1-1-1982

An assessment of the kittanning bridge electrogas weldments.

Steve R. Paterson

AN ASSESSMENT OF THE KITTANNING BRIDGE ELECTROGAS WELDMENTS

by

Steve R. Paterson

A Thesis

Presented to the Graduate Committee

of Lehigh University

in Candidacy for the Degree of

Master of Science

in

Department of Metallurgy and Materials Engineering

1982

CERTIFICATE OF APPROVAL

This thesis is accepted and approved in partial fulfillment of the requirements for the degree of Master of Science.

15 July 1982
(date)

Professor in Charge

Chairman of Department

ACKNOWLEDGMENTS

The author wishes to thank the following persons and organizations:

The Pennsylvania Department of Transportation for providing the funding for this research project.

Dr. Alan W. Pense for his assistance on this project as well as his patience in allowing me to pursue my general education above and beyond the call of duty.

Dr. John W. Fisher for his helpful discussions, ideas and suggested reading material.

Dr. John D. Wood for his assistance towards my general education at Lehigh and for his many questions--many of which I still can't fully answer.

Louise Valkenburg for typing this thesis.

Richard Sopko for printing many of the photographs included in this thesis.

Jack Gera for drafting the sketches and graphs included in this thesis.

Bruce Somers, Rajendra Dias, Andrea Weiss, Dave Calvert, William Mohylsky and Chandrasekar Narayan for their assistance towards this thesis.

TABLE OF CONTENTS

TABLE OF CONTENTS (continued)

LIST OF TABLES

LIST OF SKETCHES

LIST OF FIGURES

LIST OF FIGURES (continued)

LIST OF FIGURES (continued)

ABSTRACT

An investigation of the electrogas girder splice welds in the Kittanning Bridge superstructure was carried out to assess the fracture and fatigue characteristics of these weldments.

Forty-three (43) weld splice locations were non-destructively examined using both ultrasonic and radiographic techniques. Chemical analyses, Gharpy vee notch samples, disk shaped compact tension samples, and metallographic samples were sectioned, tested and/or evaluated from cores trepanned from eleven (11) selected electrogas weld splice locations.

Three (3) weld splices were found to be rejectable by radiography and fourteen (14) were rejectable by ultrasonics. Correlations of notch toughness estimations of the weld centerline, offcenter line and fusion line material with metallographic evaluations of selected flaws suggest that these electrogas girder splice welds have sufficient notch toughness to prevent unstable crack propagation from the pre-existent flaws observed. Furthermore, it was shown that elastic/plastic material behavior is expected in this superstructure except in regions where the material is constrained an amount equivalent to the constraint provided by a 20 cm (8") thick plate. Conservative estimates of the fatigue characteristics of these weldments suggests that fatigue crack propagation from pre-existent flaws may occur at stress fluctuation equal in magnitude to the live load design stress. An estimate of the number of stress cycles prior to unstable crack growth is presented. Realistic assessment of fatigue behavior indicates it will not be of concern in this structure.

I. INTRODUCTION

Around 1949 a Russian engineer, G. Z. Voloshkevitch, combined vertical welding techniques with the principle of heating by slag resistivity to produce a new welding process known as electroslag welding, ESW.[1] By 1960 electroslag welding was beginning to be practiced worldwide, although some engineers were concerned with the weld and heat affected zone properties resulting from this high heat input welding process.

It was from this electroslag process that the electrogas, EG, welding method was developed. In the early sixties it was found that by using the ESW equipment (see Figure 1) and by adding an inert shielding gas and/or by using a flux cored welding wire vertical welding with "open-arc" heating was possible (see Figure 2). Although EG welding originated from ESW techniques the American Welding Society, AWS, believed it was appropriate to list the EG method as a variation of either the gas metal arc welding process, GMAW, or the flux cored arc welding process, FCAW, presumably due to the arc shielding methods applied in EG welding.

The electrogas welding method was found to be very popular for vertical welding of plate material with thicknesses between 1.25 cm (0.5 inches) to 7.5 cm (3.0 inches) due to its ability of providing high deposition rates with apparently low weld defect volumes. EG welding is however a high heat input welding method and thus concern about the resultant weld and heat affected zone properties was discussed by welding engineers.[1-7]

During the late sixties and early seventies, while EG and ESW was being practiced extensively in the fabrication of numerous structures, welding research institutes were slowly compiling data about the properties and problems which result from such welding techniques. Much published data from this work became available about ESW but only a small amount of data was available about EG welding.[8,9] The bulk of this research suggested that electroslag and electrogas welding produces: (1) welds with relatively large prior austenite HAZ and weld metal grain sizes; (2) weld joints with relatively low amounts of distortion and residual stress, when compared to other welding methods; (3) weld metal with a low percentage of weld flaws; and (4) weld metal and HAZ material with relatively low "as welded" Charpy impact toughness properties. It was also suggested in these papers that, by proper use and control of these welding techniques, that safe, reliable weld joints are obtainable. Apparently, the only major problem with these EG and ESW weldments appeared to be the formation of large oriented grains in the weld metal and large HAZ grains, thus producing a low toughness joint. For this reason the American Welding Society adopted special requirements for EG and ESW welds in this regard (AWS D1.1, Appendix C), specifically that they meet a weld metal toughness specification of 20J (15 ft-lb) Charpy impact energy at $-17.8^{o}C$ ($0^{o}F$).[10]

During the seventies ESW and EG welding was popular for welding bridge girder joints such as flange butt splices, web butt splices, and transition joints. It was indeed found that by

proper control of the welding process the 20J CVN impact requirement could be met and weldments apparently free of gross defects could be produced in these applications. (It is also of interest to note the non-destructive evaluation, NDE, by ultrasonic methods of these weldments proved to be very difficult due to extensive ultrasonic energy attenuation produced by the coarse grained weld and HAZ material, although it was believed "significant" defects could be recorded in spite of this problem.)

In 1977 an interstate bridge near Pittsburgh, Pennsylvania was closed due to fracture of one of its two main girders. The fracture of this girder was found to have occurred through an electroslag weldment. This fracture triggered an investigation of the other electroslag welds on this structure as well as investigations on other bridges known to have electroslag and electrogas welded joints.[11]

As a result of these preliminary investigations the Federal Highway Administration, FHWA, forbid any future use of electroslag welding (not EG) on the main tension members of federally funded bridge projects until the question of the quality of the weldments that had been investigated could be satisfactorily answered. Furthermore, the Pennsylvania Department of Transportation, PennDOT, initiated an investigation of all of its electroslag welded bridges known to exist in Pennsylvania.

Although the FHWA directives only applied to electroslag weldments, during an examination of the Brady Street bridge weld-

ments, it was observed that some web welds (which were made by the electrogas method) had toughness values that were comparable to those provided by the electroslag process.[12] In fact none of these "production" electrogas welds provided levels of CVN absorbed energy comparable to the "qualification" tests furnished by various fabricators.

The Kittanning Bridge (see Figures 3-6), which was built in Armstrong County, Pennsylvania, over the Allegheny River is a superstructure which was fabricated with many electrogas welded splice and transition joints both in its deck truss and in its girder spans. The Kittanning Bridge was constructed in the early seventies and was opened to traffic in 1981. In February, 1971, Dr. John W. Fisher submitted a proposal to PennDOT which would evaluate the quality of the "production" electrogas weldments in the Kittanning Bridge superstructure.

The objectives of this study were to: (1) review the existing NDE records available on the electrogas weldments; (2) provide another radiographic and ultrasonic inspection of a representative sample of thirty-eight (38) electrogas welds of both top and bottom flanges, web and truss members, floor beams, girders and stringers on this superstructure; (3) remove nine sample cores from selected weldments for evaluation of these weldments using appropriate metallographic, chemical analysis and fracture toughness tests; and (4) assess the fatigue and fracture resistance of the electrogas weldments examined in this superstructure.

II. EXAMINATION METHODOLOGY

Sampling

Eleven core samples were trepanned from selected EG weldments in the Kittanning Bridge structure. Sketch I shows the approximate locations of each core. Table I lists the specific core location, the core sizes, and the identification code which was used to discuss each core. Figures 7, 8 and 9 are representative photos of three of the initial core locations. Samples KA-KJ were the initial nine (9) cores trepanned for chemical, toughness and metallographic analyses. Core KJ was removed to assess some fine cracks observed during the initial inspection of the Kittanning Bridge by Drs. Pense and Fisher. Cores KK and KL were trepanned after the selective nondestructive examination showed rejectable indications in these areas. These two cores were thus removed to assess the size and severity of these rejectable defects. Core KK was centered over an indication which was listed by UT as a 2.86 cm (1 1/8"); 0 dB defect. Core KL was centered over an indication listed as slag inclusions or porosity by radiography and as a 3.18 cm (1¼"); + 2dB defect by ultrasonic examination.

Figures 10-15 show the techniques used during the removal of cores KK and KL. This sequence is as follows: (1) the defect to be removed was relocated using ultrasonics; (2) the core was removed using a trepanning drill centered over the defect (no centering holes were drilled); and (3) the hole remaining subsequent to trepanning was die penetrant inspected to search for defects extending from the hole wall. Following this trepanning

operation the remaining hole wall should be cleaned of die penetrant chemicals and immediately painted to prevent corrosive attack. This cleaning and painting procedure was evidently not performed subsequent to removal of the initial nine cores--observation of these core areas one year after their removal showed them to be free of paint, with oxide formation observed within the holes (see Figure 7).

Sectioning

Subsequent to the initial trepanning operation, each core was rough ground and etched on its flats to locate the weldment (see Figure 16). This was followed by a layout of the CVN samples, disked shaped compact tension DC(T) specimens, and metallographic sections on each core (see sketch II), care being taken to ensure that the fracture toughness specimens (CVN and DC(T)) were notched in the proper weld location (i.e., weld center line, weld off centerline, and weld fusion line).

III. TEST PROCEDURE AND RESULTS

A. General Chemical Analysis

Two different base plate materials were used in fabrication of the Kittanning Bridge girders: (1) A588 was required for flange plates > 3.81 cm (1.5") thick; (2) A572 Grade 50 was specified for flange plates ≤ 3.81 cm (1.5") thick and for all web plates. The base material from cores KD, KE, and KF should be composed of A588 material and cores KA, KB, KC, KG, KH, KJ, KK, and KL should be composed of A572 Grade 50 base material.

At the time the Kittanning Bridge was fabricated the American Bridge Division of United States Steel Corporation (whom are believed to have produced the electrogas weld in this structure) were qualified to electrogas weld both A588 and A572 Grade 50 using two filler metals--an Airco Avacore filler metal and an Airco A608 filler metal. It is not known which was used in the weldments studied.

Chemical analyses were obtained from drillings of the base material and weld metal of cores, KA, KD, KF, KG, and KH. The results of these analyses are shown in Table II along with the required chemical compositions of the two base materials and possible weld filler metals.

The chemistry of the base materials are all within the required ranges for ASTM A572 Grade 50 or ASTM A588 structural steel with the exception of the base material analyses from core KG which showed a high amount of silicon--i.e., 0.43 wt% vs the 0.15-0.30 wt% required.

In general, the weld metal chemistry with respect to the base material has a slightly lower carbon content (~ 0.05 wt% lower), a higher manganese content (~ 0.1 wt% higher), essentially the same phosphorous and sulfur content, a higher silicon content (~ 0.20 wt% higher), a higher copper content (~ 0.20 wt% higher), and a higher molybdenum content (~ 0.20 wt% higher). No trends were observed in this respect for the nickel and chromium levels. The vanadium levels were below 0.01 wt% in all the base materials and weld metals analyzed.

Charpy Impact Testing

Charpy vee-notch impact testing was performed in accordance to ASTM E23 specifications using an E23 "Type A" Charpy impact test specimen. A 240 ft-lb Satec test machine was used for all tests. Specimens were equilibrated at the listed test temperatures for 10 minutes by immersion in a liquid nitrogen cooled ethanol bath. Charpy impact tests were performed on specimens notched at either the weld centerline, the weld fusion line, or the weld quarter width (off centerline) positions. All CVN samples were notched such that fracture propagation would occur toward the initial direction of welding. Samples were fractured at temperatures of -34.4°C (-30°F), -17.8°C (0°F), 4.4°C (40°F), and 21.1°C (70°F). The tabulated results of these tests are shown in Table III.

The 0.95 confidence intervals calculated for the mean value, $\bar{X}$, of each CVN test group (i.e., for each test temperature/notch location group) were obtained with the following statistics:[13]

$$\bar{X} - t_{\alpha/2} \frac{S}{\sqrt{n}} < \mu < \bar{X} + t_{\alpha/2} \frac{S}{\sqrt{n}} \qquad (1)$$

where

$\bar{X}$ = mean of absorbed energy values

$$= \frac{\sum_{i=1}^{n} X_i}{n} \qquad (2)$$

S = standard deviation of the absorbed energy values

$$= \frac{n \cdot \sum_{i=1}^{n} X_i^2 - \left(\sum_{i=1}^{n} X_i \right)^2}{n\,(n-1)} \qquad (3)$$

X_i = i_{th} absorbed energy value within a group, $1 = 1 \rightarrow n$

n = total # of absorbed energy values within a group

μ = unknown sample mean (the expected mean if many samples were tested)

$1 - \alpha$ = confidence interval

t = random variable having the Student-t distribution with $n - 1$ degrees of freedom.

Figure 17 shows a scatter chart of all the CVN test values as well as the statistically calculated variances of the mean. In the cases of the -34.4°C and 21.1°C fusion line CVN groups the student-t statistic predicts an extremely large range of the expected mean values. The large variances of the mean predicted for these two CVN groups is partially justified by noting that these two test groups consisted of only three and two samples

respectively (see Table III). Although the student-t statistic is valid for small sample groups, the statistical values obtained from such a limited amount of test information will understandably predict a larger spread for smaller sampling sizes (i.e., the spread in the student-t calculated mean μ, becomes amplified as the sample size, n, becomes smaller--see Equation 1).

The bulk of the scatter in CVN results from EG and ESW test groups has been shown to result from variations in the specimen notch location with respect to local grain orientation and grain size. In other words, the observed scatter in CVN absorbed energy values depicts the heterogeneous nature of the energy absorption response of electrogas weld metal when measured with a CVN sized specimen--a specimen with a fracture surface area of 0.80 cm^2 (0.124 sq.in.).

As depicted by Table III and Figure 17 the fusion line tests produced the lowest average absorbed energy values at every test temperature. The centerline values were the next lowest, with the off-centerline notched samples providing the highest average absorbed energy values.

Finally, it should be noted that each weld zone provided average absorbed energy values at -17.7°C (0°F) in excess of the 20J (15 ft-lb) AWS D1.1 Appendix C requirement. In fact, every off centerline notched and centerline notched CVN sample fractured at -17.7°C produced absorbed energy values greater than the required 20 Joules. The fusion line notched CVN samples however, produced seven out of thirteen samples with absorbed

energies below 20J when fractured at -17.7°C even though the average value of these thirteen samples was 28 Joules.

Fracture Toughness Testing

Samples KD4 and KE4 were machined into Disk Shaped Compact Tension Specimens, DC(T), in accordance to ASTM E399-81 specifications (see Sketch III). Fatigued pre-cracks were placed in the weld centerline and weld off-centerline for KD4 and KE4 respectively. The fatigue pre-cracking was performed on a 10 ton Amsler Vibrophore machine, at room temperature and operating at a frequency of 100 Hz. The last 2.5% of the overall length of the notch plus fatigue crack was fatigued with a maximum stress intensity of 61.5 MPa$\sqrt{m}$ (56 ksi$\sqrt{in}$) and 24.2 MPa$\sqrt{m}$ (22 ksi$\sqrt{in}$) for samples KD4 and KE4 respectively.

Both specimens were fractured using a 54,400 kg (120,000 lb) capacity Baldwin Universal testing machine. A test temperature of -34.4°C (-30°F) was used. The load versus load displacement diagram was recorded with a Moseley X-Y recorder. The load and displacement input were obtained from a load cell and a clip-in displacement gage, respectively. Both specimens were loaded to initial fracture at a rate of 2270 kg/sec (5,000 lb/sec). This loading rate corresponds to a stress intensity rate of approximately 110 MPa$\sqrt{m}$/sec (100 ksi$\sqrt{in}$/sec). This corresponds to a conservative measure of the maximum strain rate (or stress intensity rate) which has been experimentally measured in loaded bridge structures.[14] By testing at this loading rate and at the selected test temperature of -34.4°C an estimate of the fracture

characteristic and expected weld metal toughness while in service at the lowest American Association of State Highway and Transportation Officials (AASHTO) Zone II temperature (-34.4°C to -17.8°C) should be obtained.

The load-load displacement curves obtained from both samples exhibited shapes characteristic of elastic/plastic material behavior (see Sketch IV), thus critical, opening mode (Mode I), stress intensity, K_{IC}, values could not be calculated by the procedure outlined in ASTM E399. The fracture toughness was therefore estimated using the J-integral procedure proposed by Rice.[15] Specifically, the single specimen approximation developed by Rice, Paris, and Merkle (see Appendix 1 and references 16, 17) was used for this analysis. For this case

$$J = \frac{2}{b} \int_0^{\Delta} \frac{P}{B} \, d\Delta \tag{4}$$

or $$J = \frac{2A}{b\,B} \tag{5}$$

where A = area under the load/load point displacement curve

P = the applied load

J = the elastic-plastic stress intensity factor

Δ = load displacement

B = thickness of the specimen

b = uncracked ligament = W - a

In both of these tests initial pop-in fracture occurred. The values of the initial load drop and load-displacement corresponding to the initiation of the first pop-in cracks were used to

calculate the critical elastic-plastic stress intensity factors, J_{IC}.

These elastic/plastic critical stress intensity factor estimations, J_{IC}, were converted to values of the elastic critical stress intensity factor, K_{IC}, using the equation:

$$K_{IC} = (J_{IC}\ E)^{\frac{1}{2}} \qquad (6)$$

K_{IC} values of 119 MPa$\sqrt{m}$ (109 ksi$\sqrt{in}$) and 125 MPa$\sqrt{m}$ (114 Ksi$\sqrt{in}$) for samples KD4 and KE4 respectively were obtained.

Figure 18 shows the fracture morphology of specimens KD4 and KE4. The specimen with a weld centerline fatigue precrack, KD4, showed no tendency towards out-of-plane propagation, whereas the weld off-centerline fatigue precracked sample, KE4, showed significant out-of-plane crack propagation (the crack propagated from its initial off centerline position toward the weld centerline). The initial "pop-in" fracture of the sample KE4 did, however, occur along the initial fatigue fracture plane thus providing the necessary information for a valid off centerline toughness estimation (out-of-plane crack propagation produces non-symmetrical loading conditions--thus any load-displacement data analyzed beyond the initial "in-plane" crack propagation would not be valid without an expression to account for the resulting non-symmetrical loading).

NDE

During the period 8/3/79 through 5/22/80 forty-three (43) weld splice locations were examined in the Kittanning Bridge superstructure using both ultrasonic and radiographic inspection tech-

niques. This testing was carried out by the Pittsburgh Testing Laboratory.

The radiography was performed using an iridium 192 source and Kodak type R film. AWS test methods and acceptance standards were followed. A sensitivity of 2-2T was recorded by the PTL personnel.

Ultrasonic inspection was performed in accordance to AWS D1.1 using an IIW test reference black. The minimum ultrasonic acceptance levels used were in accordance to AWS D1.1 Table 9.25.3 (see Table IV).

Three weld splices were found to be rejectable by radiography and fourteen were rejectable by ultrasonics. A summary of these examinations is shown in Table V.

B. Metallography Methodology

Cores KA, KJ, KK, and KL were sectioned, ground, polished, etched, and subsequently observed macroscopically and microscopically. The emphasis of this metallographic work was to: (1) observe the general size, shape, and orientation of weld and HAZ structures; (2) observe the fine structure at the grain boundaries and within the grains (referring in this case to the prior austenite grain boundaries and interior structure) in the weld and HAZs; and (3) distinguish any metallurgical defects within these samples.

After fracturing the CVN specimens the external surfaces and fracture surface of these specimens were observed with a macroscope in an attempt to locate any substantial, previously undetected, flaws. The only significant defect found by this procedure was a small microcrack in the surface of CVN KC6. This area was also sectioned, ground, polished, etched and microscopically observed.

The sequence of observation was as follows: (1) macrophotographs were taken using a Crown Graphics Graflex 10.16 cm x 12.7 cm (4" x 5") camera; (2) light micrographs were produced using a Zeiss Axiomat Microscope (using either Type 55 polaroid black and white film or Kodak Kodacolor film); and (3) scanning electron micrographs using an ETEC Autoscan microscope with an energy dispersive x-ray analyzer were produced. Also, chromium shadowed carbon-acetate replicas were made of a polished and etched sample from core KJ to observe the weld metal structural morphology in more detail. These replicas were examined using a Philips EM300

transmission microscope.

CVN KC6 was also examined in more detail by contact microradiography techniques--to document possible microsegregation in this area. The microradiographic sample was prepared by: (1) cutting off a thin slice of metal with a kerosene cooled diamond cut-off wheel; (2) hand grinding this slice to ~ 10 mils by fastening to a Bakelite mount with double-stick tape; (3) placing this 10 mil slice onto a glass slide (with double-stick tape), clamping this glass slide in a Buehler glass slide holder to ensure a uniform metal thickness is obtained during final grinding; (4) hand grinding to ~ 1.5 mils (using a 600 grit paper for the final grinding); and (5) placing this wafer in contact with a fine grained photographic emulsion (Kodak High Resolution Film-S0343) and exposing it to 30 kV manganese filtered iron radiation for approximately 30 minutes.

This contact microradiography technique relies upon the differences in linear absorption characteristics of different elements in radiation of a given wavelength in accordance to the following equation:

$$I = I_o e^{-\mu_i t} \qquad (7)$$

where I = the transmitted intensity of radiation

I_o = the incident intensity of radiation

μ_i = linear absorption coefficient of each element in the metal sheet examined

t = material thickness

C. Metallography--Results

Weld Macrostructure

The macrostructure of the weld metals studied consisted of fine elongated prior austenite grains which extend epitaxially from the base metal grains. These extend inward and upward with a form factor of about 2.5. These fine elongated prior austenite grains give way to fine equiaxed prior austenite grains at approximately half the distance to the weld centerline (see Sketch V and Figures 19-21). Sketch VI shows four slightly different types of weld metal macrostructures which Paton[18] observed in his studies on electroslag welds.

Weld Microstructures

A microscopic study documented the following features of the weld metal zones:

- the weld metal grains grow epitaxially from the base metal grains.
- a continuous network of proeutectoid, idiomorphic (blocky) ferrite was observed along the weld metal prior austenite grain boundaries--thus deliniating these boundaries.
- near the weld centerline the proeutectoid, idiomorphic ferrite network becomes discontinuous.
- the weld metal prior austenite grain interiors consist of Widmanstätten ferrite (extending from the idiomorphic ferrite), acicular ferrite, cementite platelets, and occasional fine pearlite colonies.

- the fine elongated prior austenite weld metal grains have an approximate size of 0.3 mm x 2.0 mm.
- the fine equiaxed prior austenite weld metal grains have an approximate diameter of 0.15 mm (ASTM prior austenite G.S.
- occasional abnormally large (~ 3.0 mm in diameter) prior austenite grains were observed in the weld metal. These were generally located near the fusion line or near the weld faces.
- small equiaxed weld metal prior austenite grains were observed along portions of the fusion line. These are believed to result from partial melting of the base metal grains in these areas--thus producing equiaxed "weld metal grains" with a size which corresponds to the unmelted "base metal" grains located nearby. Figures 22-36 depict these microstructures.

HAZ Microstructures

Three distinct heat affected zones were observed in the EG weldments studied:

- A coarse grained heat affected zone nearest the fusion line which consisted of: (1) continuous networks of idiomorphic ferrite along prior austenite grain boundaries; (2) large amounts of Widmanstätten ferrite; (3) fine pearlite colonies; and (4) ferrite grains located within the prior austenite grains. The ASTM prior austenite grain size in the zone was estimated to be 0 at the fusion

line and 5½ up to a distance of 2 from the fusion line.

- 2-3 mm from the fusion line the structure changes to a ferrite/pearlite structure with an ASTM ferrite grain size of 9½. No prior austenite grain boundaries were delineated in this zone, thus no ASTM prior austenite G.S. was measured.
- 6-10 mm from the fusion line the HAZ structure again changes to a ferrite/refined pearlite structure with an ASTM ferrite grain size of 8.
- Somewhere around 7-12 mm, depending on the weld position and heat input of a particular weldment, the unaffected base material was observed. The unaffected base metal consists of a ferrite/fine pearlite structure with an ASTM ferrite grain size of ~ 7. Figures 37-48 depict these structures.

Macroscopic and Microscopic Defects

Cores KJ, KK, KL and CVN KC6 were examined macroscopically and microscopically to determine the nature and significance of any defects present. Specimens KK and KL were studied to identify the rejectable defects detected by NDE. Specimen KJ was a sample in which defects were observed during the initial inspection of this core. A defect was found in CVN KC6 during the initial lay-out scheme for core KC.

Core KK was sliced into four ~ 1 cm sections, each perpendicular to the welding direction in an attempt to locate any flaws associated with the 2.86 cm/0 dB indication found by UT inspection. No internal defects were found. A 1.8 cm long piece of slag was

observed on the south face of this core near the region of the UT indication. It is believed that this non-removed slag provided the UT indication. Figures 49-54 illustrate the examination sequence of this core.

Core KL was sectioned transverse to the weld direction to locate the 3.18 cm/+2dB indication recorded in this region (see Figures 55-61). The defect was found to be a slag inclusion located at the root of a repair weld. The repair weld appears to have been produced with a shielded metal arc welding (SMAW) process. This slag inclusion was estimated to be 1.3 mm in diameter and 10 mm long. The radiograph from this splice joint shows at least five other slag inclusions located at the root of this SMAW-repair weld, the longest of these being the defect which was removed by this core KL (see Figure 61). Figure 60 shows the severe notch provided by this slag inclusion.

Core KJ was removed from the north edge of the lower flange plate in girder 103G2D to examine the defects found by Drs. Pense and Fisher during their initial inspection of the Kittanning Bridge. Three defects were observed on this flat plate end as is shown in Figure 62. The defect labeled "A" was found to be a 2 mm long crack filled with slag and free copper (see Figures 63-68). The defect labeled "B" (Figure 64) was determined to be a machining mark produced during slippage of the trepanning drill (see Figures 69 and 70). The small cracks shown in Figure 70 appear to be cracks running throughout a surface layer of corrosion product formed in this groove. The defect labeled "C" (Figure 62) was

estimated to be slag and a HAZ which was not removed after the welding of runoff tabs to this flange plate.

Figures 71-77 show the location and morphology of the defect found in CVN-KC6. This 2.5 mm crack did not appear to contain any foreign material, but simply propagates along the idiomorphic pro-eutectoid ferrite interface associated with a prior austenite grain boundary. Microradiography of this area showed no detectable elemental microsegregation, thus suggesting that this defect was a hydrogen assisted crack.[19,20,21]

IV. FATIGUE AND FRACTURE RESISTANCE PLAN

Background

Experience has shown that structures can potentially fail in the following modes:[22]

1. General yielding or excessive plastic deformation.
2. Buckling or general instability (either plastic or elastic).
3. Subcritical crack growth (fatigue, stress corrosion, corrosion fatigue, etc.).
4. Unstable crack extension, either ductile or brittle, leading to either partial or complete failure of a member.

The emphasis of this research project was to assess the resistance of the electrogas weldments contained in the Kittanning Bridge superstructure to unstable crack extension and to subcritical crack growth by fatigue. In making this assessment the worst expected environmental conditions and the most severe loading conditions were assumed to be acting on the structure simultaneously--an analysis which should provide a conservative estimate of the expected mechanical behavior of these weldments. The following conditions were assumed:

Temperature = -34.4°C (-30°F) = Lower bound of AASHTO Zone II temperature range.

Static stress acting on the weldment = Dead load + Live load + Impact load + Thermally induced load + residual stress due to welding $\tilde{=}$ the weldments yield

strength, σ_s measured at an intermediate strain rate and at -34.4°C.

Flaw Sizes and Geometry = the most severe flaws found in the selective NDE study.

Loading Rate = 110 MPa $\sqrt{m}$/sec in front of each crack tip.

Fluctuating Stress, $\Delta\sigma$ = sum of the stresses produced by the estimated live and impact loads.

Fracture Plan

An assessment of the resistance of these electrogas weldments to unstable crack extension using fracture mechanic concepts requires knowledge of the following:

- stress level = f (stress conditions, design and fabrication)
- flaw geometry and size = f (allowable flaw sizes and distributions, NDE capabilities, and fabrication quality)
- material toughness = f (material, strain rate, temperature, section thickness)

Due to the small quantity of material available for testing no weld or base metal yield strengths were measured. An estimate of the maximum possible stress acting on these electrogas weldments should be the value of the lowest yield strength (as measured by a tensile test) encountered in either the weld metal, the HAZ or the nearby base material. Figures 78 and 79 show hardness traverses of cross-sections of the weldment in cores KJ and KK respectively. Since the hardness was found to be essentially constant throughout the weld metal, HAZ, and base material a conservative estimate of

the effective tensile yield strength was thus made by assuming a yield strength equal to the minimum required yield strength of the A588 and A572 Grade 50 base materials--345 MPa (50 ksi). Under the influence of intermediate loading rates and low temperatures (-34.4°C) this value may perhaps reach as high as 415 MPa (60 ksi)--for a rationale of this estimate see Appendix II.

The most severe flaw geometry/size/location combination expected in these weldments was assumed to be equivalent to the most severe flaws found during our selective non-destructive evaluation of these weldments. Two flaw types will be considered: (1) elliptical internal flaws with minor axis dimensions, 2a, approximately 2.5 mm in length; and (2) elliptical surface flaws with crack lengths a = 2.0 mm.

The material toughness was measured by two separate tests: (1) the numerous dynamic CVN tests performed at various test temperatures, and weld locations, and (2) the two disk shaped compact tension specimens.

As discussed in the section on Fracture Toughness Testing, K_{IC}, values of 120 MPa$\sqrt{m}$ and 125 MPa$\sqrt{m}$ were estimated from the weld metal loaded at 110 MPa$\sqrt{m}$/sec and equilibrated to a temperature of -34.4°C.

Dynamic CVN data in the transition region was equated to dynamic K_{IC} values, K_{ID}, using the empirical formula proposed by Barsom et al.[23]

$$K_{ID} = (5\,E\,(CVN))^{\frac{1}{2}} \qquad (8)$$

where E = modulus of elasticity

These K_{ID} values were subsequently shifted along the temperature axis by the empirical equation (also proposed by Barsom et al.[24]):

$$T_{shift} = 0.75\ (215 - 1.5\ \sigma_y) \qquad (9)$$

where T_{shift} = the temperature shift in ^{o}F experimentally observed between equivalent dynamic stress intensity, K_{ID}, and "bridge loaded" (samples loaded at a rate of ~ 110 MPa$\sqrt{m}$/sec) stress intensity, $K_{IC_{bridges}}$, values.

σ_y = the room temperature static yield strength in ksi $\tilde{=}$ 50 ksi.

Figure 80 shows the results of these two empirical transformations. These results add credence to the two K_{IC} values measured with the disk shaped compact tension sample, as well as showing the expected trends in the K_{IC} values at temperatures below -34.4°C (30°F).

The stress intensity factor for cracks or fissures can be expressed as:[25]

$$K = F_e F_s F_w F_g\ \sigma\sqrt{\pi a} \qquad (10)$$

where F_e = crack shape correction factor

F_s = free surface correction factor

F_w = finite width correction factor

F_g = stress gradient correction factor

σ = applied gross section stress

K = stress intensity value

For embedded flaws the upper and lower bound of the stress intensity value is given by:

$$\frac{2}{\pi}\ \sigma\sqrt{\pi a_1} \leq K < \sigma\sqrt{\pi a_2} \qquad (11)$$

where a_1 = radius of a penny shaped flaw

a_2 = the half width of an elongated defect

Solving for the radius of an unstable penny shaped defect leads to the upper bound solution:

$$a_1 = \left(\frac{\pi K_{IC}}{2 \sigma_y}\right)^2 \frac{1}{\pi} = \left(\frac{\pi}{2} \frac{119 \text{ MPa}\sqrt{\text{m}}}{415 \text{ MPa}}\right)^2 \frac{1}{\pi} = 6.5 \text{ cm}$$

or solving for the half width of an elongated defect provides a lower bound solution

$$a_2 = \left(\frac{K_{IC}}{\sigma_y}\right)^2 \frac{1}{\pi} = \left(\frac{119 \text{ MPa}\sqrt{\text{m}}}{415 \text{ MPa}}\right)^2 \frac{1}{\pi} = 2.6 \text{ cm}$$

thus $2a_2 = 5.2$ cm

For surface flaws the upper and lower bound of the stress intensity value is given by:

$$1.1 \frac{2}{\pi} \sigma \sqrt{\pi a_1} \leq K < 1.1 \sigma \sqrt{\pi a_2} \qquad (12)$$

Thus $a_1 = 5.3$ cm

$a_2 = 2.2$ cm

These calculations suggest that embedded or surface flaws with the geometry/size configurations calculated would be unstable if a material with a plane strain critical stress intensity of 119 MPa$\sqrt{\text{m}}$ is loaded to a stress of 415 MPa under plain strain conditions. By comparing these calculated flaw geometry/size combinations to the flaw geometry/sizes found during our selective NDE and microscopic evaluations it was concluded that the defects observed in the Kittanning Bridge electrogas splice joints are not in danger of propagating in an unstable fashion (the calculated

sizes are an order of magnitude larger than the observed sizes). Furthermore if we consider the condition necessary for plane strain:

$$a, B \geq 2.5 \left(\frac{K_{IC}}{\sigma_y}\right)^2 = 2.5 \left(\frac{119 \text{ MPa}\sqrt{\text{m}}}{415 \text{ MPa}}\right)^2 \qquad (13)$$

$$= 20.6 \text{ cm } (8.1")$$

we can further conclude that the likelihood of reaching full constraint conditions in the Kittanning Bridge electrogas weldments is unlikely--thus providing an increase in critical stress intensity necessary for unstable crack propagation and increased propensity for elastic/plastic behavior prior to crack extension.

Fatigue Control Assessment

This latter analysis only addressed unstable crack propagation, not stable propagation by mechanisms such as fatigue. Another question to be addressed is whether defects equivalent in severity to those observed in the Kittanning Bridge electrogas welds are likely to propagate by fatigue.

Although no fatigue threshold, ΔK_{th}, measurements for electrogas weld metals were available an expected conservative estimate of 2.8 MPa$\sqrt{\text{m}}$ (2.6 ksi$\sqrt{\text{in}}$) as has been measured for electroslag weld metal in structural steel, is assumed.[26]

For a defect to be resistant to fatigue propagation:

$$\Delta K_{th} > F_e F_g F_s F_w \Delta\sigma \sqrt{\pi a} \qquad (14)$$

where ΔK_{th} = the fatigue threshold stress intensity range below which fatigue propagation is unmeasurably slow.

$\Delta\sigma$ = the gross section stress range.

From a summation of the stresses due to live loads and impact loads a maximum expected stress range for the girders in this structure is found to be 34 MPa (5 ksi).

For embedded flaws:

$$\frac{2}{\pi} \Delta\sigma \sqrt{\pi a_1} \leq \Delta K < \Delta\sigma \sqrt{\pi a_2} \qquad (15)$$

where a_1 = radius of a penny shaped flaw

a_2 = the half width of an elongated defect

Solving for a_1 and a_2 provides the following:

$$a_1 = \left(\frac{\pi\ (\Delta K_{th})}{2\ (\Delta\sigma)}\right)^2 \frac{1}{\pi} = \left(\frac{\pi\ (2.8\ \text{MPa}\sqrt{\text{m}})}{2\ (34\ \text{MPa})}\right)^2 \frac{1}{\pi} = 5.3\ \text{mm}$$

$$a_2 = \left(\frac{\Delta K_{th}}{\Delta\sigma}\right)^2 \frac{1}{\pi} = \left(\frac{2.8\ \text{MPa}\sqrt{\text{m}}}{34\ \text{MPa}}\right)^2 \frac{1}{\pi} = 2.2\ \text{mm}$$

For surface flaws:

$$1.1\ \frac{2}{\pi}\ \Delta\sigma \sqrt{\pi a_1} \leq \Delta K < 1.1\ \Delta\sigma\sqrt{\pi a_2} \qquad (16)$$

where a_1 = the crack depth of a semicircular surface crack

a_2 = the crack depth of an elongated surface crack

in this case.

$$a_1 = 4.4\ \text{mm}$$

$$a_2 = 1.8\ \text{mm}$$

Since the largest embedded and surface flaws observed in the Kittanning Bridge weldments studied are larger than the sizes calculated to just prevent growth by fatigue it must be assumed that fatigue crack growth can occur from flaws located in the Kittanning Bridge electrogas weldments.

The rate of fatigue crack growth can be estimated using the equation proposed by Paris.[27]

$$\frac{da}{dN} = A\ \Delta K^m \qquad (17)$$

where $\frac{da}{dn}$ = fatigue crack growth

ΔK = stress intensity factor range = $K_{max} - K_{min}$

A,m = f(material variables, environment, frequency, temperature, stress ratio).

For ferrite/pearlite steels an average value of

$a = 6.89 \times 10^{-12}$/cycle $(MPa)^3\sqrt{m}$ [3.6×10^{-10}/cycle $(Ksi)^3\sqrt{in}$]

and m = 3 has been experimentally measured on numerous steels,[28] thus an estimate of the fatigue crack growth rate may be obtained by application of the following equation:

$$\frac{da}{dN} = 6.89 \times 10^{-12}\ (\Delta K)^3 = 6.89 \times 10^{-12}(F_e F_s F_w F_g \Delta\sigma \sqrt{\pi a})^3$$

with $\Delta K = MPa\sqrt{m}$

a = crack length in meters

The number of stress cycles necessary to grow a "stable" flaw by fatigue to a size which will cause "unstable" flaw growth (see Fracture Plan) can be obtained by a numerical or direct integration of the Paris fatigue equation described above. For direct integration techniques to be valid the product of the stress intensity correction factors, F_e, F_s, F_w and F_g and the gross section stress range, $\Delta\sigma$, must be constant throughout the life of the section, a requirement which is not likely to be met in the electrogas weldments studied. However, as an estimate of the total expected life, we can assume we have a penny shaped flaw where $K = \frac{2}{\pi}\sigma\sqrt{\pi a}$.

For this case the total number of stress cycles becomes:

$$N_f = \frac{2}{(m-2)\, A\, Y^m\, \sigma^m} \quad \frac{1}{a_o^{(m-2/2)}} - \frac{1}{a_f^{(m-2/2)}} \qquad (18)$$

where a_o = the initial flaw size

a_f = the final flaw size

For an initial flaw size of 2.5 mm (0.0984"), a final flaw size of 6.5 cm (2.56"), and a gross section stress range of 34 MPa (5 ksi):

$$N_f = \frac{2}{\frac{2}{\pi}^3\, 6.89 \times 10^{-12}\, (34\ \text{MPa})^3} \quad \frac{1}{\sqrt{2.5 \times 10^{-3}}} - \frac{1}{\sqrt{6.5 \times 10^{-2}}}$$

= 460 million cycles

Figure 81 shows a plot of cycles to failure vs. initial crack size for both an embedded penny shaped crack and a surface flaw with an $a/2_c$ (crack depth/width) ratio of 0.36 -- these being two expected equilibrium crack geometries.[29]

It should be noted that the fact that fatigue crack growth can occur under some conditions in this structure does not mean that it is diminished in capacity. First, it is clear that the conservatively predicted cyclic life is quite long, over 400 million cycles, providing ample service life. Second, the predicted point at which a fatigue crack becomes unstable is based on a conservative estimate of critical flaw size, one that could be several times smaller than the true one. Thus cyclic life could be longer than predicted. Third, the fatigue threshold behavior of real flaws is usually somewhat different from uniform laboratory produced cracks. In general threshold values are much higher for real flaws because

they are not as sharp, have irregular fronts and are often branched. If the threshold for growth were raised only slightly, or the live load reduced, crack growth would not be predicted. If, for example, the live load was actually $\sim$ 20 MPa (3 Ksi) then no growth will occur. Thus the crack growth calculations are quite conservative, and significant fatigue crack growth, while possible, is unlikely in this structure.

V. CONCLUSIONS

The selective chemical, metallographic, notch toughness, and non-destructive examinations performed on the electrogas weld splice joints in the Kittanning Bridge superstructure provided the following information:

- The weld and base metal chemistry was within the expected limits for A572 Grade 50 steel except in core KG which showed a slightly high silicon content (0.43 wt% vs. 0.15-0.30 wt% required).
- The weld fusion line produced the lowest average absorbed Charpy vee notch absorbed energy values at every test temperature. The weld centerline produced the next lowest values with the off-centerline providing the highest absorbed energy values.
- Each weld zone provided average Charpy vee notch absorbed energy values at -17.7°C (0°F) in excess of the 20 J (15 ft-lb) AWS D1.1 Appendix C requirement. The AASHTO Zone 2 requirement of 20 J (15 ft-lb) at 4.4°C (40°F) is thus also met.
- Two disk shaped compact tension specimens fractured at -34.4°C (-30°F) with a 110 MPa$\sqrt{m}$/sec (100 ksi$\sqrt{in}$/sec) loading rate provided notched fracture toughness estimates, K_{IC}, of 119 MPa$\sqrt{m}$ (109 ksi$\sqrt{in}$), and 125 MPa$\sqrt{m}$ (114 ksi$\sqrt{in}$) for the weld centerline and off centerline positions respectively.
- Of the forty-three (43) weld splice locations examined by radiography and UT three (3) were found to be rejectable by

radiography and fourteen (14) were found to be rejectable by ultrasonics. Trepanning and metallographic examination of the two most severe defects showed them to be: (1) a 1.3 mm diameter x 10 mm long internal slag inclusion located at the root of a repair weld, and (2) a 18 mm long piece of slag not removed from the inside of a box girder transition splice weld.

- A 2.5 mm internal crack believed to have resulted from hydrogen assisted ferrite vein cracking and a 2 mm deep surface flaw resulting from slag and free copper entrapment were also observed during metallographic examination of select cores.
- A fracture mechanics estimation of the allowable flaw size prior to unstable brittle fracture in these electrogas weldments suggests that the electrogas weld metal studied had sufficient notch toughness at the least anticipated service temperature (LAST) to tolerate flaws of the sizes and severities observed. Furthermore, fracture initiation in these weldments will occur in an elastic/plastic regime at the LAST except in regions with high triaxial restraint.
- Fatigue crack growth from pre-existent flaws is estimated to be possible if a gross section stress range equivalent in magnitude to the live load design stress (34 MPa, 5 ksi) is applied to these electrogas girder splice welds. If, on the other hand, these electrogas girder splice welds experience the more realistic live load stress of $\sim$ 20 MPa (3 ksi) then

flaws of the size and severity observed will not provide sufficient stress intensity to provide crack extension by fatigue (i.e., the stress intensity range, ΔK, will be less than the fatigue threshold range ΔK_{TH}).

- Even if continuous 34 MPa (5 ksi) stress fluctuations were experienced in these electrogas girder splice welds while the structure was operated at the least anticipated service temperature of -34.4°C (-30°F) then the fatigue life is estimated to be greater than 400 million cycles, still providing this structure with a safe life capability.

TABLE I

Location and Identification and Size

of Trepanned Cores

Identification	Sample Location	Sample Size
KA	Truss Span--L9-L11 at L9 (bottom flange)	4" dia x 1"
KB	Truss Span--U2-U4 at U2 (bottom flange)	4" dia x 1"
KC	Truss Span--U10-L11 at L11 (bottom flange)	4" dia x 3/4"
KD	Girder Span--901G2D-NS	2 3/4" dia x 2"
KE	Girder Span--320G2-S at 47' from field spl. (bottom flange)	2 3/4" dia x 2"
KF	Floor Beam--FBP10-E at Pier #10	2 3/4" dia x 1 5/8"
KG	Girder Span--702G2D-SS (bottom flange, CL of span)	2 3/4" dia x 1½"
KH	Girder Span--402G2D-SS (bottom flange)	2 3/4" dia x 1½"
KJ	Girder Span--103G2D (bottom flange)	2 3/4" dia x 1"
KK	Truss Span--L11-L13 at L11 (north web)	1 3/4" dia x 1½"
KL	Girder Span--103G2D (west web)	1 3/4" dia x 5/8"

TABLE II - Weld and base metal chemistry (in weight percents).

Sample ID	ASTM A572 Grade 50	KA Base Metal	KA Weld Metal	KD Base Metal	KD Weld Metal	KF Base Metal	KF Weld Metal	KG Base Metal	KG Weld Metal	KH Base Metal	KH Weld Metal
Carbon	0.23 max	0.21	0.13	0.16	0.13	0.15	0.11	0.20	0.13	0.17	0.13
Manganese	0.75 - 1.35	1.21	1.32	0.98	1.19	1.04	1.31	1.28	1.17	1.31	1.36
Phosphorous	0.040 max	0.012	0.013	0.015	0.014	0.013	0.013	0.020	0.019	0.012	0.021
Sulfur	0.050 max	0.028	0.019	0.019	0.016	0.030	0.016	0.032	0.023	0.026	0.020
Silicon	0.15 - 0.30	0.21	0.42	0.23	0.43	0.23	0.51	0.43	0.34	0.21	0.35
Copper	-	0.022	0.304	0.253	0.412	0.318	0.427	0.030	0.188	0.013	0.347
Nickel	-	0.040	0.047	0.134	0.071	0.129	0.087	0.070	0.045	0.022	0.055
Chromium	-	0.047	0.045	0.435	0.187	0.419	0.165	0.040	0.066	0.037	0.124
Molybdenum	-	<0.005	0.255	0.040	0.263	0.020	0.319	0.008	0.227	<0.005	0.208
Vanadium	-	<0.01	<0.01	<0.01	<0.01	<0.01	<0.01	<0.01	<0.01	<0.01	<0.01

TABLE III

Charpy Impact Test Results

Specimen	Position	Temperature	Energy Absorbed
KF1-3	Fusion line	-30°F	9.5
KE1-4	"	"	5.0
KH2-3	"	"	25.0
95% confidence interval of the mean = -(12.9) ⟷ 39.3			$\bar{X}$ = 13.17 S = 10.49 $\mu 0.95 = 13.2 \pm 26.1$
KF1-2	Fusion line	0°F	10.0
KF2-2	"	"	26.0
KF3-2	"	"	11.0
KE1-1	"	"	40.0
KE2-1	"	"	43.0
KE3-1	"	"	10.5
KD2-2	"	"	34.5
KD3-2	"	"	9.0
KH2-2	"	"	35.0
KB4	"	"	14.0
KB4	"	"	35.0
KC4	"	"	7.0
KC5	"	"	5.5
95% confidence interval of the mean = 13.1 ⟷ 30.1			$\bar{X}$ = 21.58 S = 14.14 $\mu 0.95 = 21.6 \pm 8.5$
KF2-3	Fusion line	40°F	14.5
KF3-3	"	"	29.0
KE2-4	"	"	45.5
KE3-4	"	"	20.0
KB1	"	"	45.5
KB2	"	"	51.0
KC2	"	"	12.5
95% confidence interval of the mean = 16.2 ⟷ 46.0			$\bar{X}$ = 31.14 S = 16.12 $\mu 0.95 = 31.1 \pm 14.9$

continued --

TABLE III (continued)

Charpy Impact Test Results

Specimen	Position	Temperature	Energy Absorbed
KD2-3	Fusion line	70°F	45.0
KD3-3	"	"	49.0
95% confidence interval = 21.6 ⟷ 72.4 of the mean			$\bar{X}$ = 47.0 S = 2.83 $\mu 0.95 = 47.0 \pm 25.4$
KE1-3	Center line	-30°F	26.5
KD1-4	"	"	20.0
KH1-3	"	"	16.0
KG1-4	"	"	13.0
95% confidence interval = 9.6 ⟷ 28.2 of the mean			$\bar{X}$ = 18.875 S = 5.84 $\mu 0.95 = 18.9 \pm 9.3$
KE1-2	Center line	0°F	22.5
KE2-2	"	"	17.0
KE3-2	"	"	20.5
KD1-1	"	"	22.5
KD2-1	"	"	30.0
KD3-1	"	"	24.0
KH1-2	"	"	27.0
KG1-1	"	"	20.5
KG2-1	"	"	28.0
KB3	"	"	30.0
KC1	"	"	30.5
KC6	"	"	36.0
95% confidence interval = 22.2 ⟷ 29.2 of the mean			$\bar{X}$ = 25.67 S = 5.49 $\mu 0.95 = 25.7 \pm 3.5$

continued --

TABLE III (continued)

Charpy Impact Test Results

Specimen	Position	Temperature	Energy Absorbed
KE2-3	Center line	40°F	32.0
KE3-3	"	"	32.0
KD2-4	"	"	31.0
KD3-4	"	"	43.0
KG2-4	"	"	30.0
			$\bar{X}$ = 33.6
95% confidence interval of the mean = 27.0 ⟷ 40.2			S = 5.32
			$\mu 0.95 = 33.6 \pm 6.6$
KF1-4	Off-Center line	-30°F	27.0
KD1-3	"	"	25.0
KH1-4	"	"	17.0
KG1-3	"	"	22.0
			$\bar{X}$ = 22.75
95% confidence interval of the mean = 15.9 ⟷ 29.7			S = 4.35
			$\mu 0.95 = 22.8 \pm 6.9$
KF1-1	Off-Center line	0°F	31.0
KF2-1	"	"	44.0
KF3-1	"	"	34.0
KD1-2	"	"	28.0
KH1-1	"	"	24.5
KH2-1	"	"	23.0
KG1-2	"	"	38.0
KG2-2	"	"	38.0
			$\bar{X}$ = 32.56
95% confidence interval of the mean = 26.5 ⟷ 38.7			S = 7.29
			$\mu 0.95 = 32.6 \pm 6.1$
KF2-4	Off-Center line	40°F	55.0
KF3-4	"	"	58.0
KH2-4	"	"	38.5
KG2-3	"	"	46.0
			$\bar{X}$ = 49.25
95% confidence interval of the mean = 34.9 ⟷ 63.7			S = 9.07
			$\mu 0.95 = 49.3 \pm 14.4$

TABLE IV

AWS S1.1 Ultrasonic Acceptance Criteria

MINIMUM ACCEPTANCE LEVELS (DECIBELS)

REFLECTOR SEVERITY	WELD THICKNESS (in.) AND TRANSDUCER ANGLE																	
	5/16 to 3/4		>3/4 to 1-1/2		>1-1/2 to 2-1/2			>2-1/2 to 4			>4 to 6			>6 to 8		
	70°		70°		70°	60°	45°	70°	60°	45°	70°	60°	45°	70°	60°	45°
Large Reflectors	+14		+ 9		+5	+ 8	+10	+2	+5	+ 7	-1	+2	+4	-3	0	+2
Small Reflectors	+15		+10		+7	+10	+12	+4	+7	+ 9	+1	+4	+6	-1	+2	+4
Minor Reflectors	+16		+11		+9	+12	+14	+6	+9	+11	+3	+6	+8	+1	+4	+6

SCANNING LEVELS

Sound path distance, in	mm	Above zero reference, db
to 2-1/2	63.5	+20
>2-1/2 to 5	63.5 - 127	+25
>5 to 10	127 - 254	+35
>10 to 15	254 - 381	+45

LARGE REFLECTORS:
Any discontinuity, REGARDLESS OF LENGTH, having a more serious rating (smaller number) than this level shall be rejected.

SMALL REFLECTORS:
Any discontinuity longer than 3/4 in. (19 mm) having a more serious rating (smaller number) than this level shall be rejected.

MINOR REFLECTORS:
Any discontinuity longer than 2 in. (51 mm) having a more serious rating (smaller number) than this level shall be rejected.

TABLE IV

AWS S1.1 Ultrasonic Acceptance Criteria

MINIMUM ACCEPTANCE LEVELS (DECIBELS)

REFLECTOR SEVERITY	WELD THICKNESS (in.) AND TRANSDUCER ANGLE																	
	5/16 to 3/4		>3/4 to 1-1/2			>1-1/2 to 2-1/2			>2-1/2 to 4			>4 to 6			>6 to 8		
	70°		70°			70°	60°	45°	70°	60°	45°	70°	60°	45°	70°	60°	45°
Large Reflectors	+14		+ 9			+5	+ 8	+10	+2	+5	+ 7	-1	+2	+4	-3	0	+2
Small Reflectors	+15		+10			+7	+10	+12	+4	+7	+ 9	+1	+4	+6	-1	+2	+4
Minor Reflectors	+16		+11			+9.	+12	+14	+6	+9	+11	+3	+6	+8	+1	+4	+6

SCANNING LEVELS

Sound path distance, in	mm	Above zero reference, db
to 2-1/2	63.5	+20
>2-1/2 to 5	63.5 - 127	+25
>5 to 10	127 - 254	+35
>10 to 15	254 - 381	+45

LARGE REFLECTORS:
Any discontinuity, REGARDLESS OF LENGTH, having a more serious rating (smaller number) than this level shall be rejected.

SMALL REFLECTORS:
Any discontinuity longer than 3/4 in. (19 mm) having a more serious rating (smaller number) than this level shall be rejected.

MINOR REFLECTORS:
Any discontinuity longer than 2 in. (51 mm) having a more serious rating (smaller number) than this level shall be rejected.

TABLE V

Locations of Rejectable Defects

	Member	Plate	Defect	NDT Page
	North Truss			
	U_0U_1 at U_0	Top Flange	+8 to +12 Db	2
	U_6U_8 at U_6	North Web	+9	8
	L_4L_5 at L_5	Bottom Flange	+6	11
*	$L_{11}L_{13}$ at L_{11}	North Web	0	20
	U_6L_5 at L_5	Bottom Flange	+10	23
	U_6L_7 at L_7	Bottom Flange	+7	23
	$U_{10}L_{11}$ at L_{11}	North Web	+12	26
	Girders			
*	103G2D	Web West Pier 1	Radiograph (porosity & slag)	37
*	103G2D	Web West Pier 1	+2 to +12	38
	103G2D	Bottom Flange	+8	39
	103G2D	Top Flange	+13 to +16	40
	202G2D	Bottom Flange	Radiograph (porosity)	41
	202G2D	Top Flange	+9	44
	402G2D	Web	+5 to +8	47
	502G2D	Top Flange	+6 to +10	51
	702G2D	Bottom Flange	Radiograph (Crack ?)	52
	702G2D	Top Flange	+10 to +15	55
	260G5 Ramp D	Bottom Flange	+8	61

* Cores KK and KL removed defects in these locations

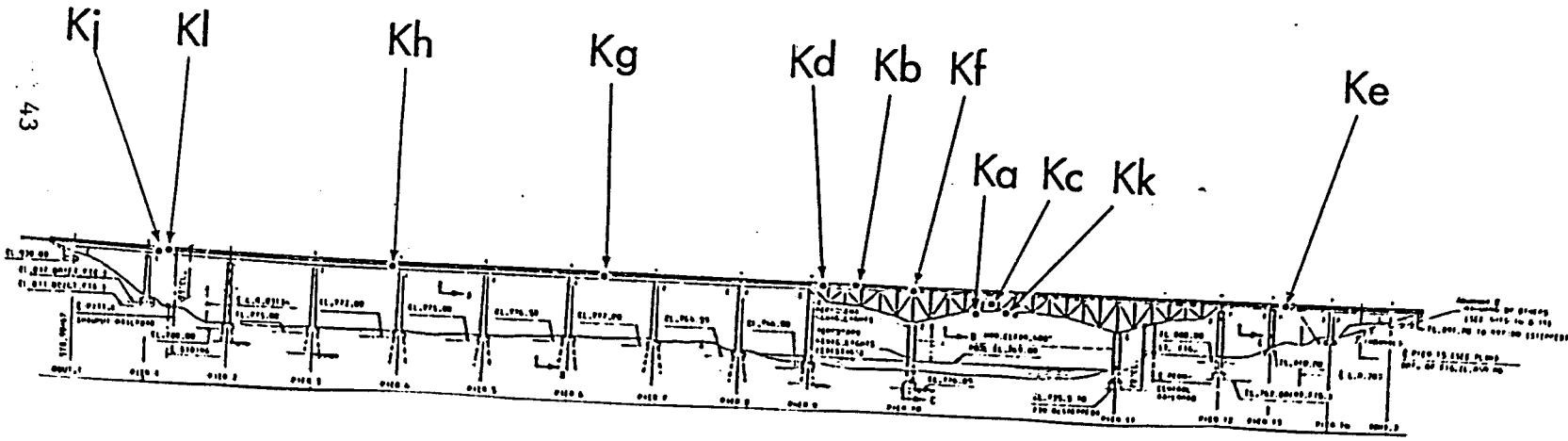

Sketch I - Approximate location of trepanned cores.

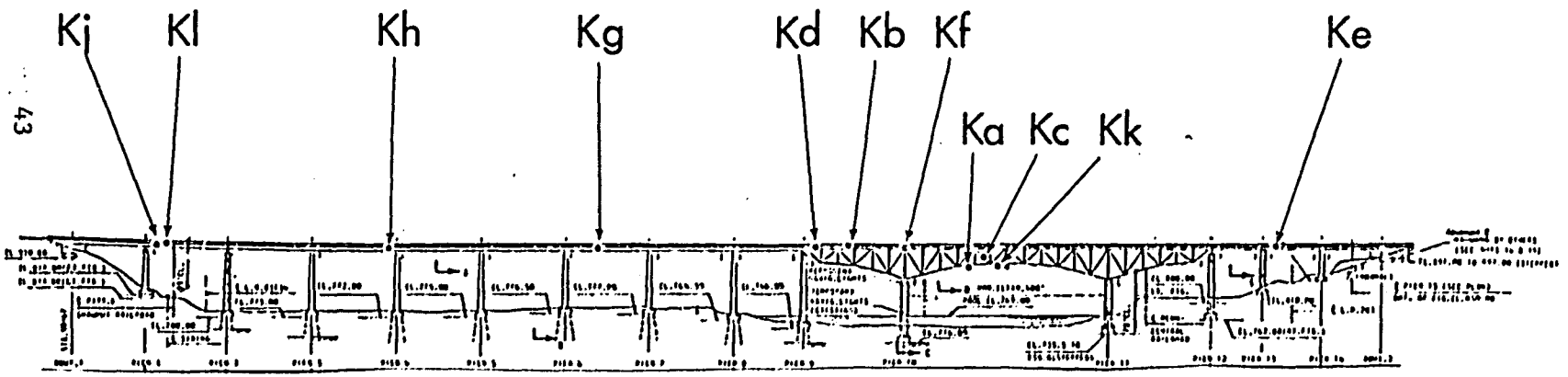

Sketch I - Approximate location of trepanned cores.

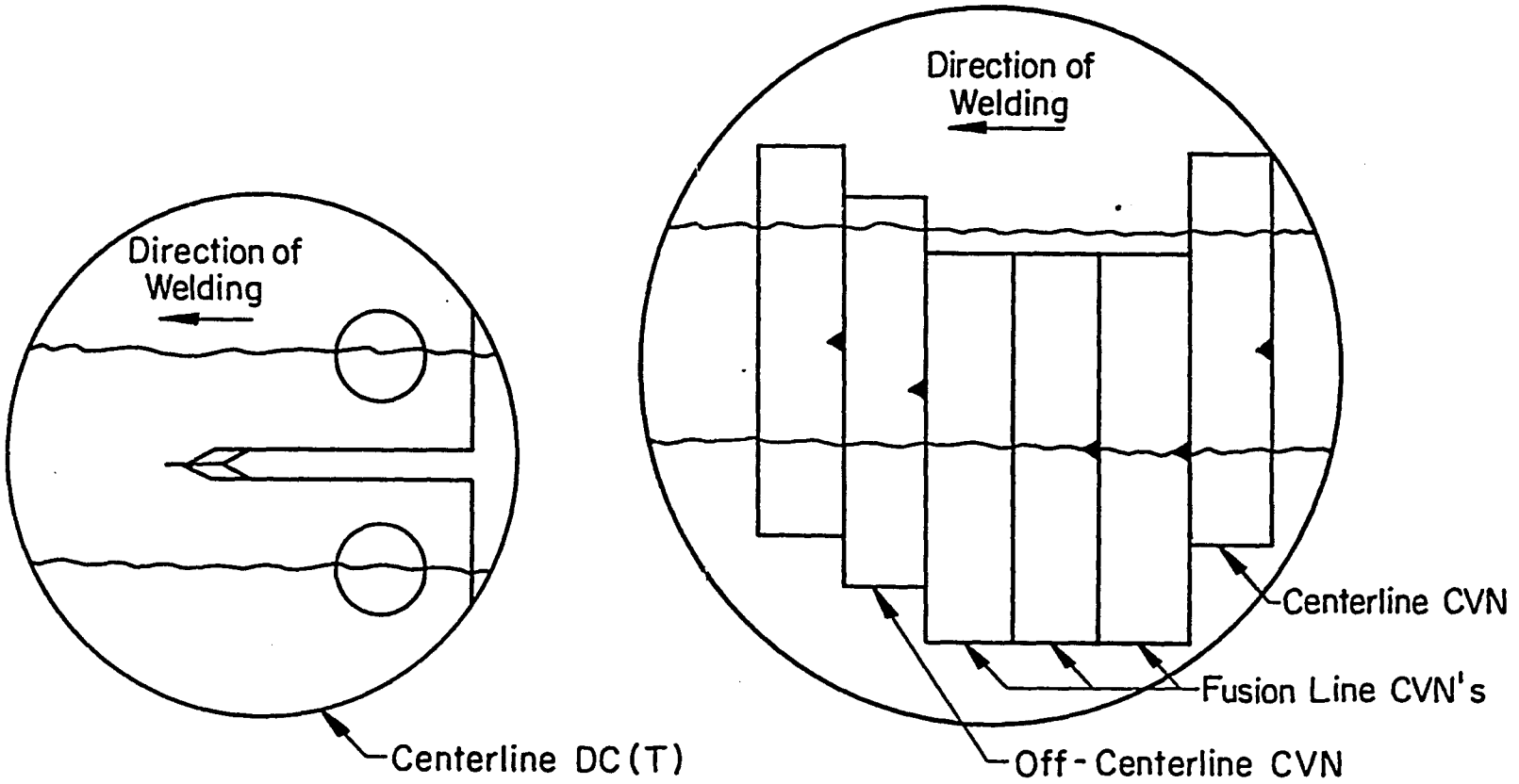

Sketch II - Typical layout of notch toughness specimens on trepanned cores.

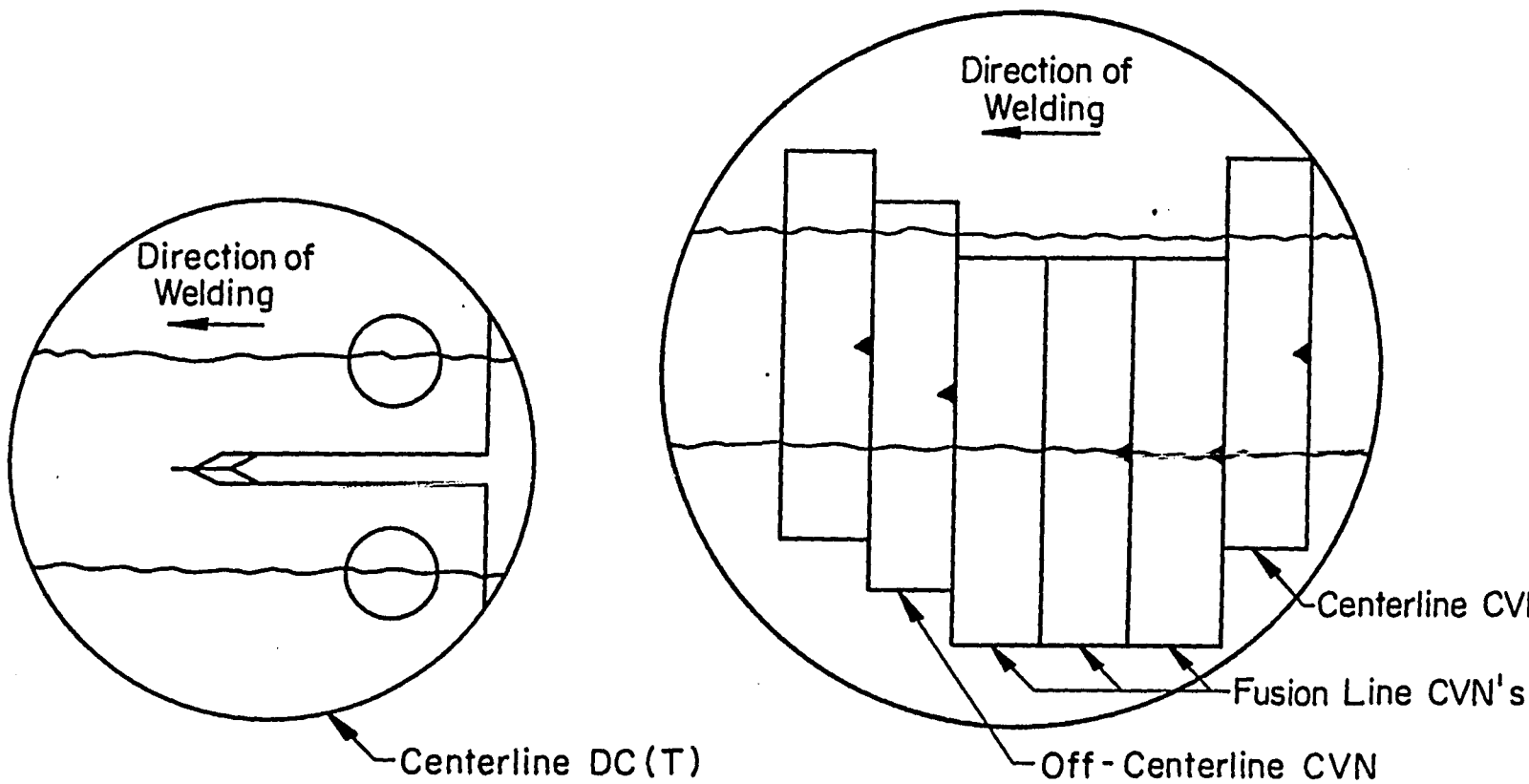

Sketch II - Typical layout of notch toughness specimens on trepanned cores.

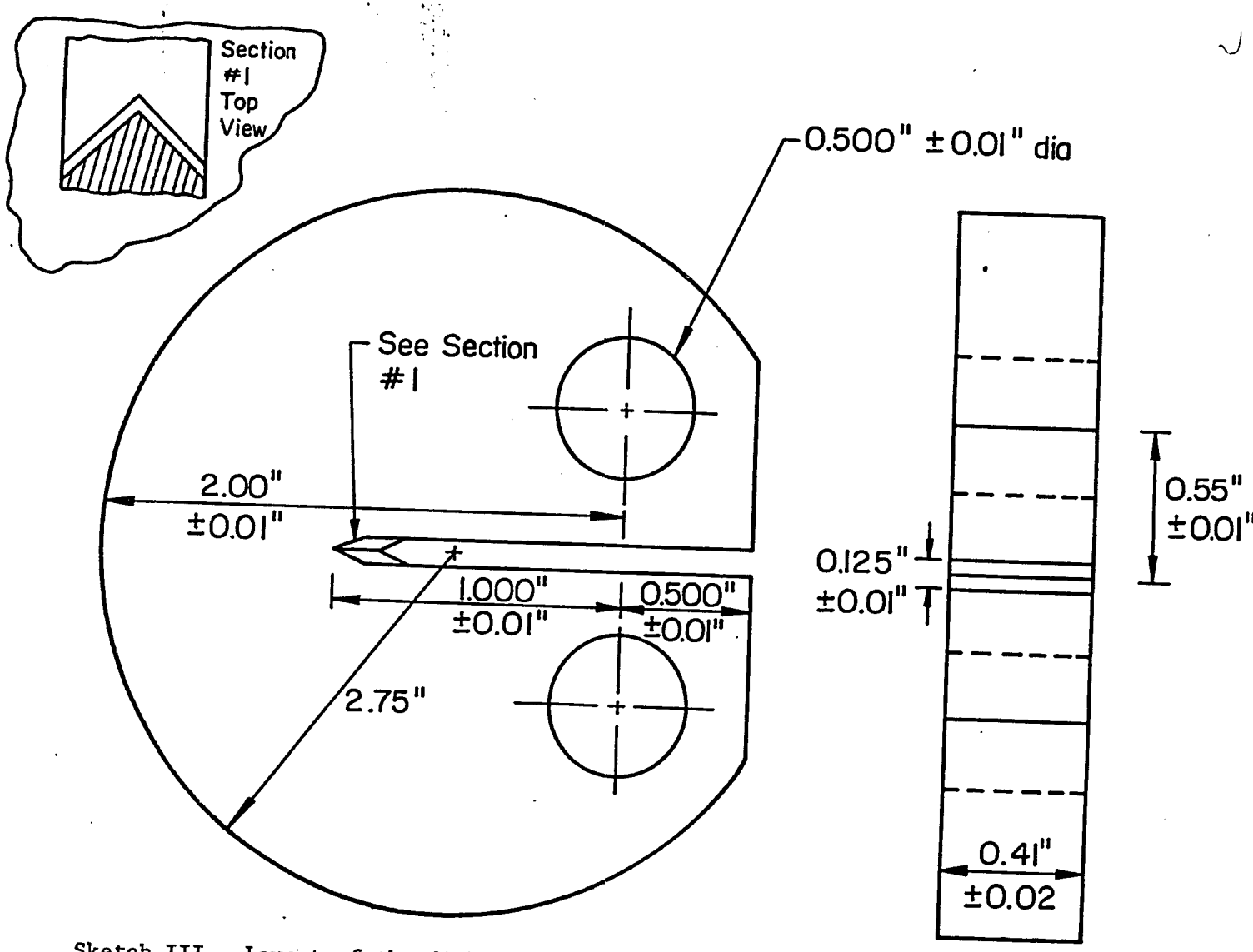

Sketch III - Layout of the disk shaped compact tension specimens used in this study.

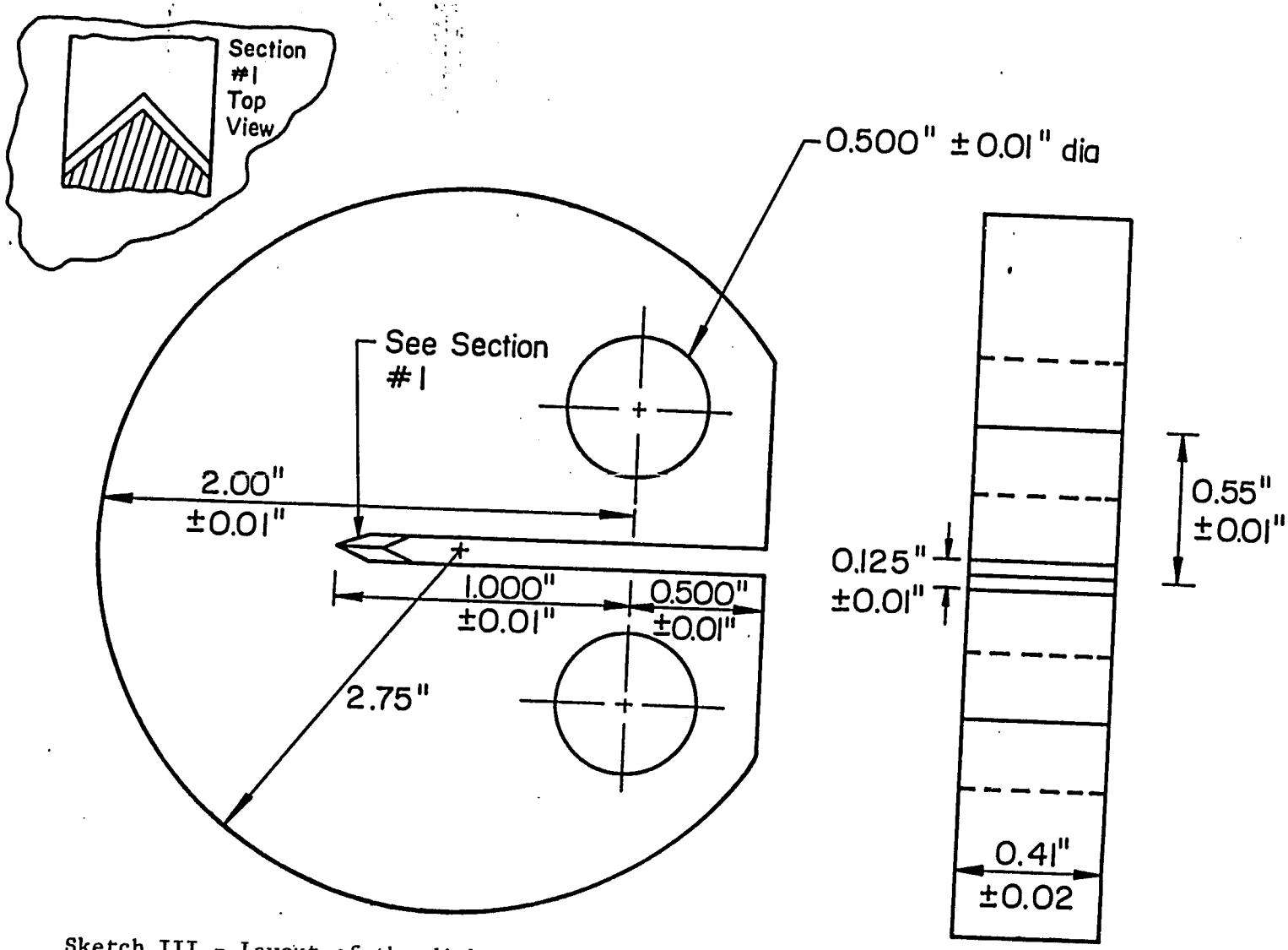

Sketch III - Layout of the disk shaped compact tension specimens used in this study.

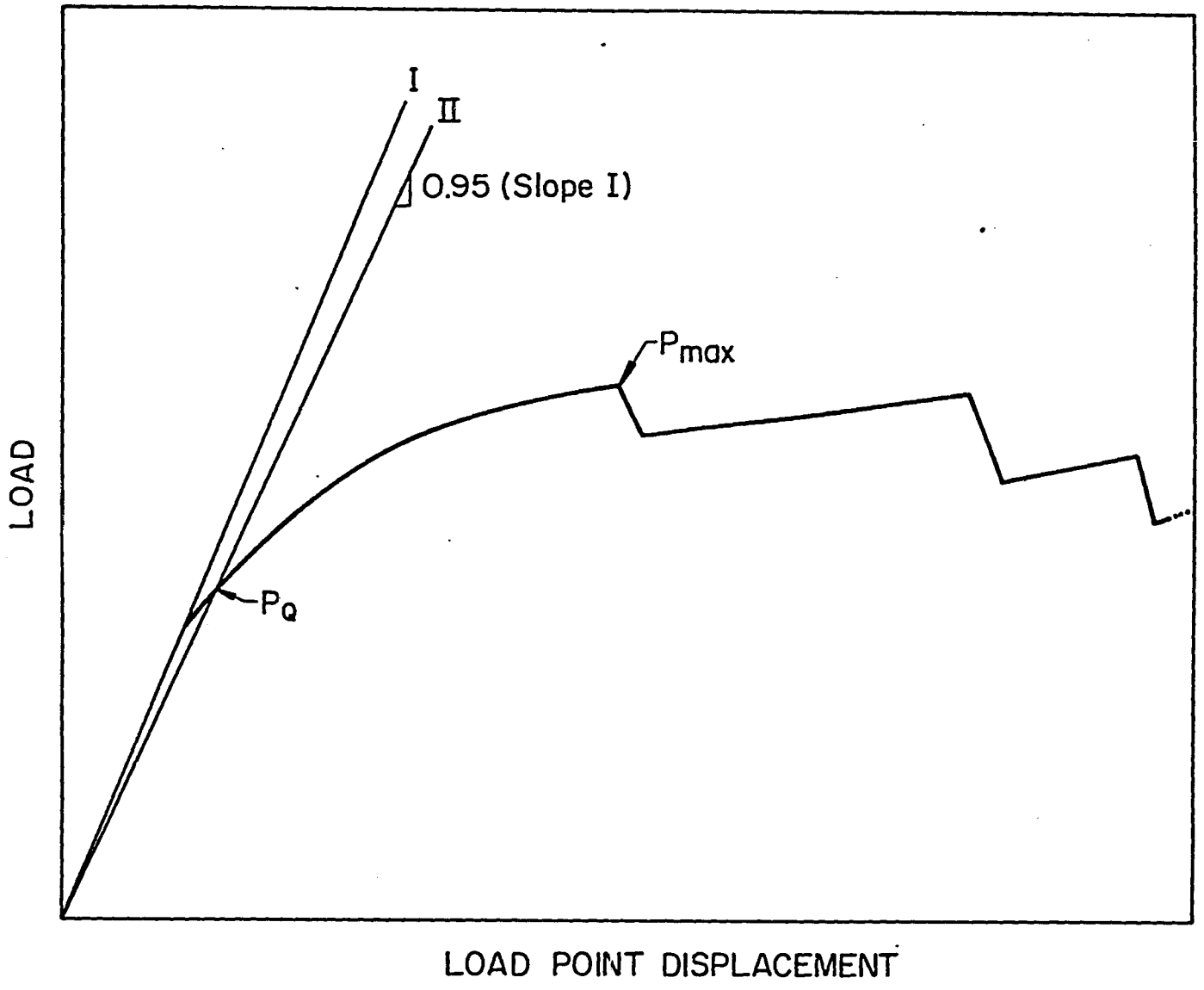

Sketch IV - Generalized load-load point displacement curve indicating elastic/plastic material behavior.

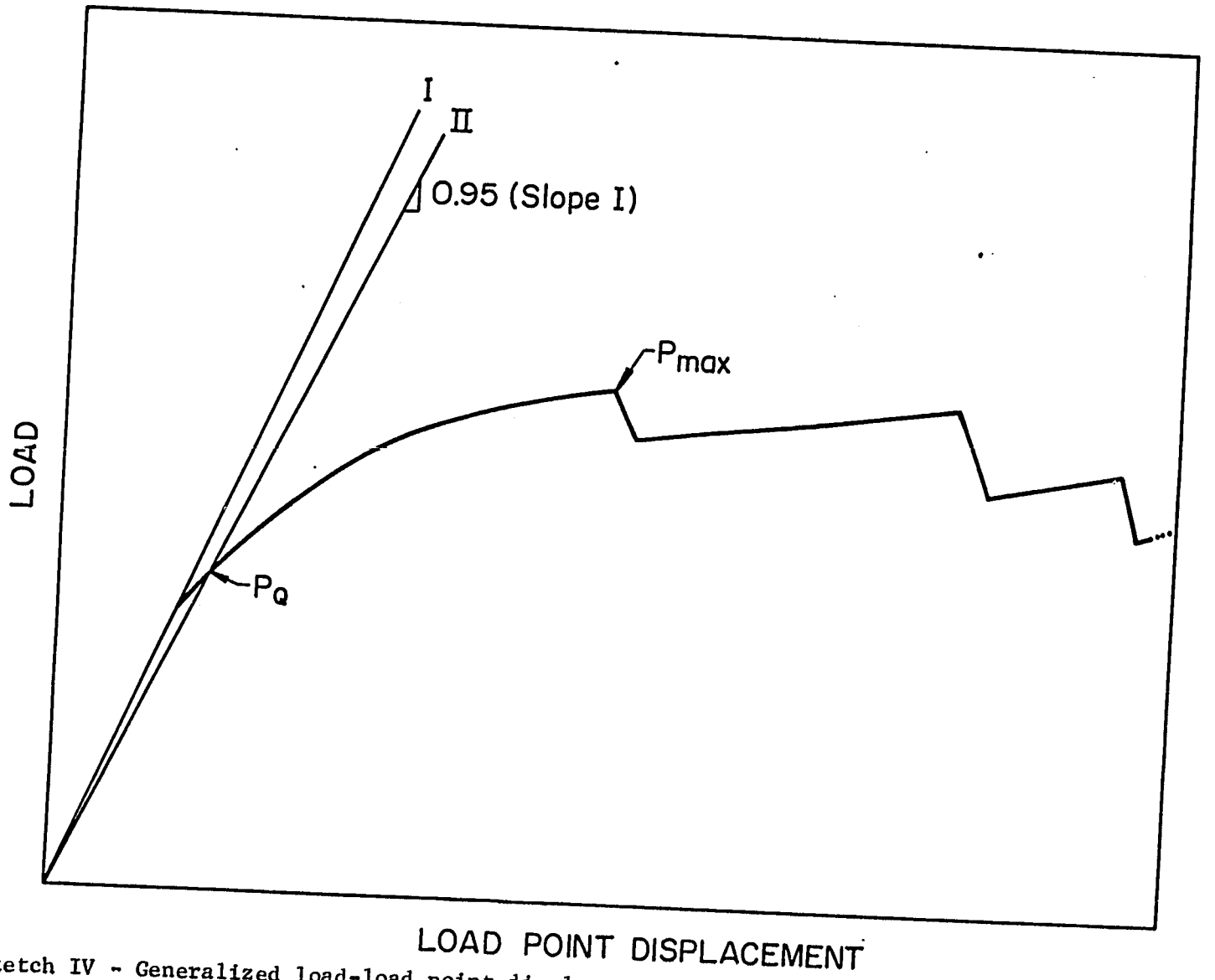

Sketch IV - Generalized load-load point displacement curve indicating elastic/plastic material behavior.

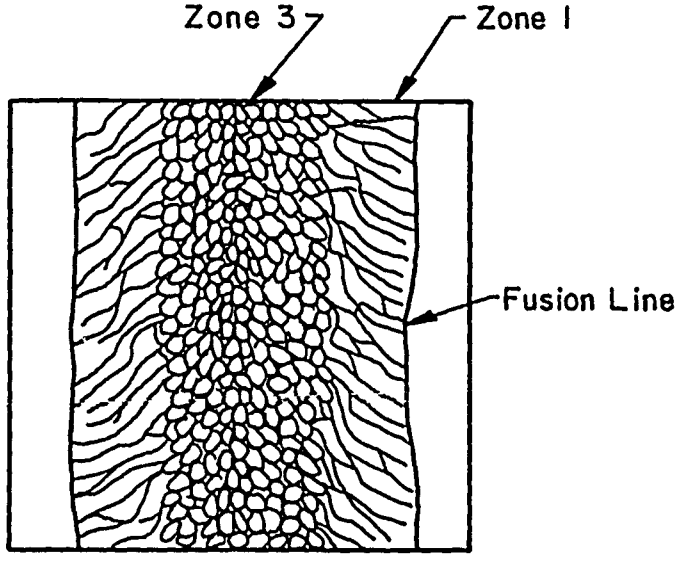

Sketch V - Prior austenite grain morphologies observed in the Kittanning Bridge electrogas weldments. Zone 1 depicts fine columnar crystals. Zone 3 depicts fine equiaxed crystals.

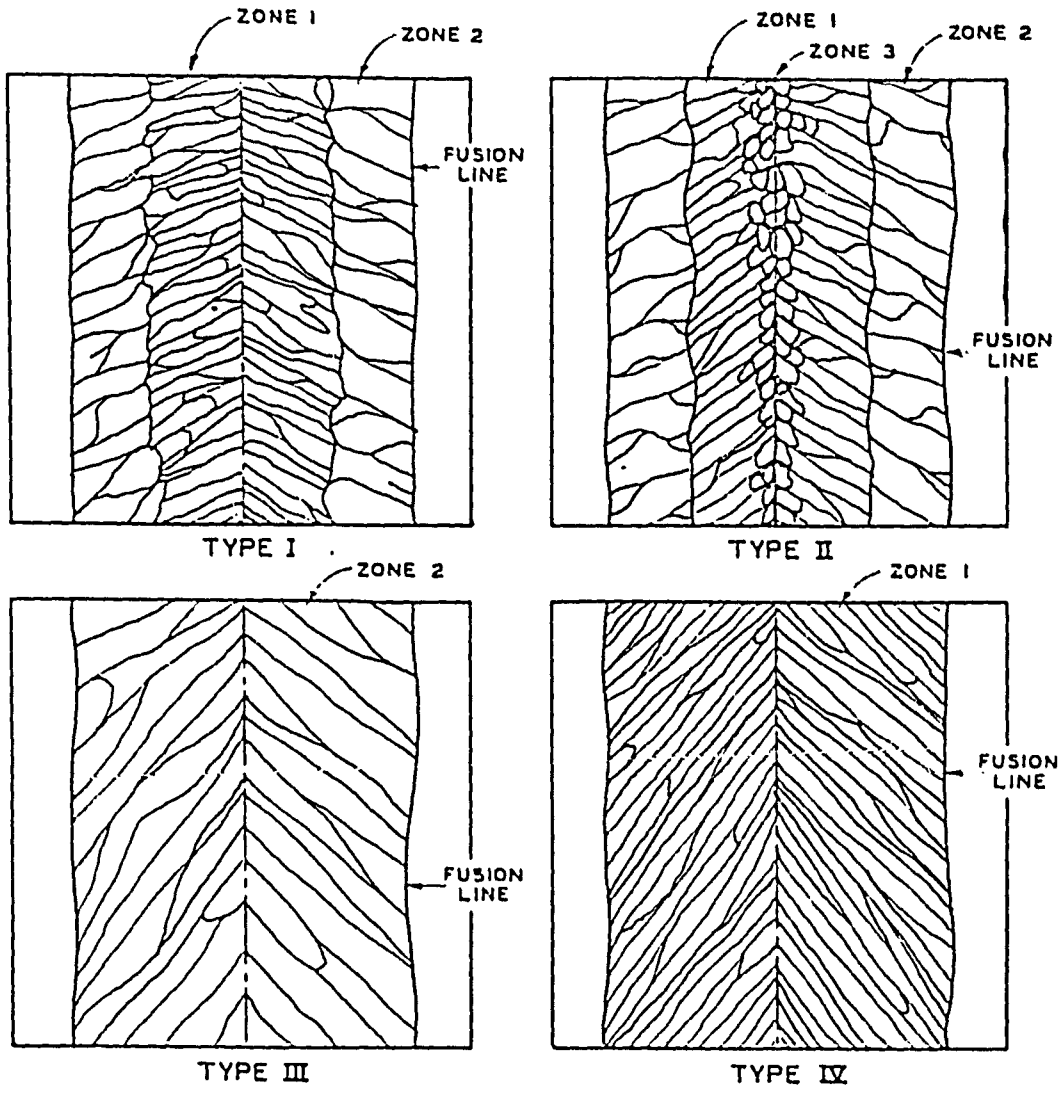

Sketch VI - Electroslag joint types, longitudinal section through the weld. Type I-coarse (Zone 2) and fine (Zone 1) columnar crystals. Type II-Zone 1 and 2 plus equiaxed crystals (Zone 3). Type III-all Zone 2 crystals. Type IV-all Zone 1 crystals (after Ref. 2).

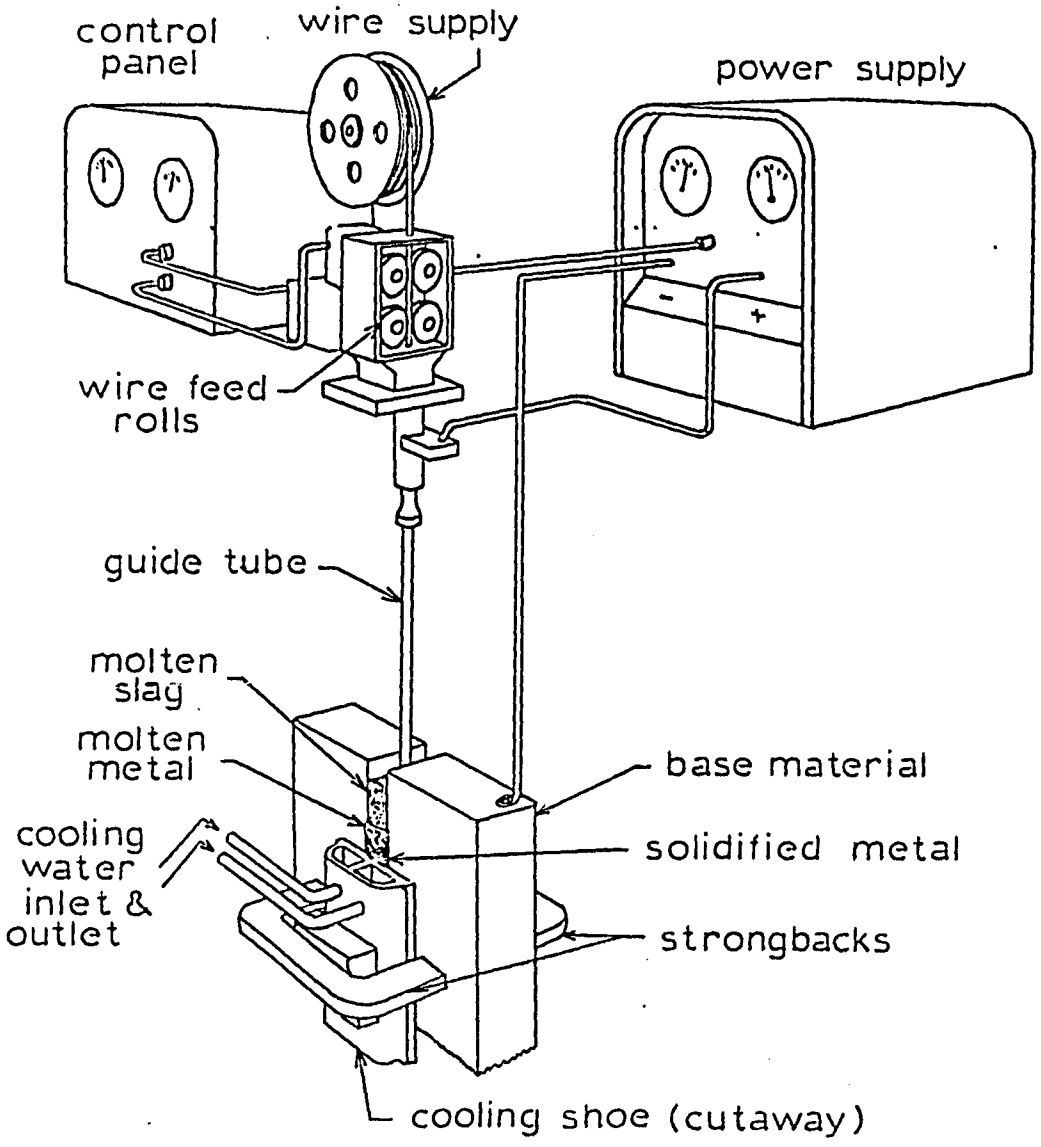

Figure 1 - General electroslag welding configuration (from ref. 26).

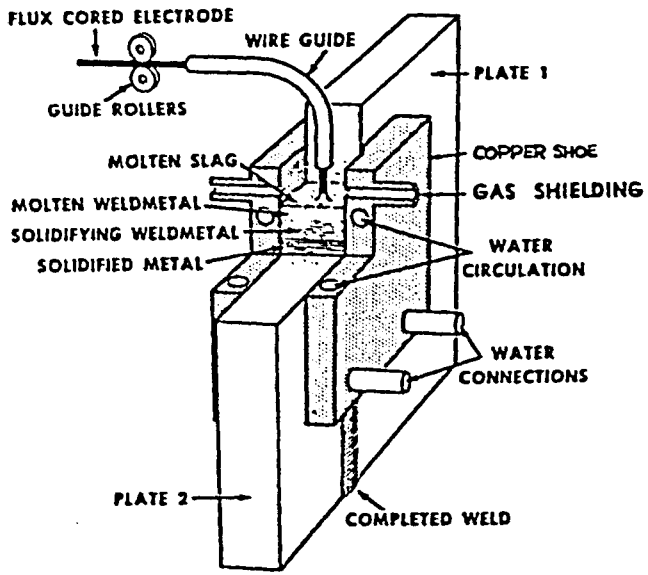

—Schematic drawing of shoes for electrogas welding

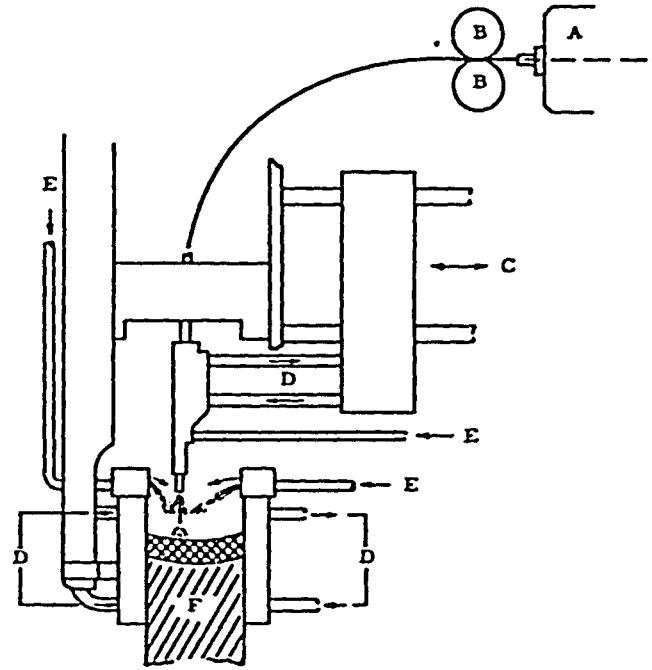

—Schematic of weld setup for electrogas welding. (A) Rotary wire straightener. (B) Drive rolls. (C) Oscillation. (D) Water. (E) Gas. (F) Weld

Figure 2 - General electrogas welding configuration (from ref. 1).

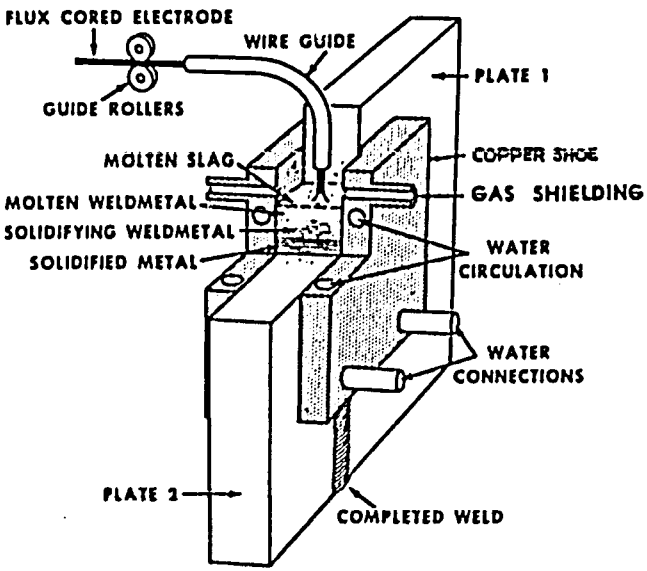

—Schematic drawing of shoes for electrogas welding

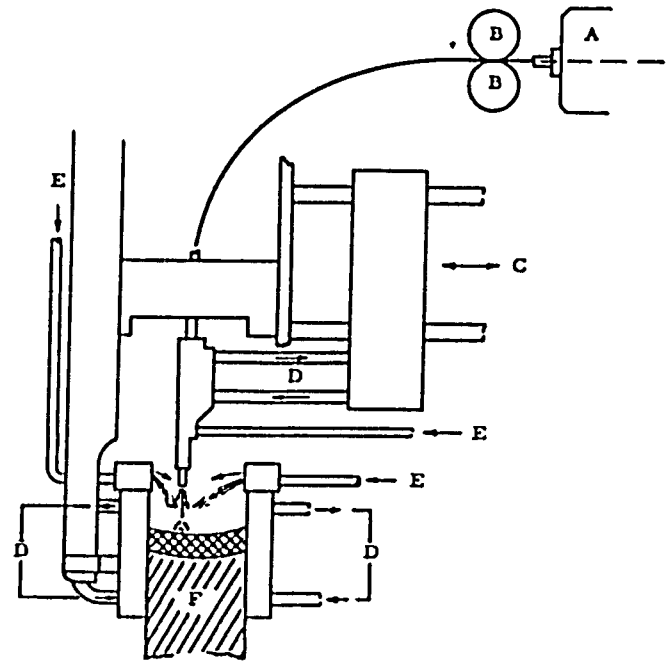

—Schematic of weld setup for electrogas welding. (A) Rotary wire straightener. (B) Drive rolls. (C) Oscillation. (D) Water. (E) Gas. (F) Weld

Figure 2 - General electrogas welding configuration (from ref. 1).

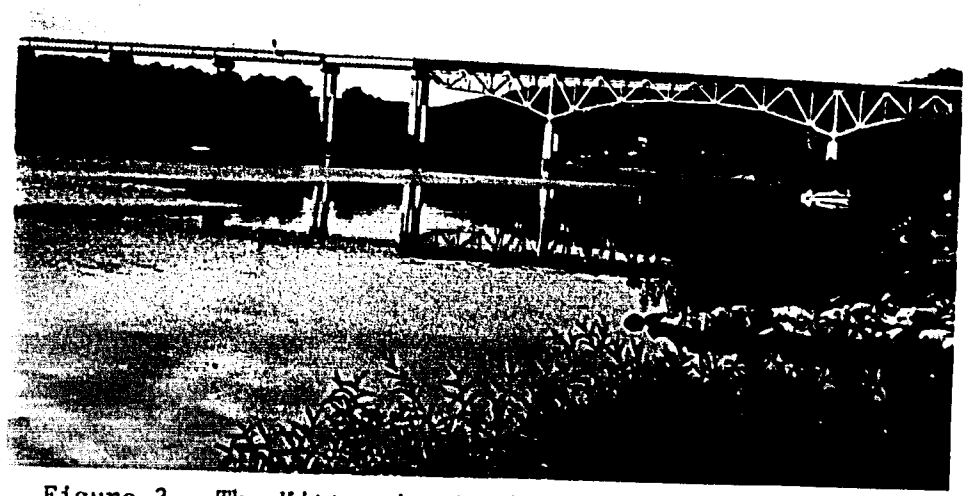

Figure 3 - The Kittanning Bridge viewed from the south.

Figure 4 - The Kittanning Bridge viewed from the north.

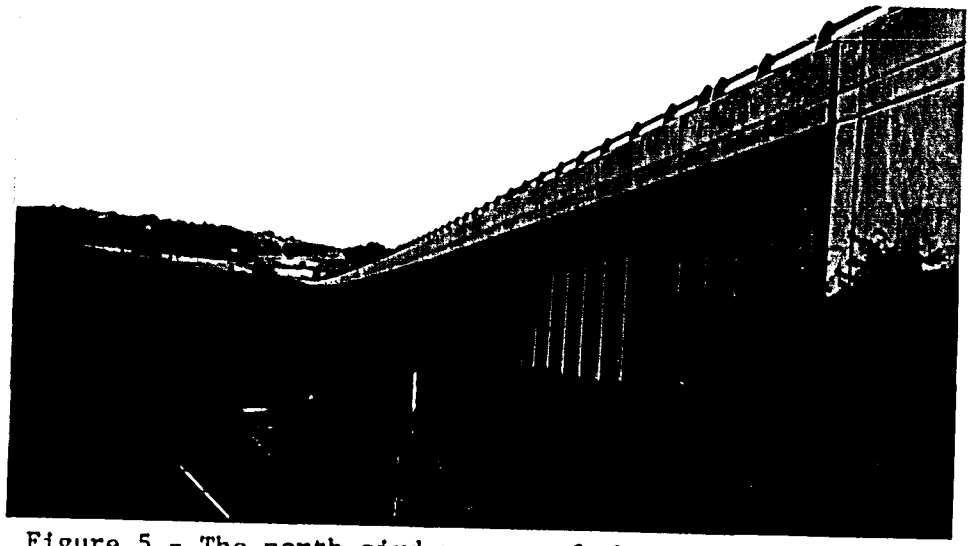

Figure 5 - The north girder span of the Kittanning Bridge viewed from the west.

Figure 6 - View of the Kittanning Bridge under-deck truss spans.

Figure 7 - View of floor beam #10 east showing the location of Core KF.

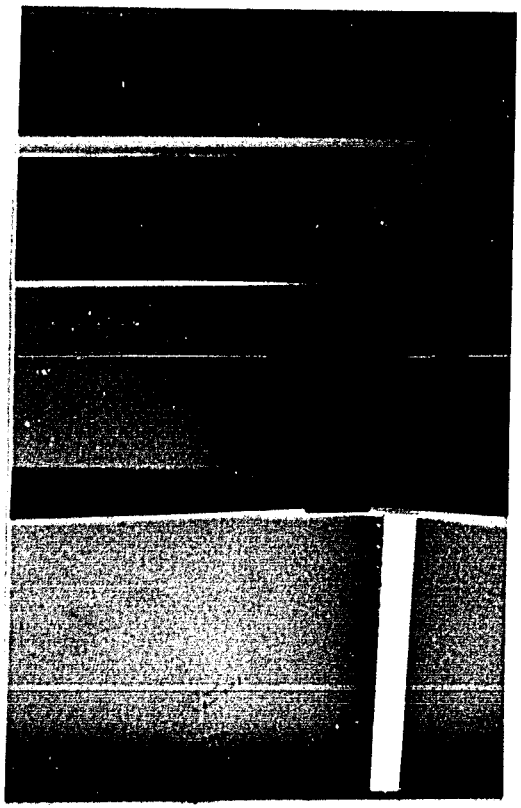

Figure 8 - View of girder 702G2D-south side showing the location of Core KG.

Figure 9 - View of girder U10-L11 at L11 showing the location of Core KC

Figures 10-12 - Ultrasonic inspection, trepanning, and post inspection by die penetrant of Core KK located at L11-L13 at L11.

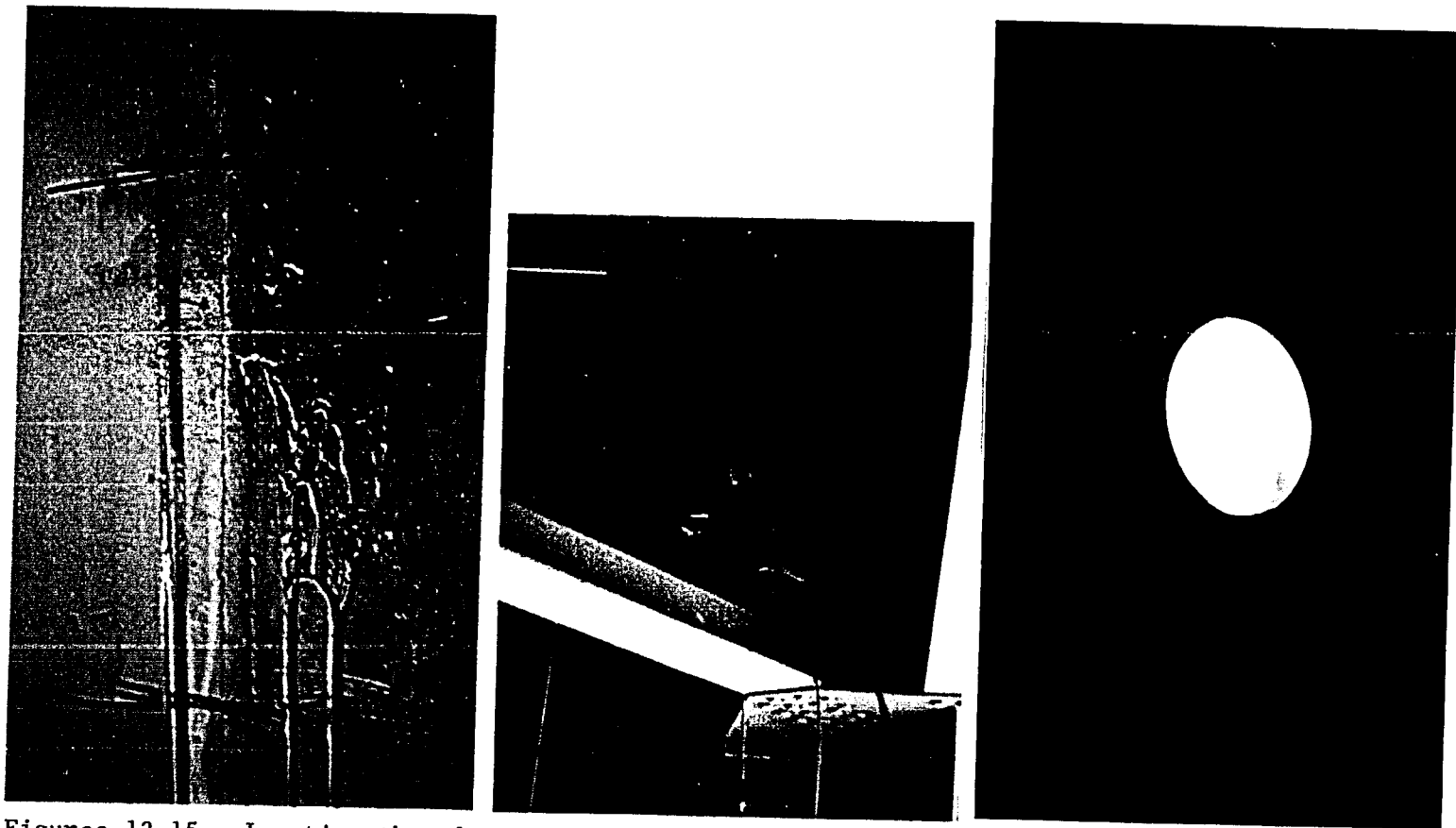

Figures 13-15 - Locating the ultrasonic indication, trepanning, and post die penetrant inspection of Core KLlocated in girder 103G2D.

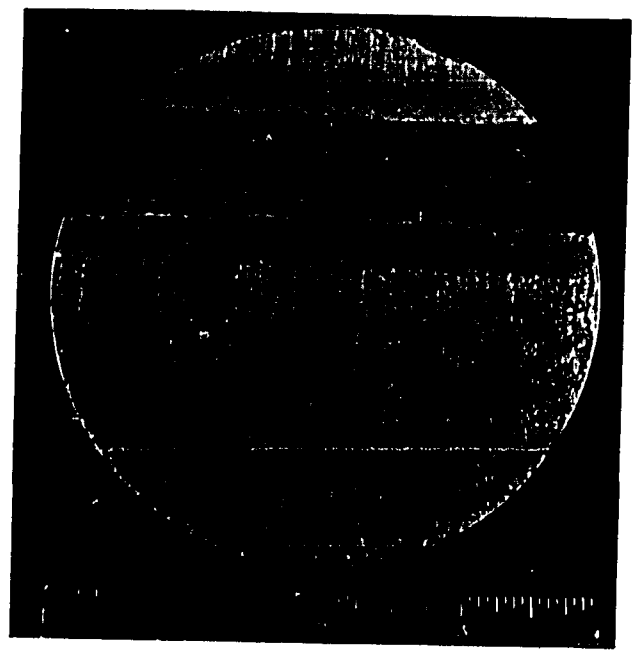

Figure 16 - Photomacrograph of Core KB after macroetching.
5% nital
Mag: 0.75X

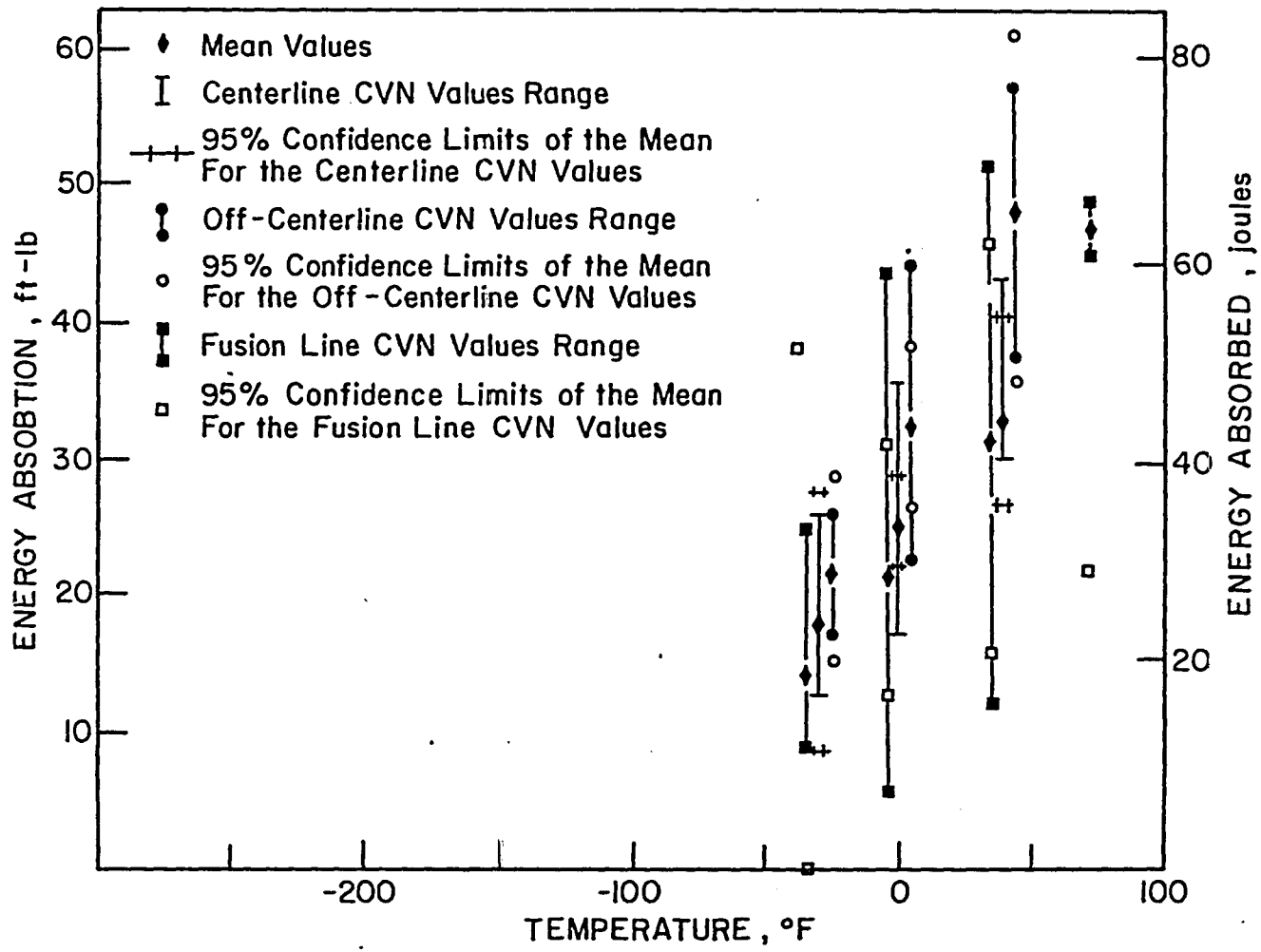

Figure 17 - Scatter chart of Charpy vee notch absorbed energy values.

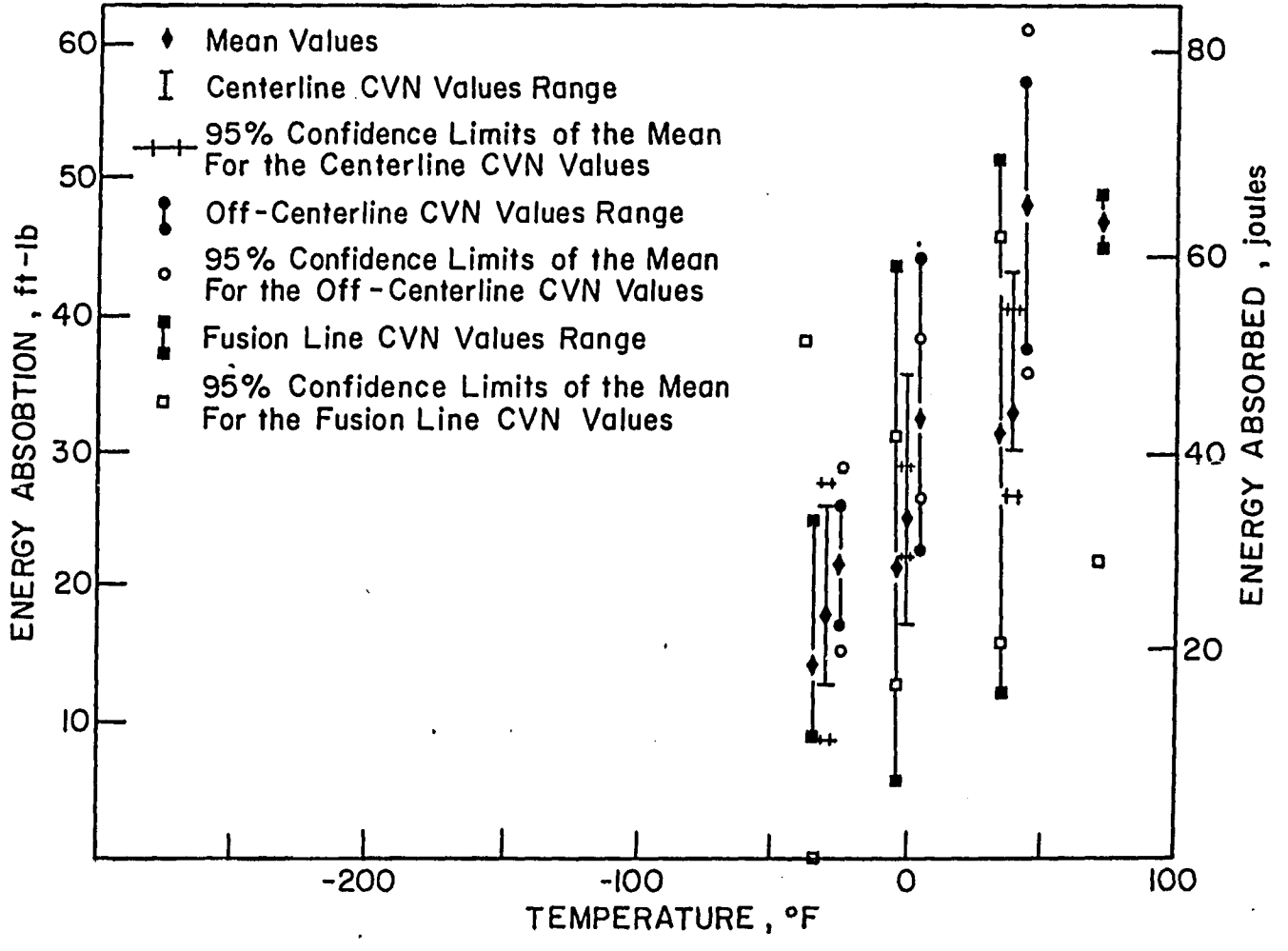

Figure 17 - Scatter chart of Charpy vee notch absorbed energy values.

Figure 18 - Photomacrograph showing the fracture surface morphology from the disk-shape compact tension specimens machined from Core KD4 and KE4. Mag: 1X

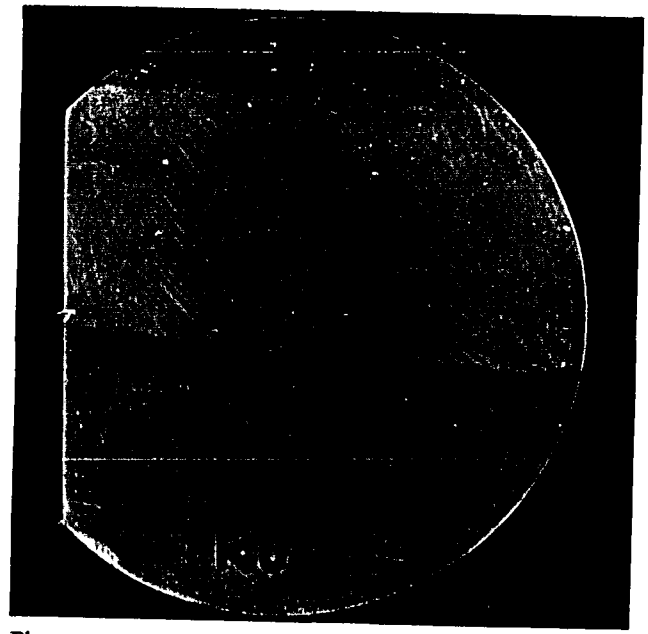

Figure 19 - Photomacrograph of Core KJ after rough polishing and macroetching.
5% nital
Mag: 1X

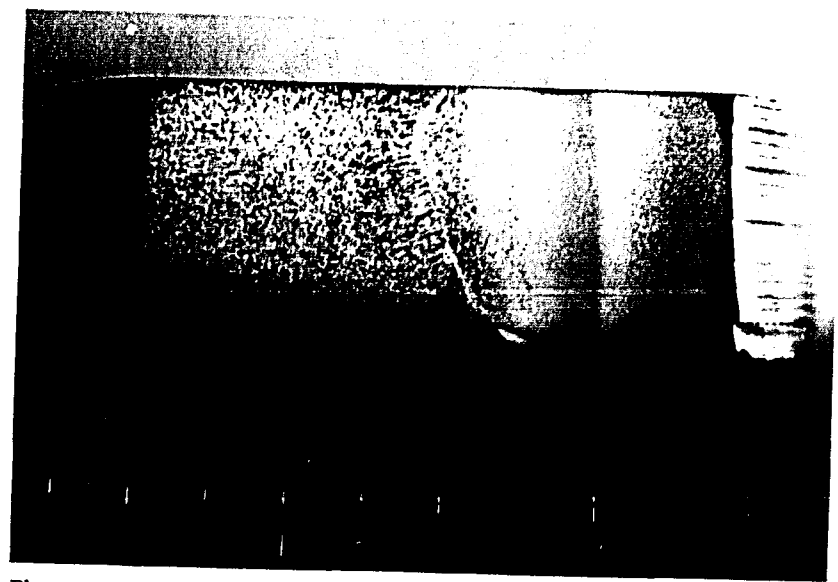

Figure 20 - Photomacrograph of a transverse section of Core KJ after polishing and etching.
2% nital
Mag: 1.6X

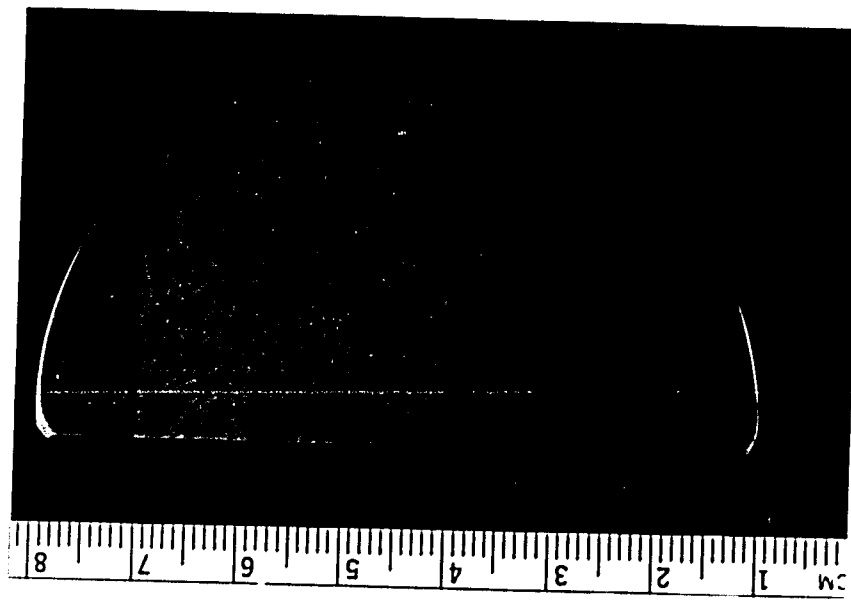

Figure 21 - Photomacrograph of a Core KJ after polishing and etching. This weld has a form factor of ~ 2.5. Note the fine elongated grain structure near the weld metal edge and the fine equiaxed grain structure near the weld centerline.
2% nital
Mag: 1.4X

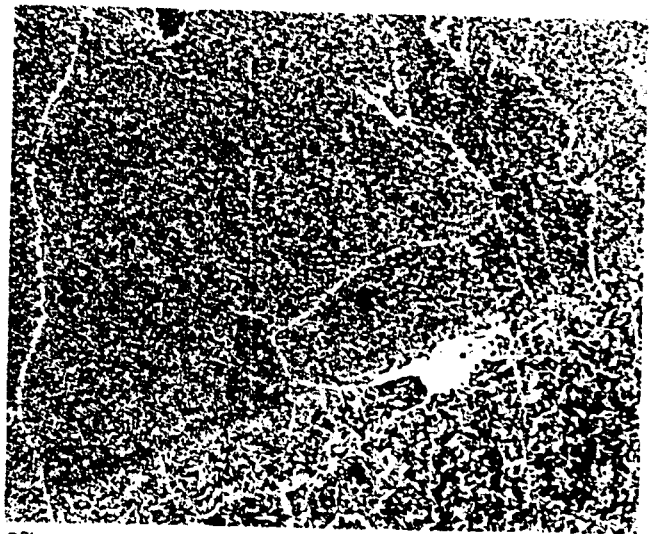

2% nital 50X

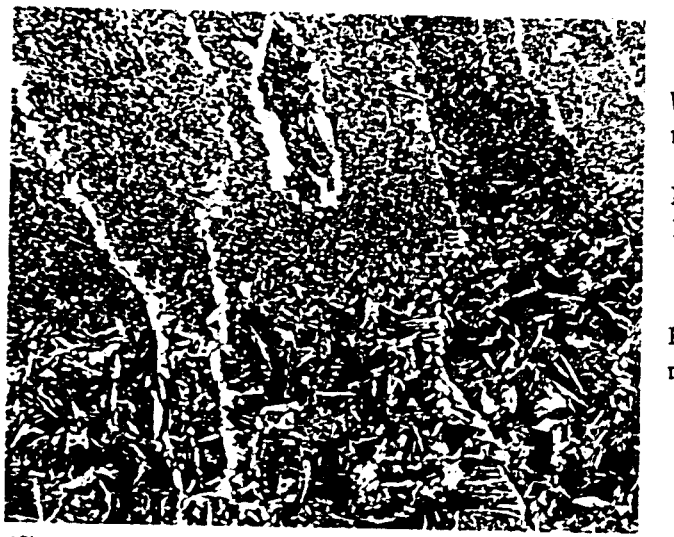

2% nital Bright field 100X

Figures 22-24 - Photomicrographs from sample KJ showing the characteristics of the weld fusion line.

2% nital Dark field 100X

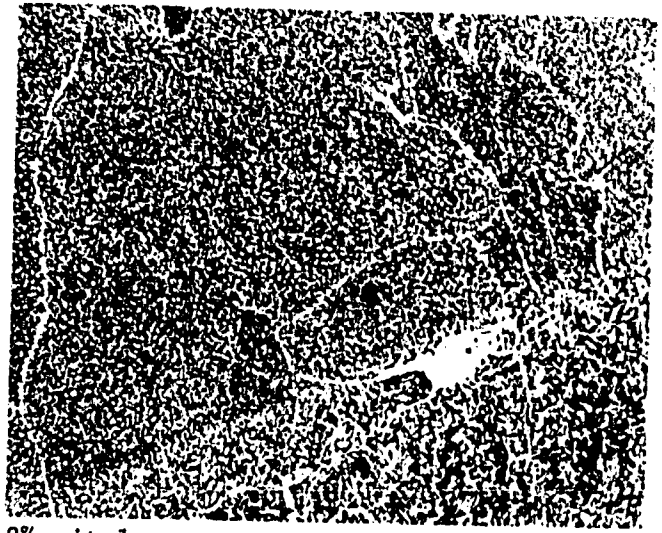

Fusion line

2% nital 50X

Weld metal

Fusio line

Base metal

2% nital Bright field 100X

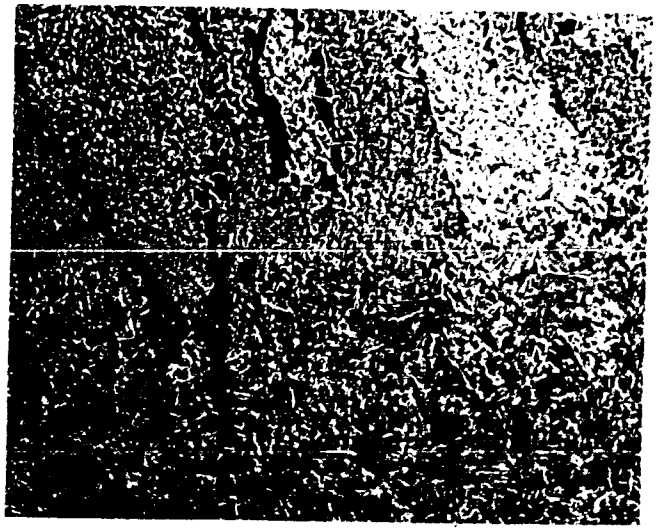

Weld metal

Fusion line

Base metal

2% nital Dark field 100X

Figures 22-24 - Photomicrographs from sample KJ showing the characteristics of the weld fusion line.

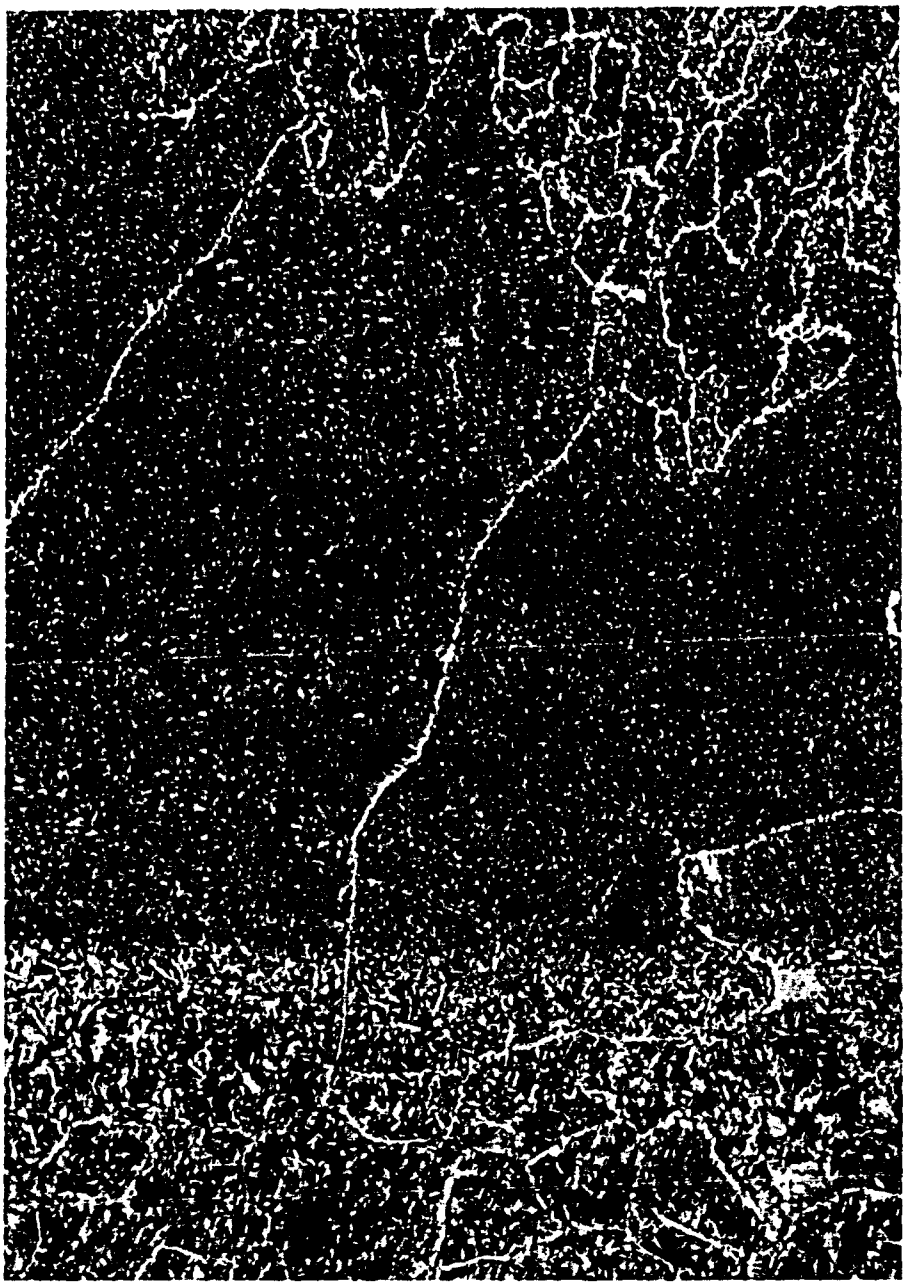

Figure 25 - Photomicrograph showing epitaxial growth of the weld metal from the base metal. Note also the change from elongated prior austenite grains to equiaxed prior austenite grain away from the fusion line.
2% nital

Mag: ~ 140X

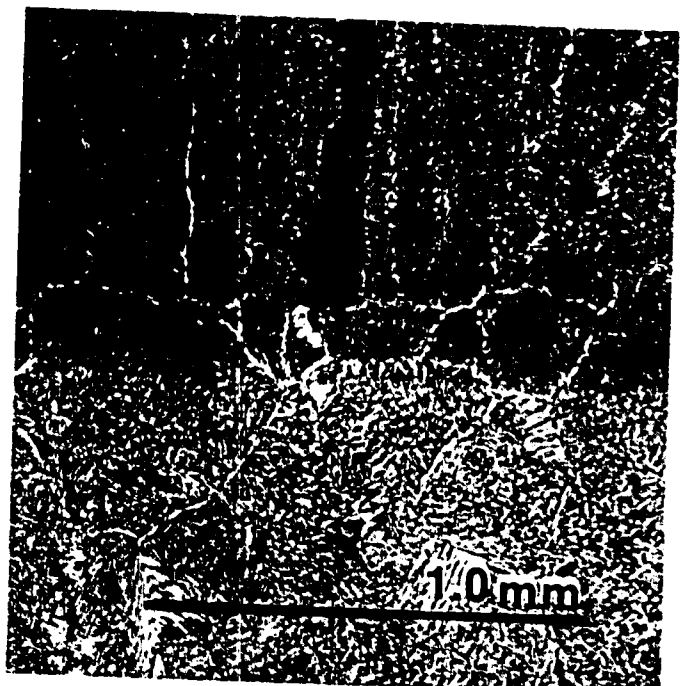

Figures 26-28 - Photomicrographs of the fusion line microstructure observed in sample KL. Note the partial melting of the base metal prior austenite grains.

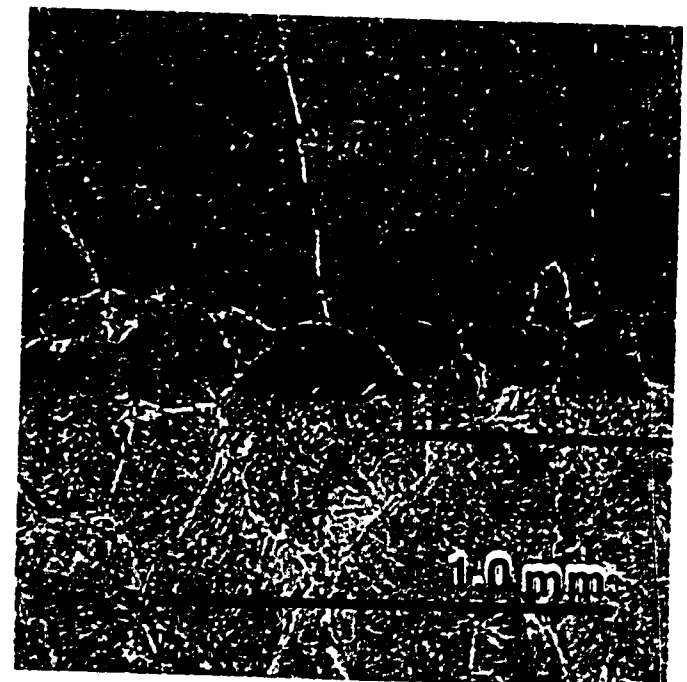

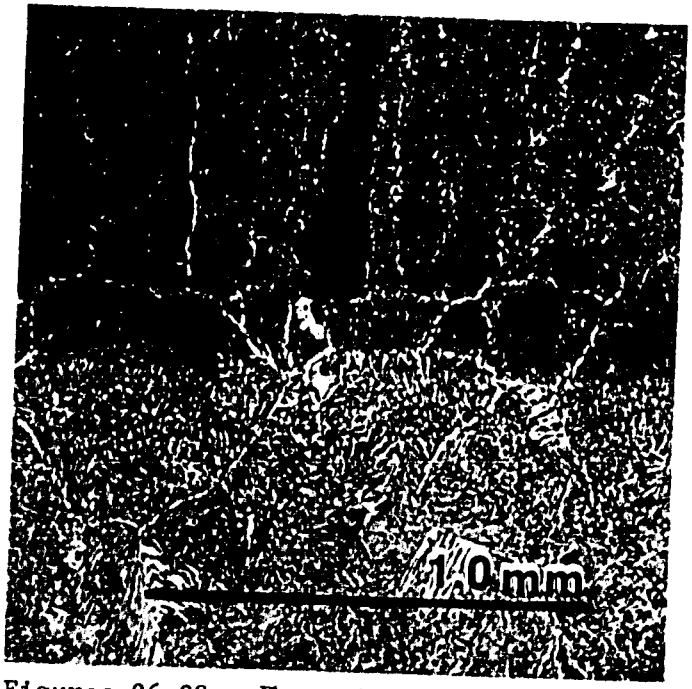

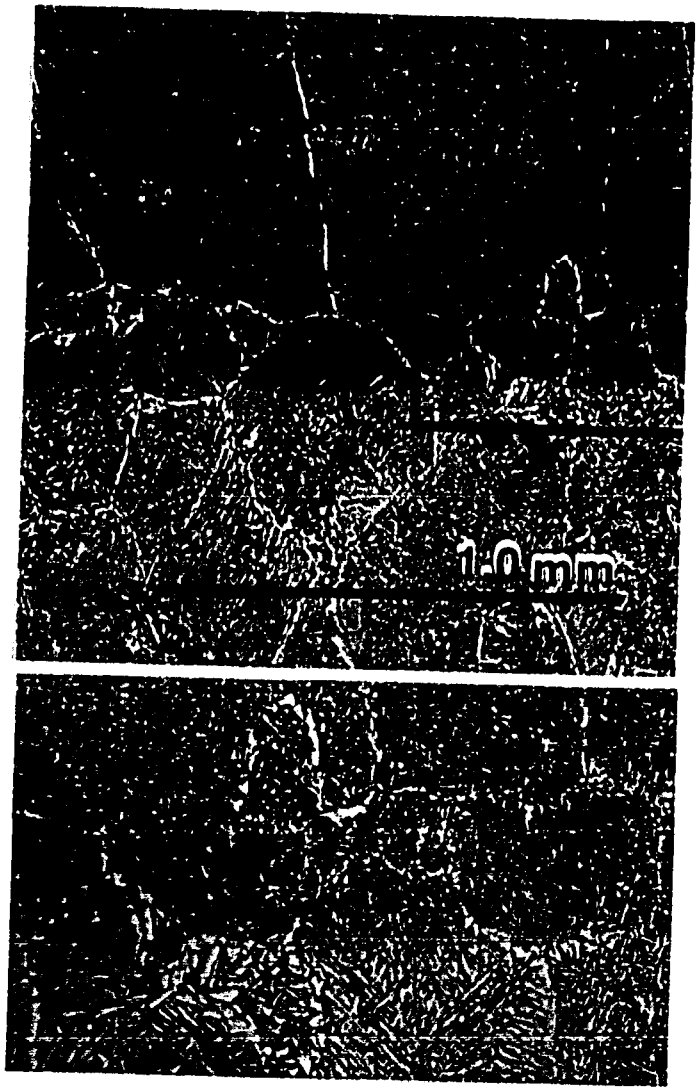

Figures 26-28 - Photomicrographs of the fusion line microstructure observed in sample KL. Note the partial melting of the base metal prior austenite grains.

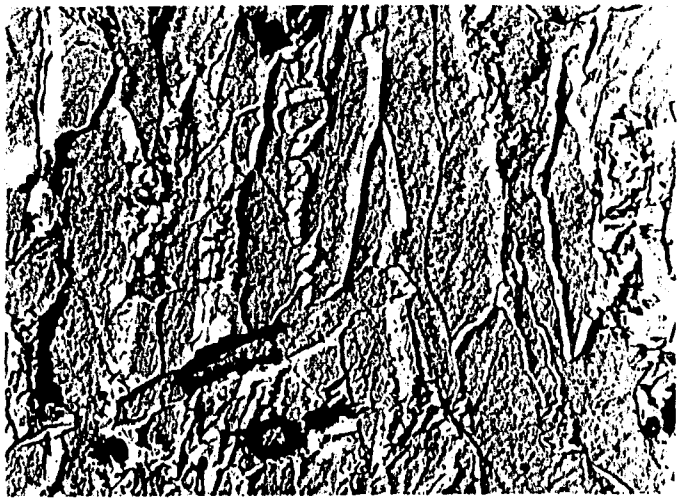

Figure 29 - Transmission electron micrograph showing the weld metal morphology from sample KJ. Chromium shadowed carbon-acetate replica. 2% nital Mag: 5000X

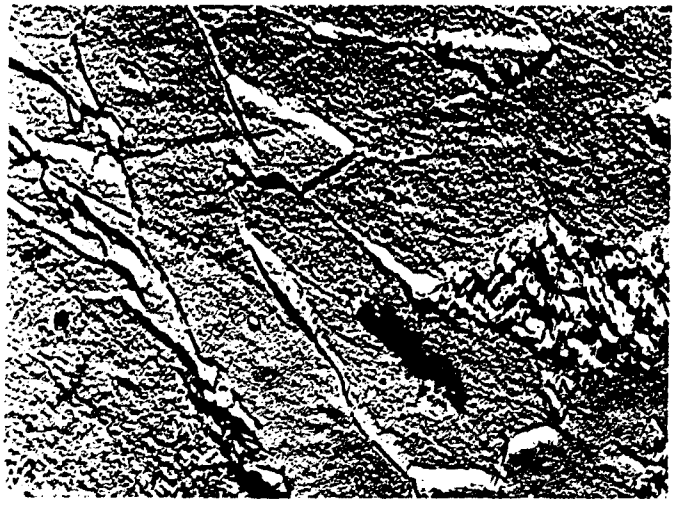

Figure 30 - Transmission electron micrograph showing the weld metal morphology from sample KJ. Chromium shadowed carbon-acetate replica. 2% nital Mag: 11,000X

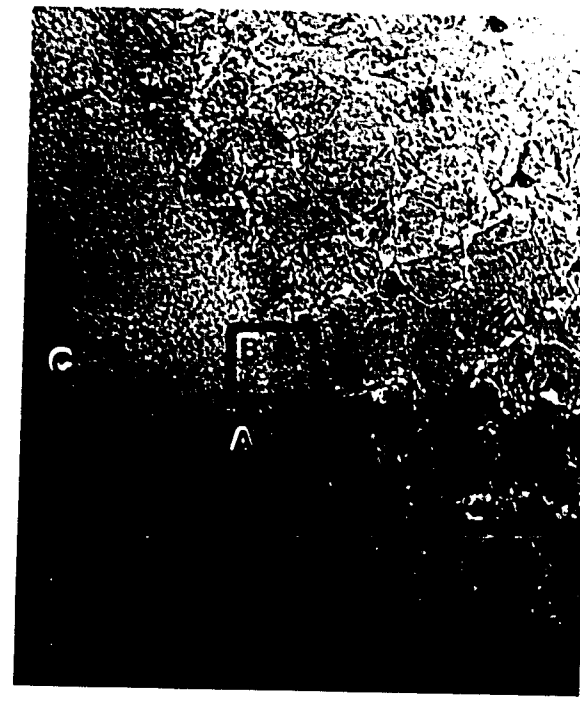

Figure 31 - Scanning electron micrograph from sample KC6 showing the weld fusion zone. Mag: 60X/SEM

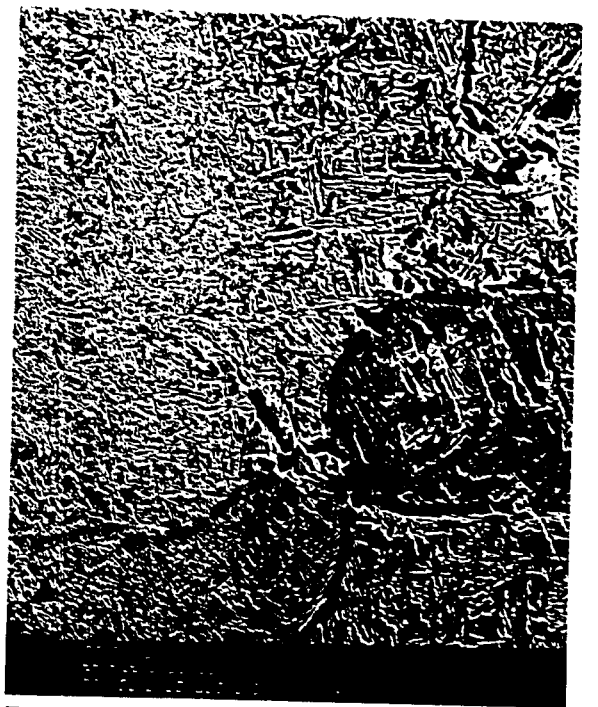

Figure 32 - Enlarged view from area "A" in Fig. 31.
Mag: 160X/SEM

Figure 33 - Enlarged view of Fig. 32.
Mag: 400X/SEM

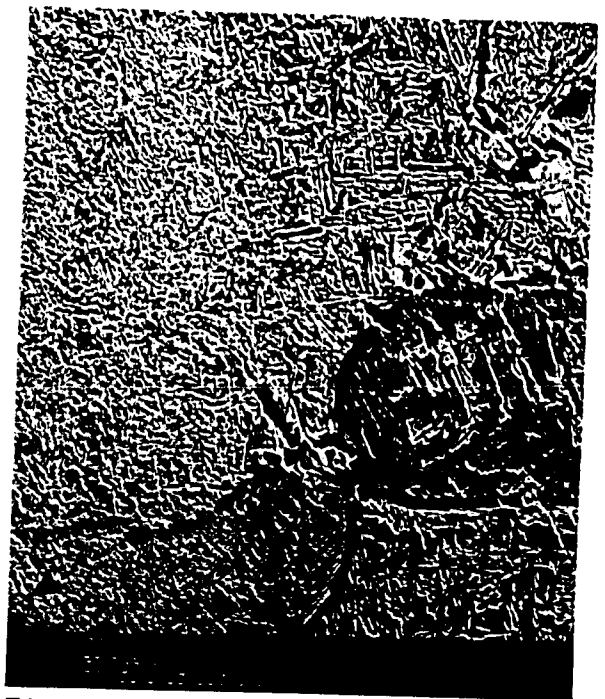

Figure 32 - Enlarged view from area "A" in Fig. 31.
Mag: 160X/SEM

Figure 33 - Enlarged view of Fig. 32.
Mag: 400X/SEM

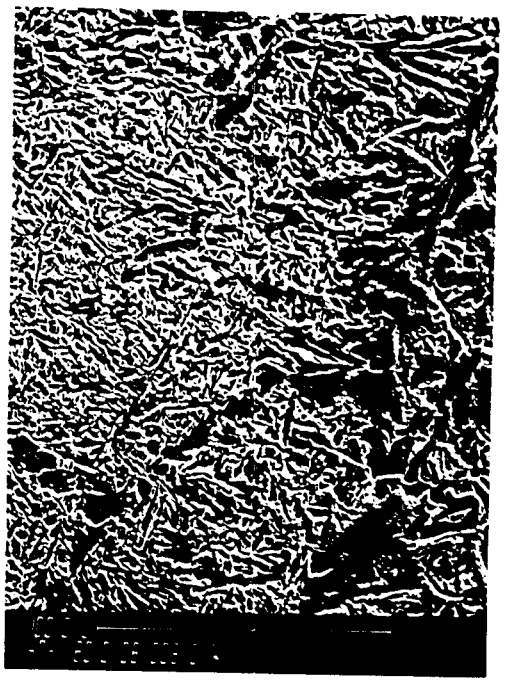

Figure 34 - Scanning electron micrograph showing area "B" in Fig. 31.
Mag: 400X/SEM

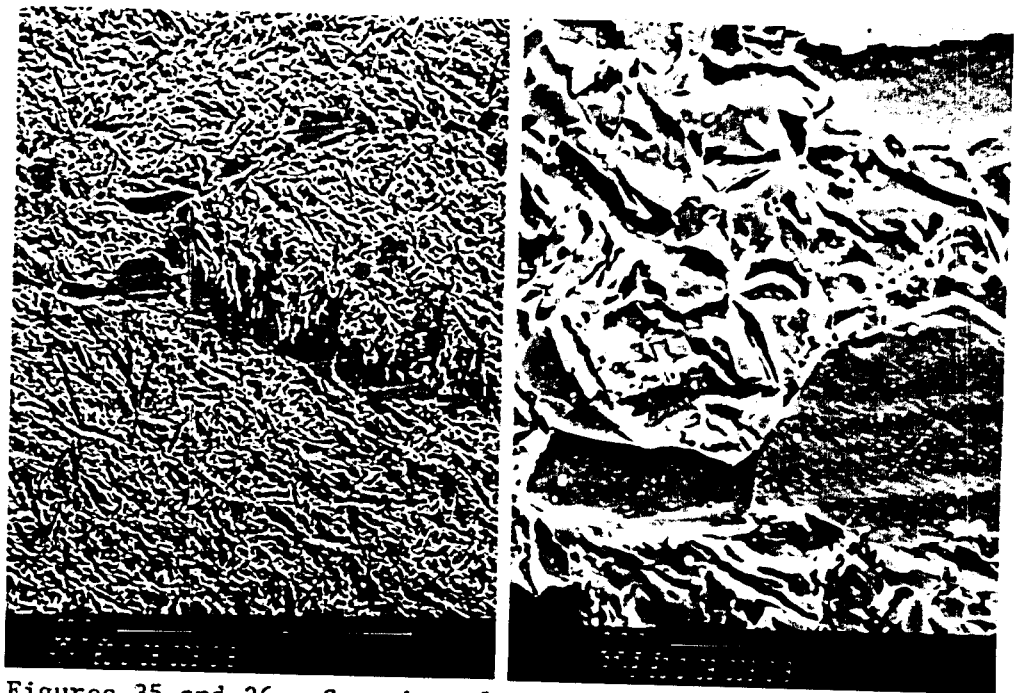

Figures 35 and 36 - Scanning electron micrographs showing area "C" in Fig. 31.
Mag. 400X, 2000X/SEM

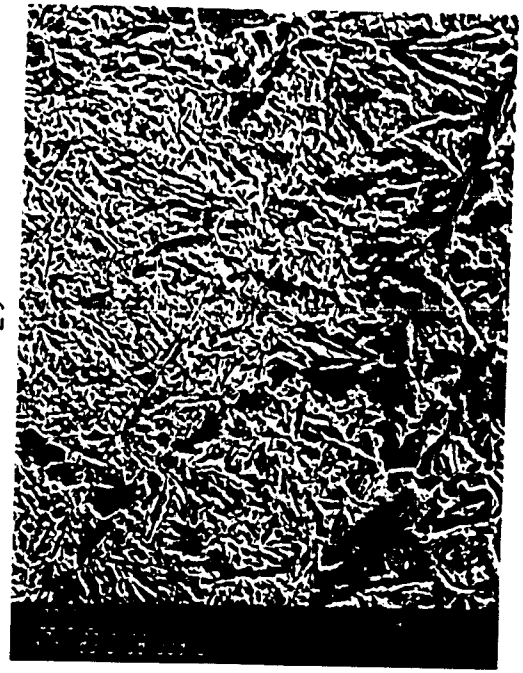

Figure 34 - Scanning electron micrograph showing area "B" in Fig. 31.
Mag: 400X/SEM

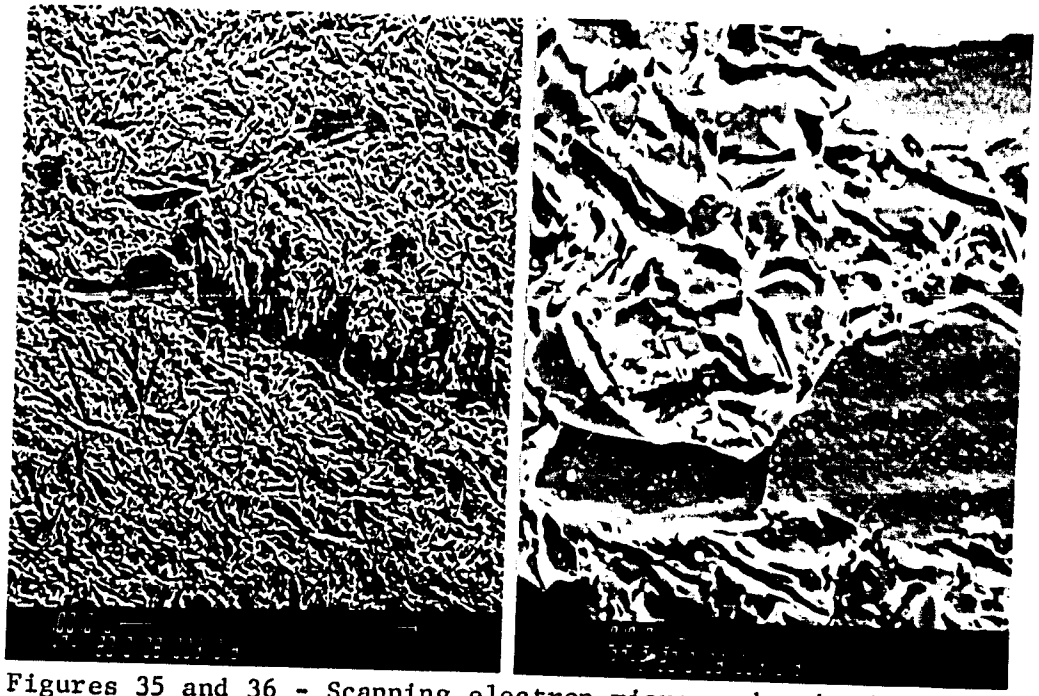

Figures 35 and 36 - Scanning electron micrographs showing area "C" in Fig. 31.
Mag. 400X, 2000X/SEM

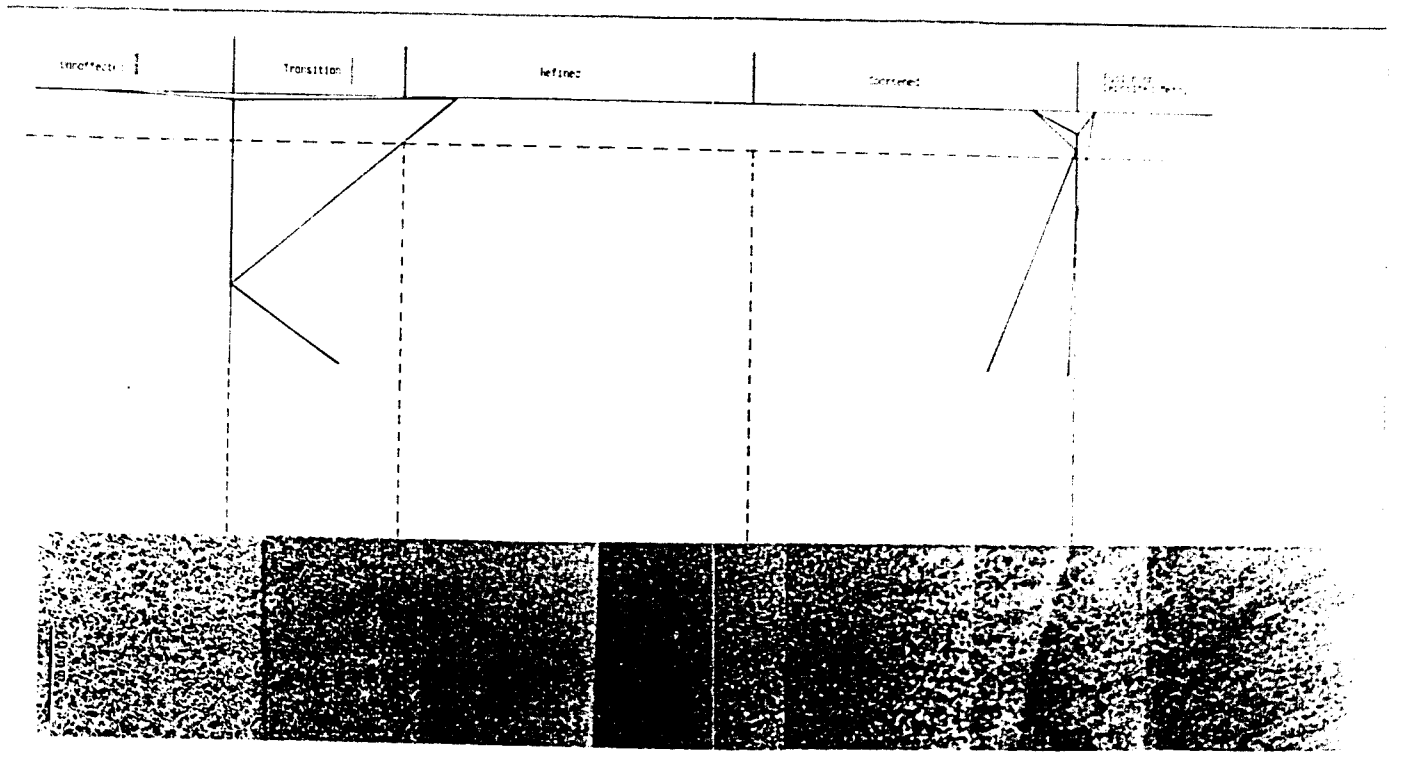

Figure 37 - Photomicrograph showing the base metal heat affected zones with a portion of an $Fe\text{-}Fe_3C$ diagram depicting the character of each zone.

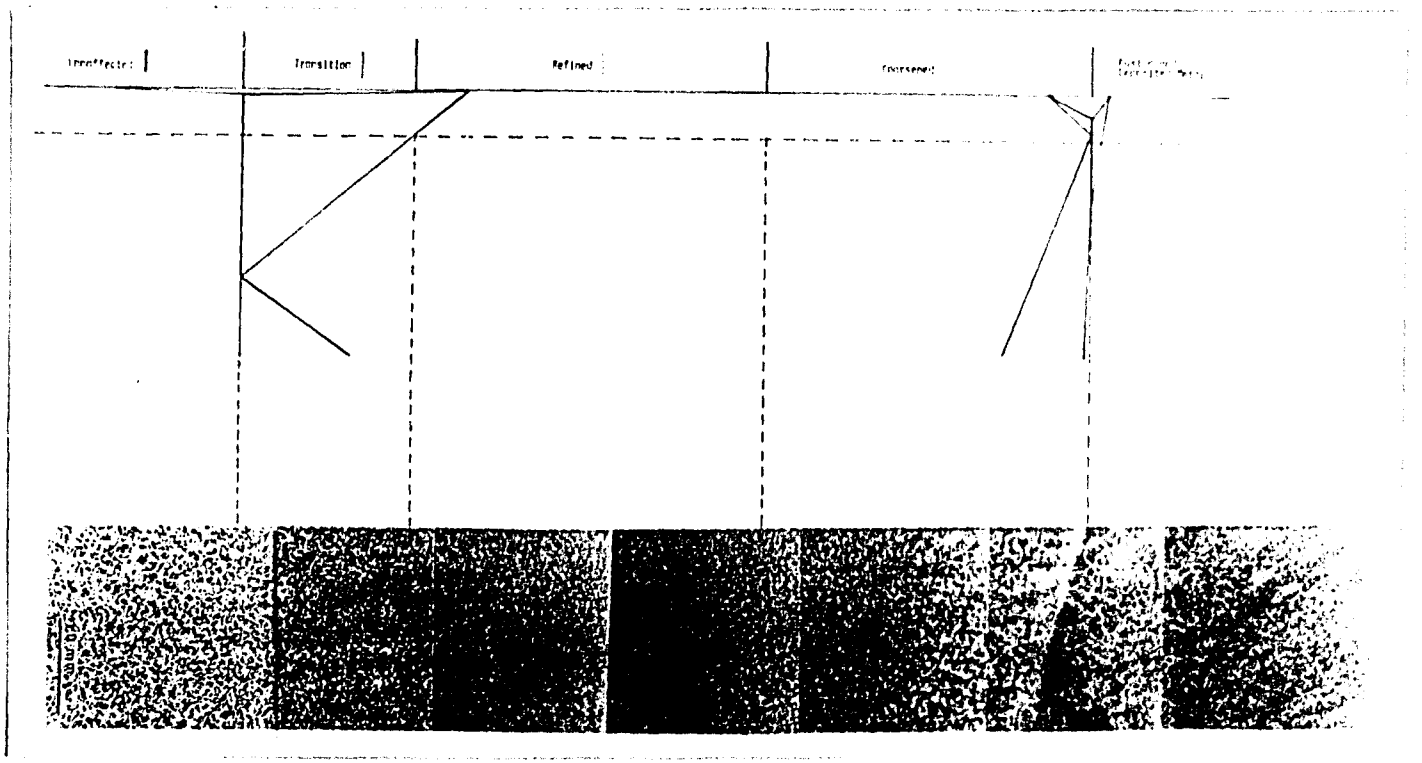

Figure 37 - Photomicrograph showing the base metal heat affected zones with a portion of an $Fe-Fe_3C$ diagram depicting the character of each zone.

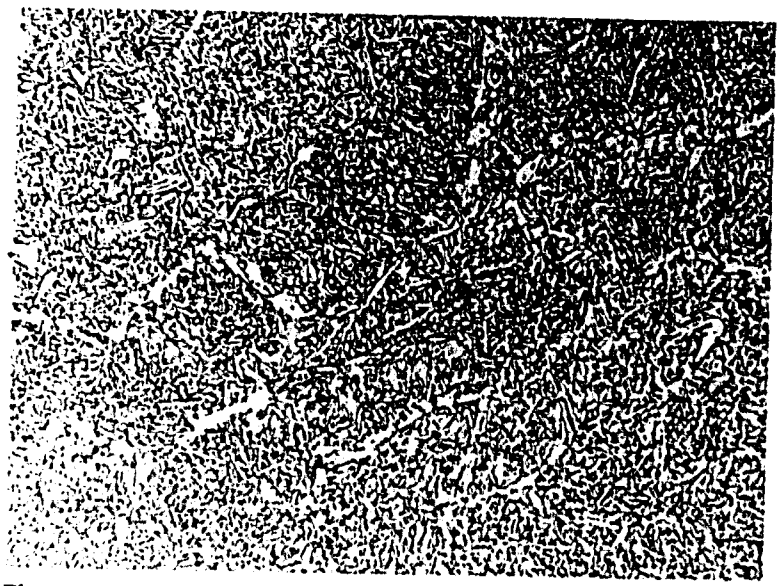

Figure 38 - Photomicrograph showing the weld metal microstructure of Core KA.
2% nital
Mag: 250X

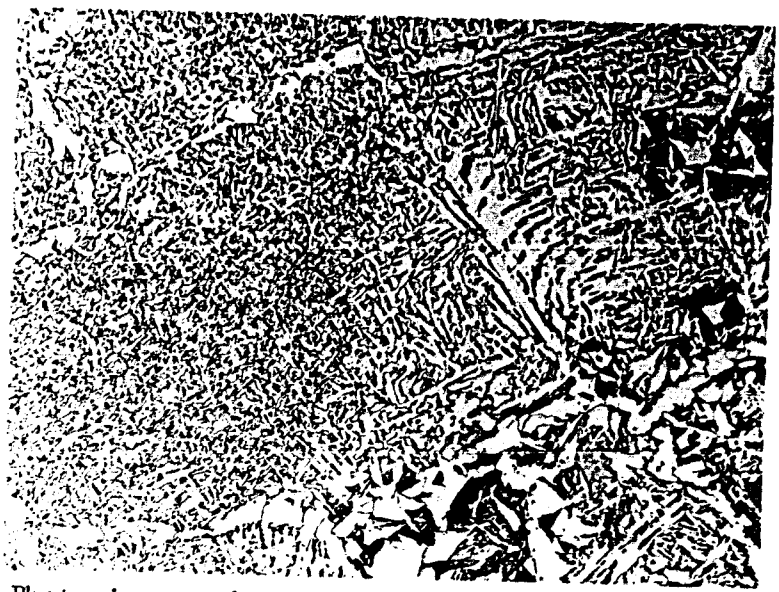

Figure 39 - Photomicrograph showing the fusion line microstructure of Core KA.
2% nital
Mag: 250X

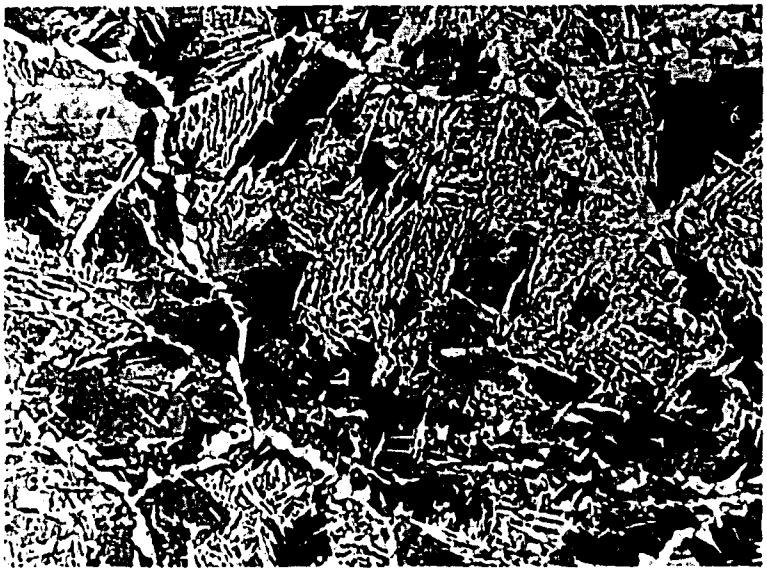

Figure 40 - Photomicrograph showing the coarse grain heat affected zone of Core KA in an area close to the fusion line.
2% nital Mag: 250X

Figure 41 - Photomicrograph showing the coarse grain heat affected zone of Core KA in an area 2-3 mm from the fusion line.
2% nital Mag: 250X

6300X

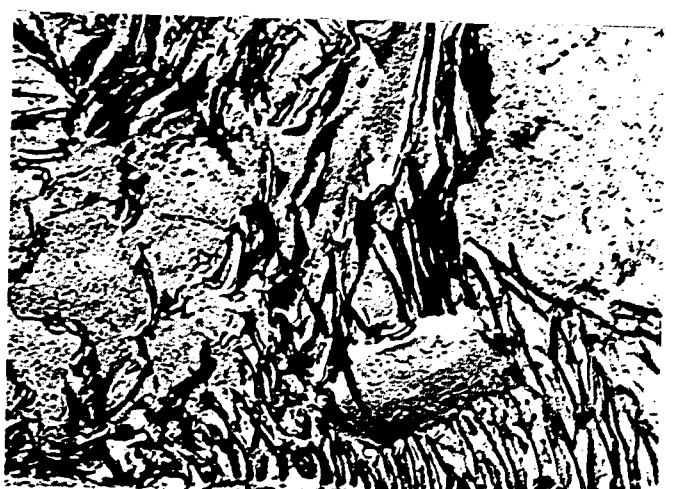

11,000X

Figures 42 & 43 - Transmission electron micrographs showing the ferrite/pearlite morphology in the coarse grained heat affected zone. These are both from chromium shadowed carbon/acetate replicas.

Figures 42 & 43 - Transmission electron micrographs showing the ferrite/pearlite morphology in the coarse grained heat affected zone. These are both from chromium shadowed carbon/acetate replicas.

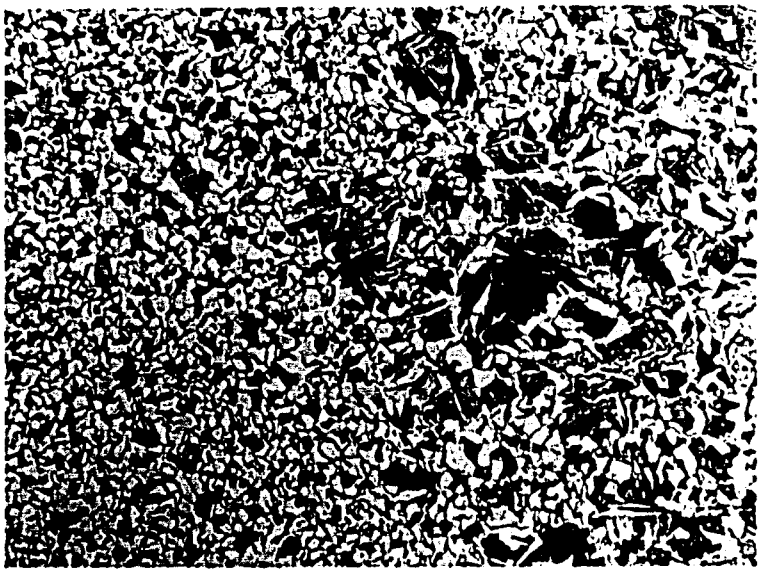

Figure 44 - Photomicrograph showing the coarse grain heat affected zone recrystallized grain heat affected zone boundary.
2% nital Mag: 250X

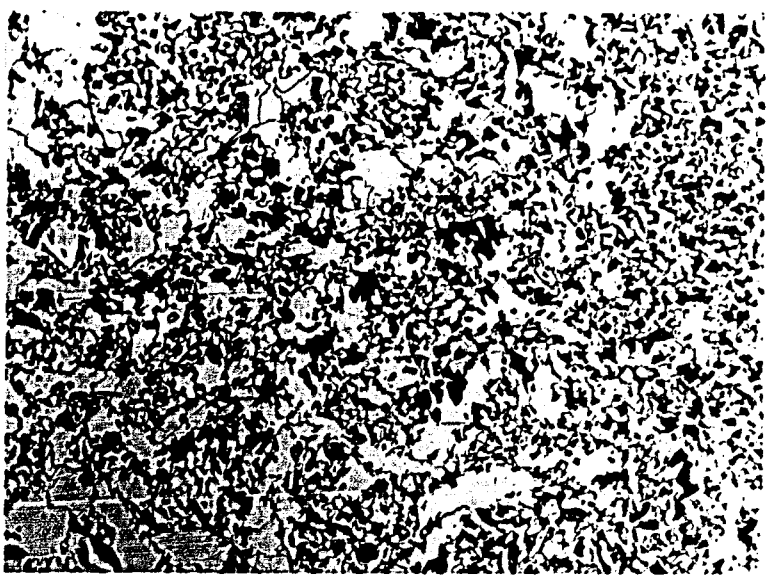

Figure 45 - Photomicrograph showing the recrystallized grain heat affected zone/intercritical heat affected zone boundary. Note the change in ferrite grain size.
2% nital Mag: 250X

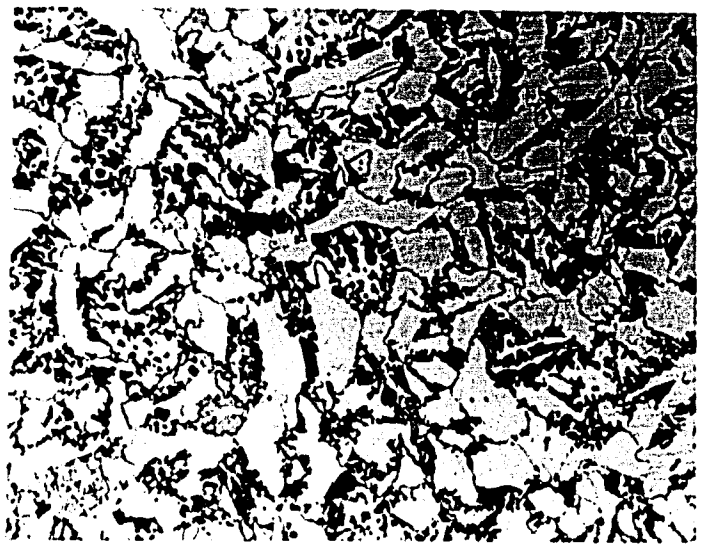

Figure 46 - Photomicrograph showing the intercritical heat affected zone. Note the refined pearlite colonies. 2% nital Mag: 250X

Figure 47 - Photomicrograph showing the intercritical heat affected zone/unaffected base metal boundary. 2% nital Mag: 250X

Figure 48 - Photomicrograph showing the ferrite pearlite structure of the unaffected base metal.
2% nital Mag: 250X

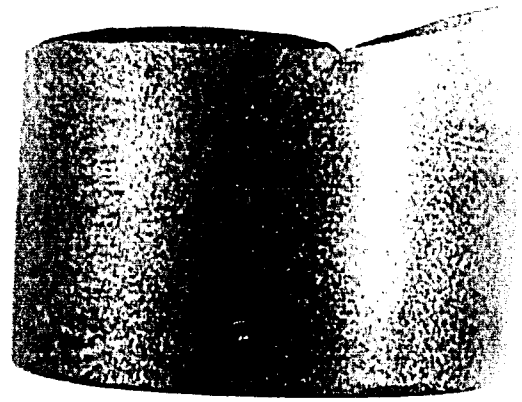

Figure 49 - Photomacrograph showing Core KK after rough polishing and macroetching.
5% nital
Mag: 1.5 X

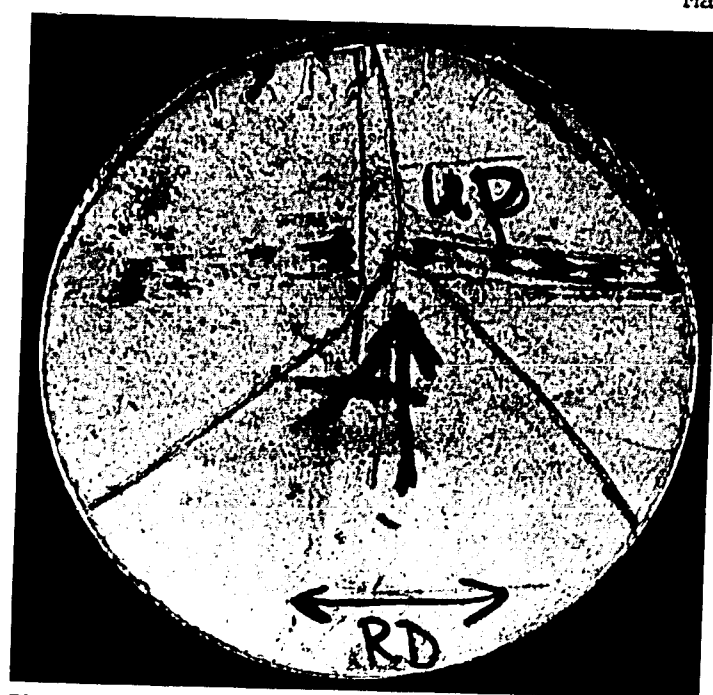

Figure 50 - Photomacrograph showing the north face of Core KK.
Mag: 1.8X

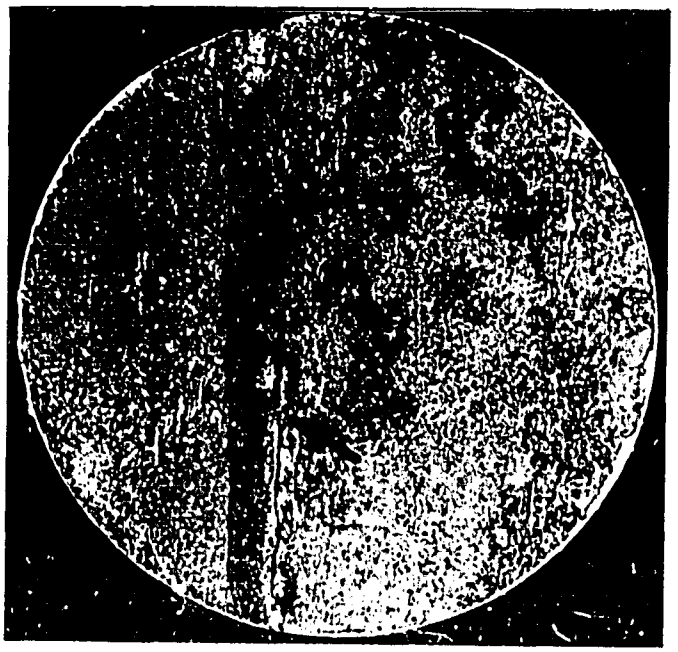

Figure 51 - Photomacrograph of the south face of Core KK. Note the entrapped slag (see arrows). Mag: 1.8X

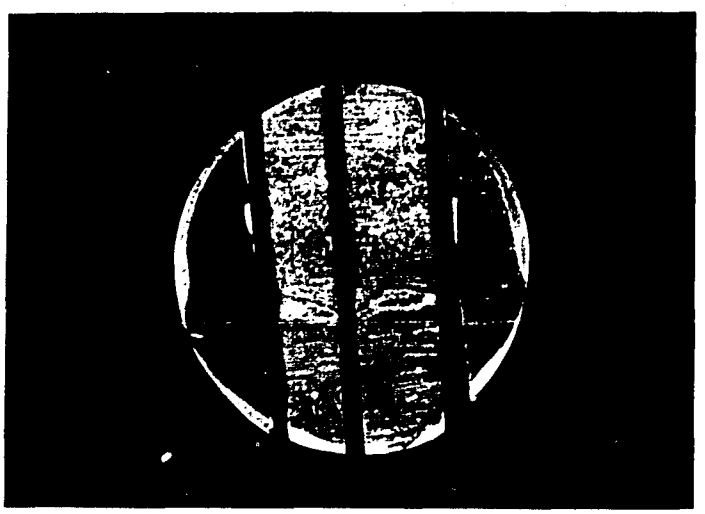

Figure 52 - Photomacrograph showing Core KK after sectioning.

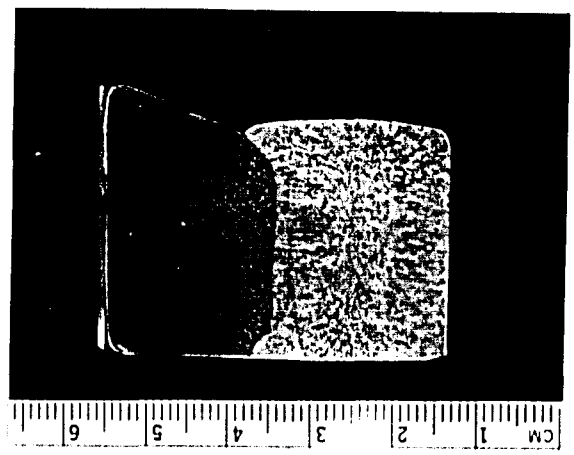

Figure 53 - Photomacrograph of surface "A" shown in Fig. 52 after polishing and macro-etching. 5% nital

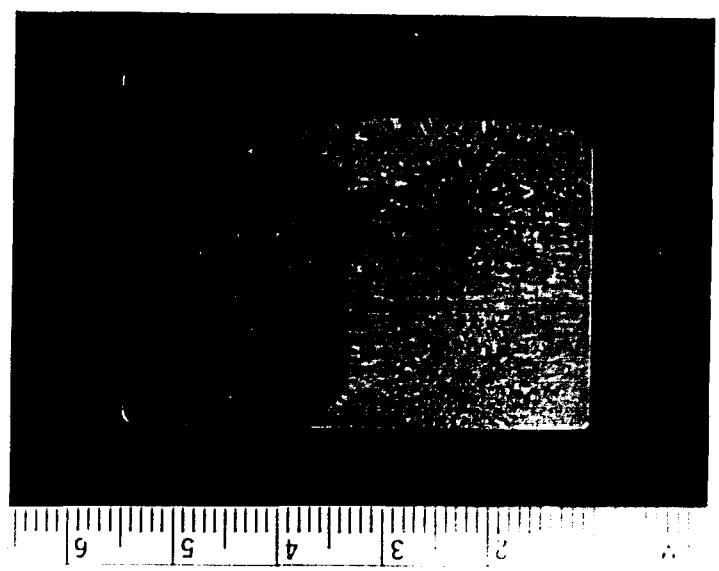

Figure 54 - Photomacrograph of surface "B" shown in Fig. 52 after polishing and macro-etching. 5% nital

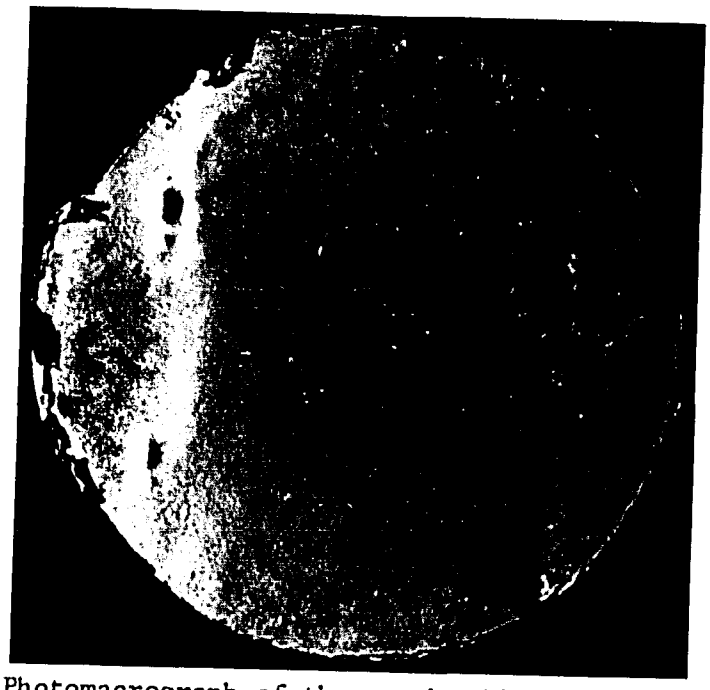

Figure 55 - Photomacrograph of the north side of Core KL.
Mag: 1.8X

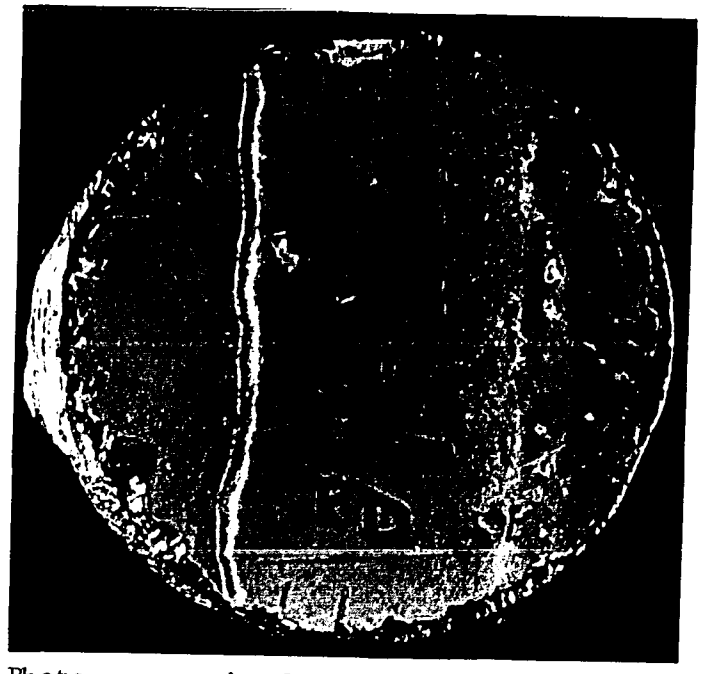

Figure 56 - Photomacrograph of the south side of Core KL.
Mag: 1.8X

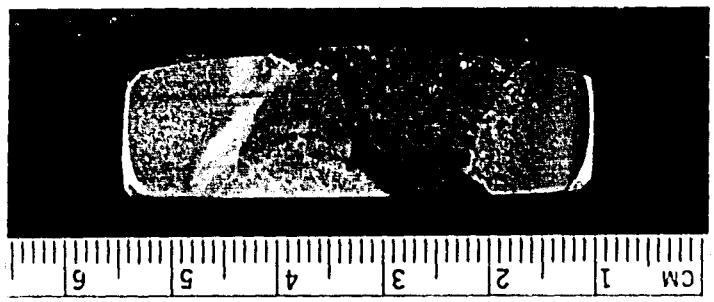

Figure 57 - Photomacrograph showing a polished and etched cross-section of Core KL. Note the EG weldment, the repair weld and the entrapped slag between these weldments.

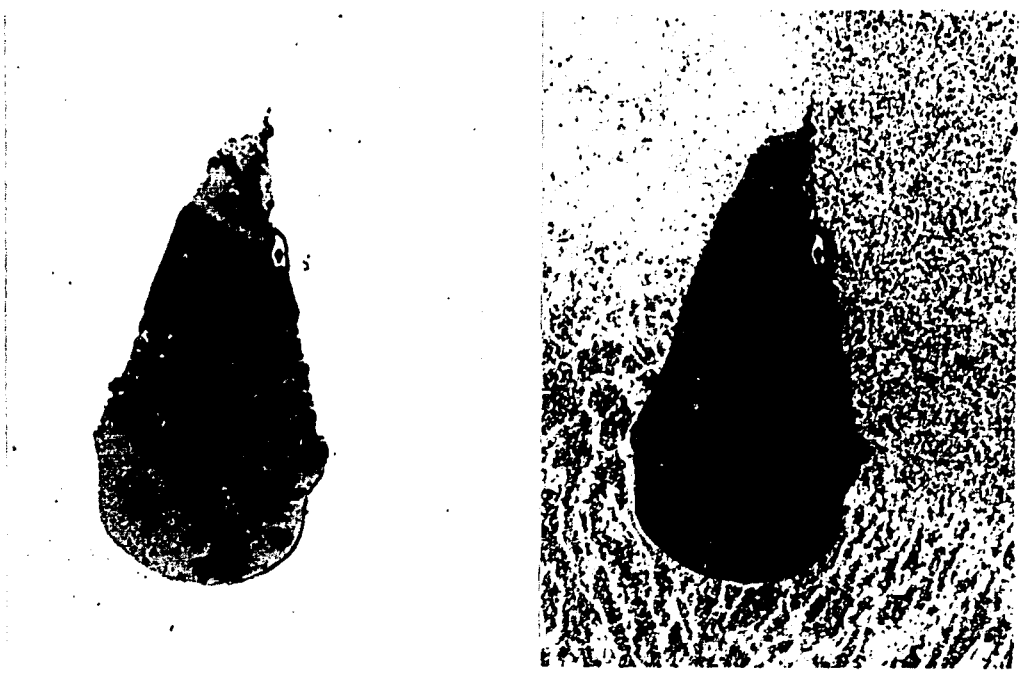

unetched Mag: 50X 2% nital Mag: 50X

Figures 58-59 - Photomicrographs showing an unetched and an etched view of the entrapped slag seen in Core KL (see Fig. 57).

Figure 60 - Enlarged view of the tip of the entrapped slag shown in Figs. 57-59. Note the sharp radius of the defect in this area.
2% nital Mag: 250X

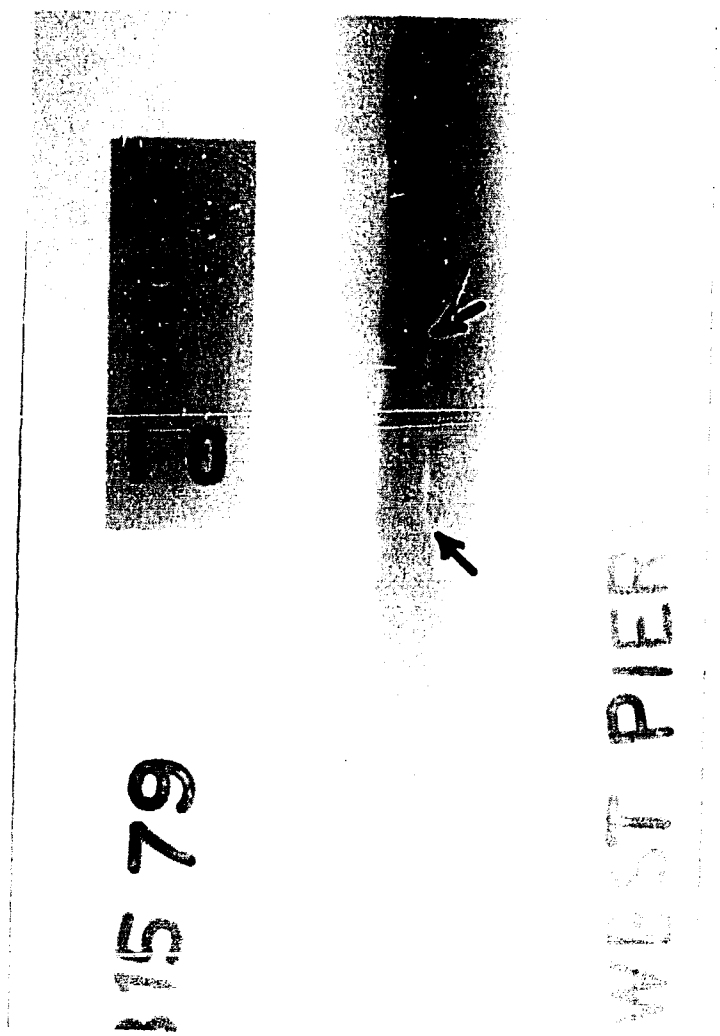

Figure 61 - This shows a portion of the radiograph taken prior to removal of Core KL. The arrow shows the defect which was removed.

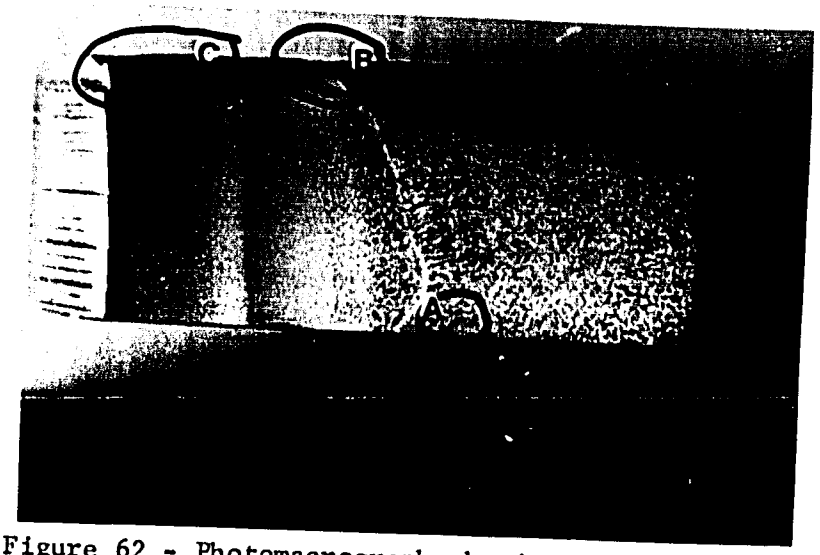

Figure 62 - Photomacrograph showing a polished and macroetched view of the flange edge in Core KJ.

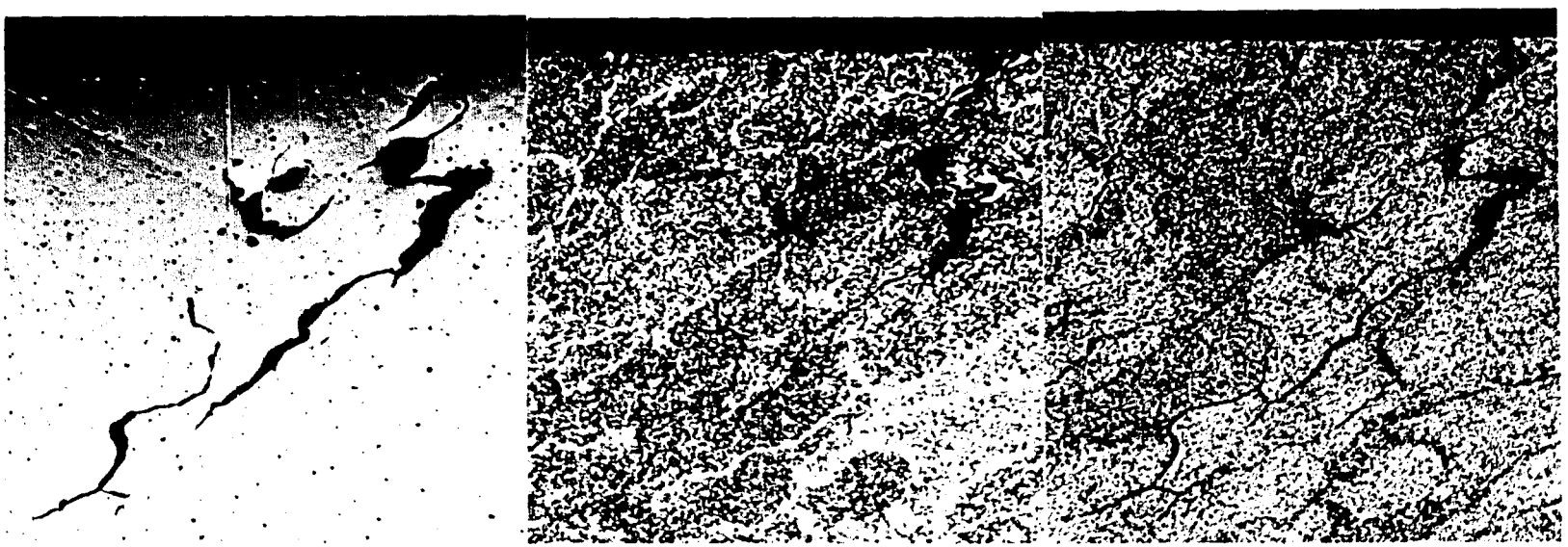

Figures 63-65 - Photomicrographs of a defect in area "A" in Fig. 62.

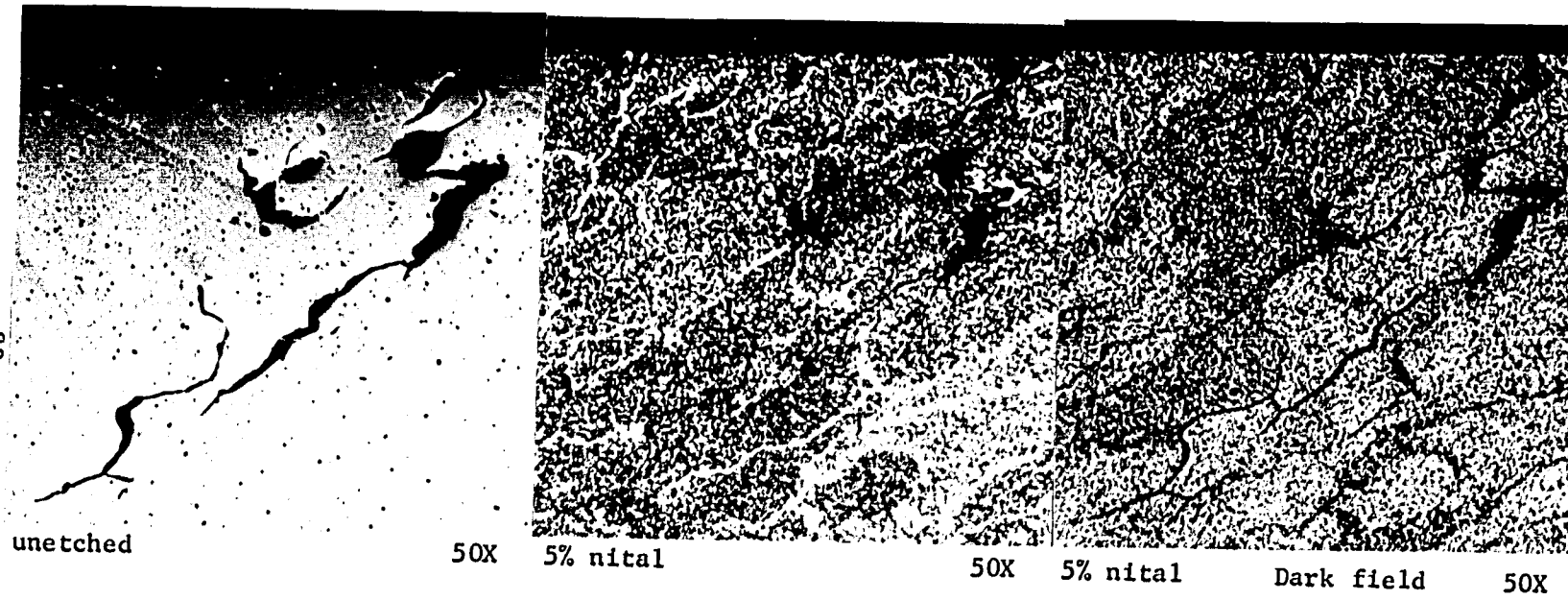

Figures 63-65 - Photomicrographs of a defect in area "A" in Fig. 62.

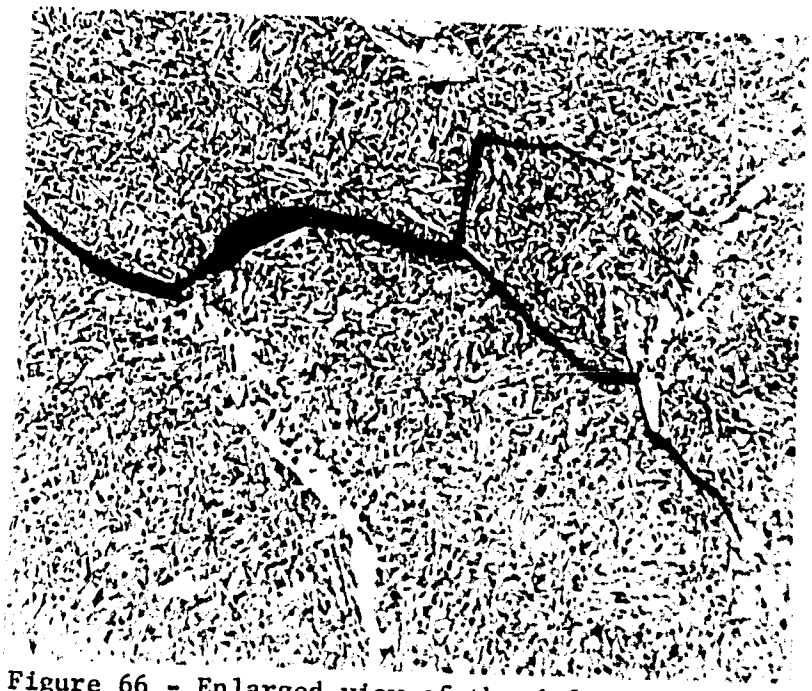

Figure 66 - Enlarged view of the defect shown in Figs. 63-65.
2% nital
Mag: 250X

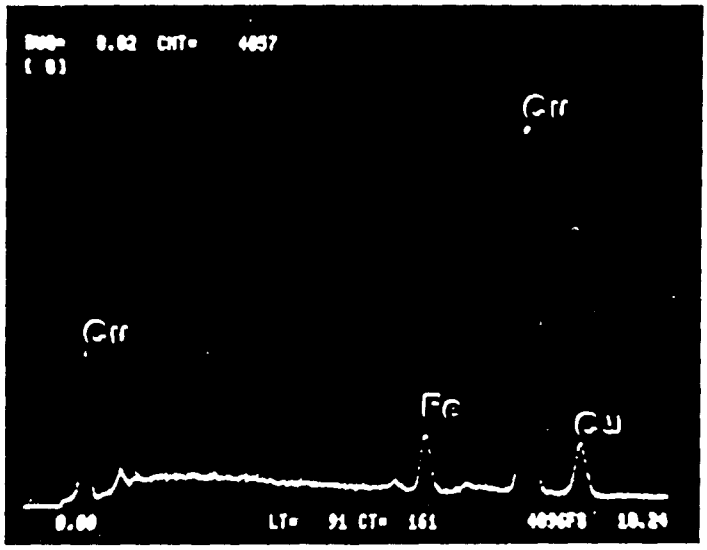

A

B

Figure 67A & B - Scanning electron micrograph showing a section of the defect seen in Figs. 63-66. An EDAX printout from the encircled region documents the presence of copper, aluminum, silicon, manganese and iron in this area.

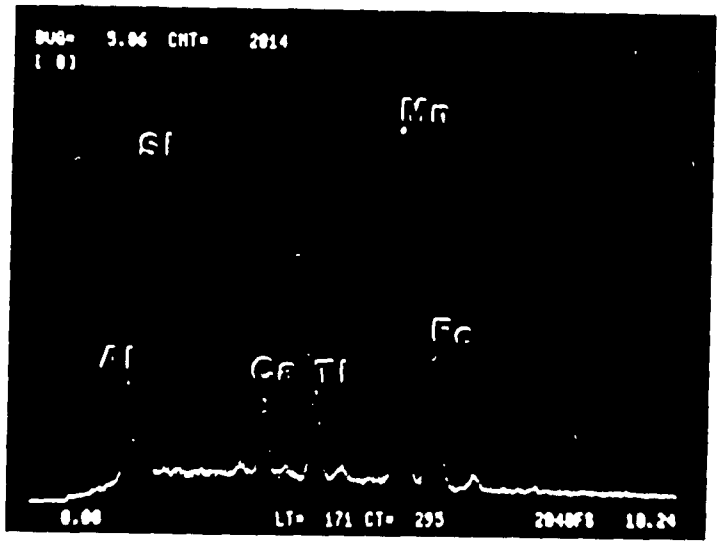

A

B

Figure 68A & B - Another view of the defect found in Core KJ. The embedded material found in this region showed high silicon, calcium, titanium and manganese concentrations.

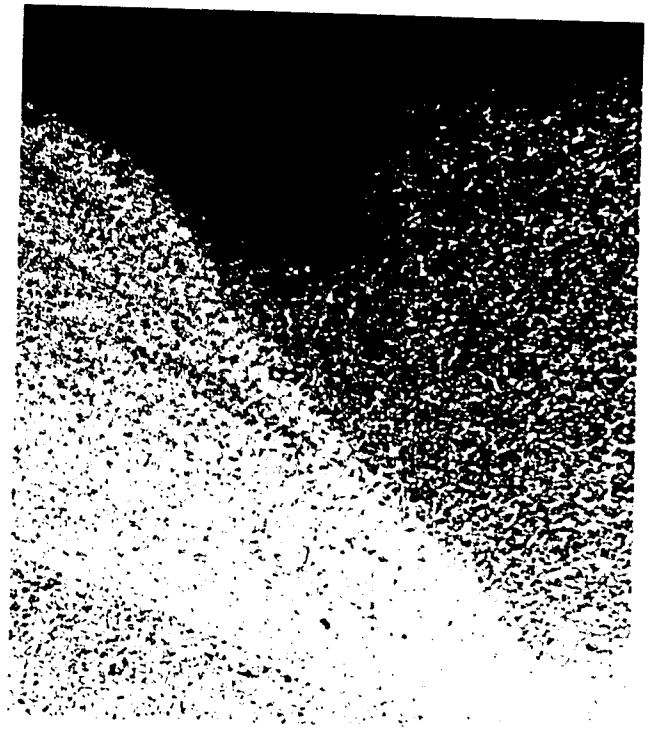

Figure 69 - Photomicrograph showing the defect in region "B" on Fig. 62. Note the sharp corner of this defect which lies fully in the weld metal. This defect is believed to be a machining mark which occurred during the trepanning operation of Core KJ.
2% nital

Mag: 50X

Figure 70 - Scanning electron micrograph showing the tip of the defect shown in Fig. 69. The fine cracks shown are believed to be cracks in the surface oxide layer seen in this area.

Mag: 500X/SEM

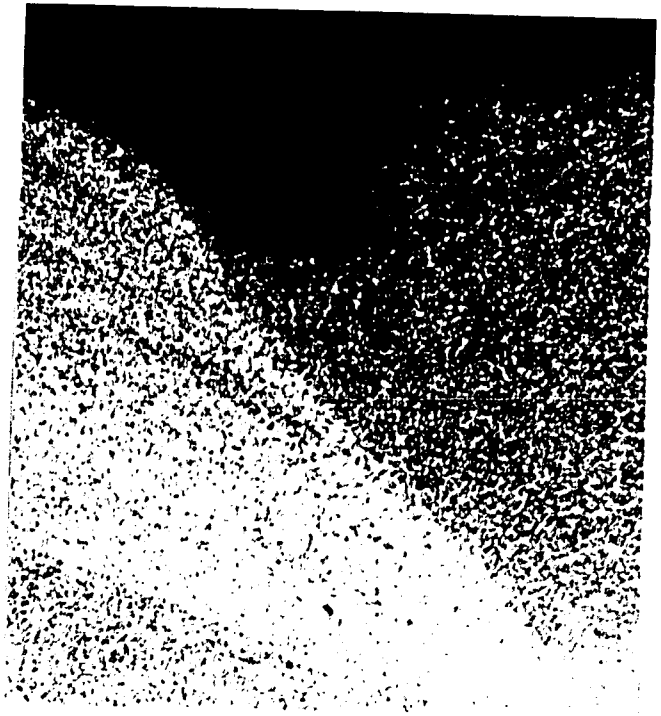

Figure 69 - Photomicrograph showing the defect in region "B" on Fig. 62. Note the sharp corner of this defect which lies fully in the weld metal. This defect is believed to be a machining mark which occurred during the trepanning operation of Core KJ.
2% nital

Mag: 50X

Figure 70 - Scanning electron micrograph showing the tip of the defect shown in Fig. 69. The fine cracks shown are believed to be cracks in the surface oxide layer seen in this area.

Mag: 500X/SEM

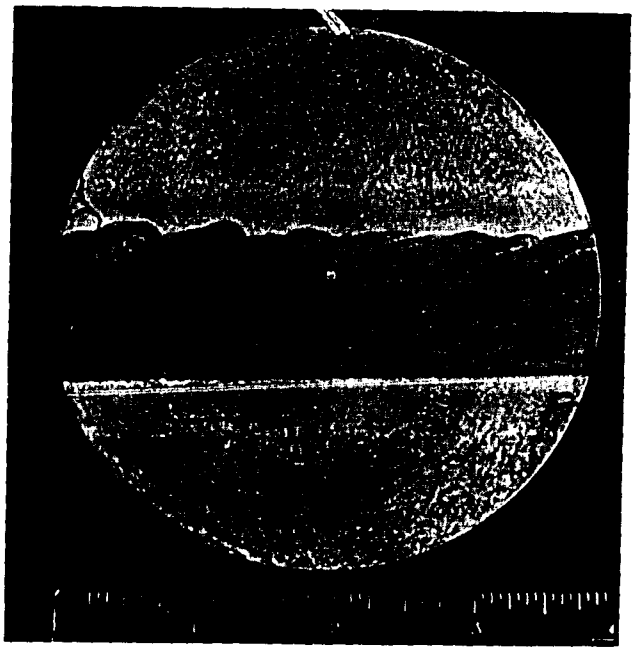

Figure 71 - Photomacrograph showing a diametrical view of Core KC after rough polishing and macro-etching. The ruler is in inches.
5% nital Mag: 0.75X

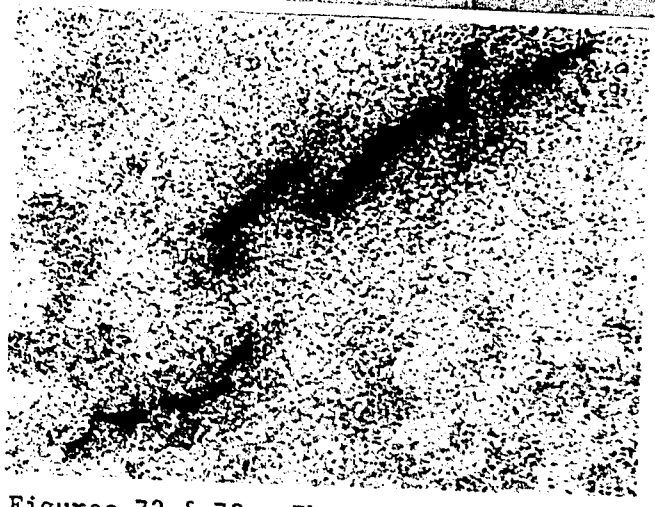

Figures 72 & 73 - Photomicrographs showing the defect found in the encircled area shown in Fig. 71.
unetched/2% nital

Mag: 50X

Figure 74 - Same as Figs. 72 & 73 except in the macroetched condition used for SEM observation.
5% nital

Mag: 50X

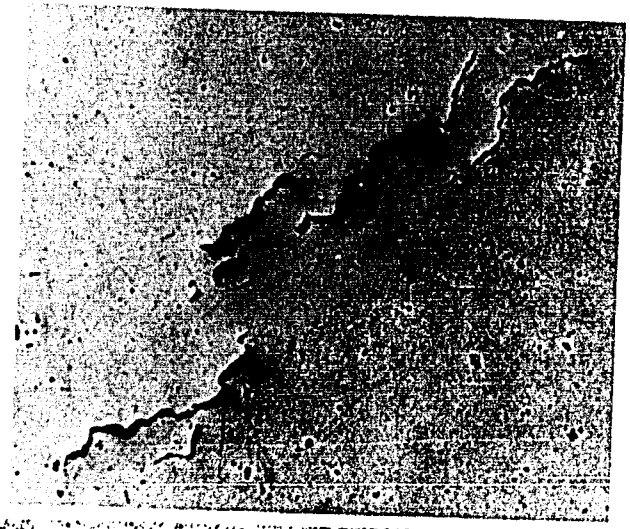

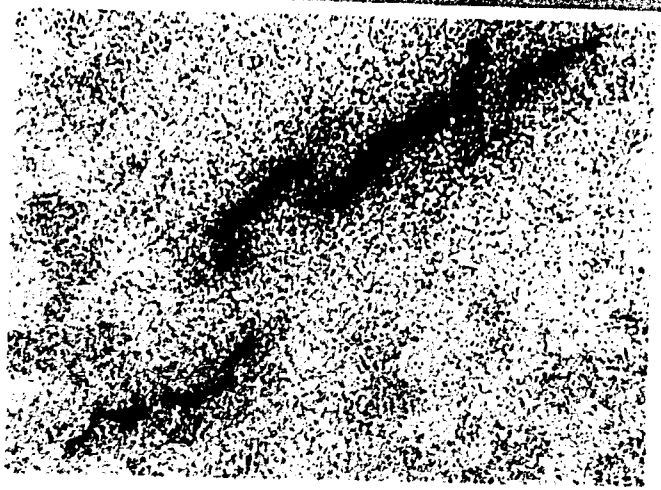

Figures 72 & 73 - Photomicrographs showing the defect found in the encircled area shown in Fig. 71.
unetched/2% nital

Mag: 50X

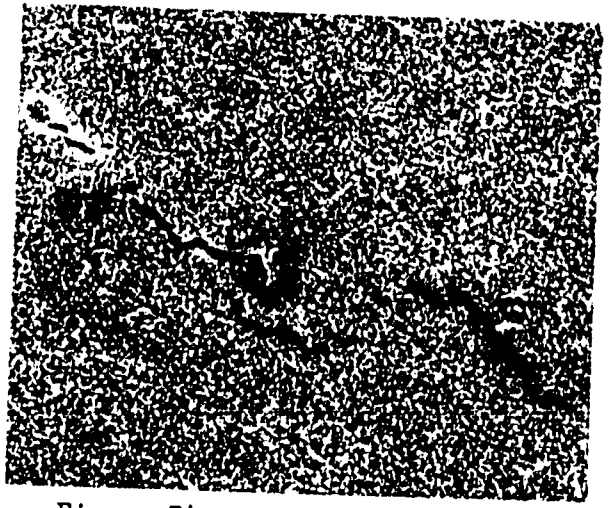

Figure 74 - Same as Figs. 72 & 73 except in the macroetched condition used for SEM observation.
5% nital

Mag: 50X

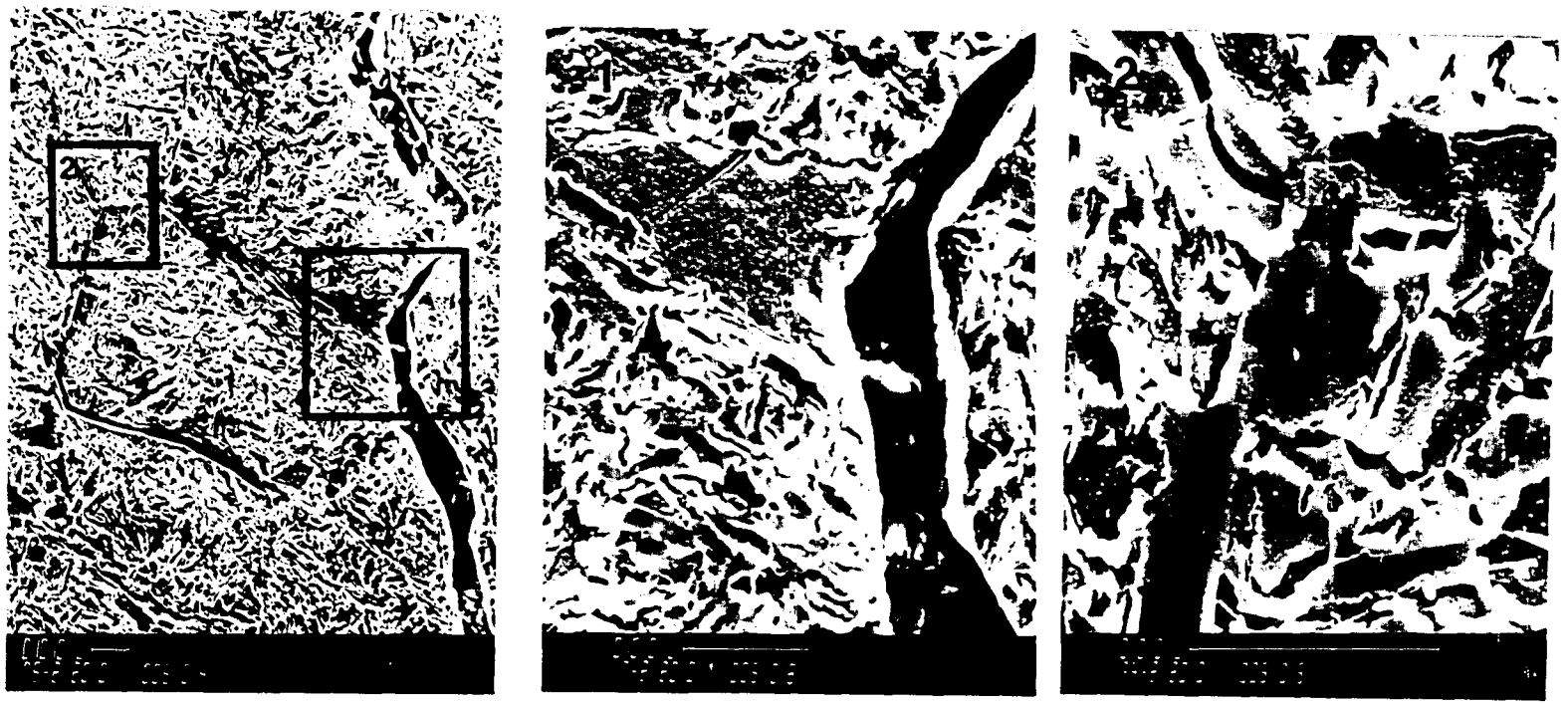

5% nital Mag: 500X 5% nital Mag: 1700X 5% nital Mag: 3400X

Figures 75-77 - Scanning electron micrographs of the defect found in Core KC (see Figs. 71-74). Note the intergranular character of these cracks. These cracks appear to be located along the interface of proeutectoid ferrite which nucleates along prior austenite grain boundaries.

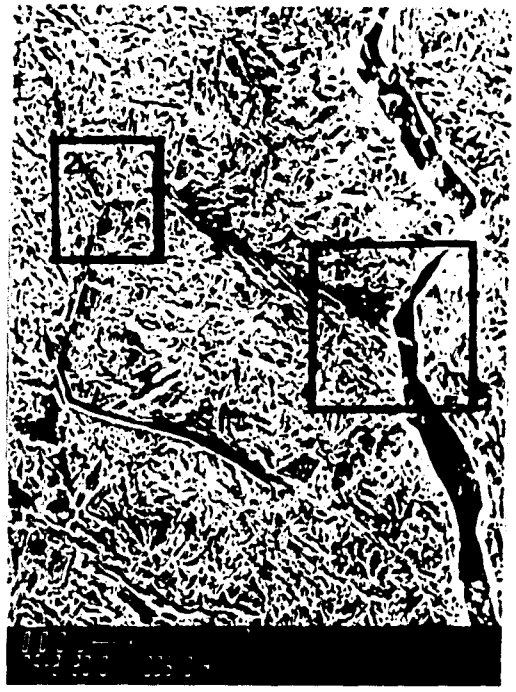

5% nital Mag: 500X

5% nital Mag: 1700X

5% nital Mag: 3400X

Figures 75-77 - Scanning electron micrographs of the defect found in Core KC (see Figs. 71-74). Note the intergranular character of these cracks. These cracks appear to be located along the interface of proeutectoid ferrite which nucleates along prior austenite grain boundaries.

Figure 78 - Rockwell B hardness traverse of a cross-section of core KJ using 2 mm increments.

Hardness Values

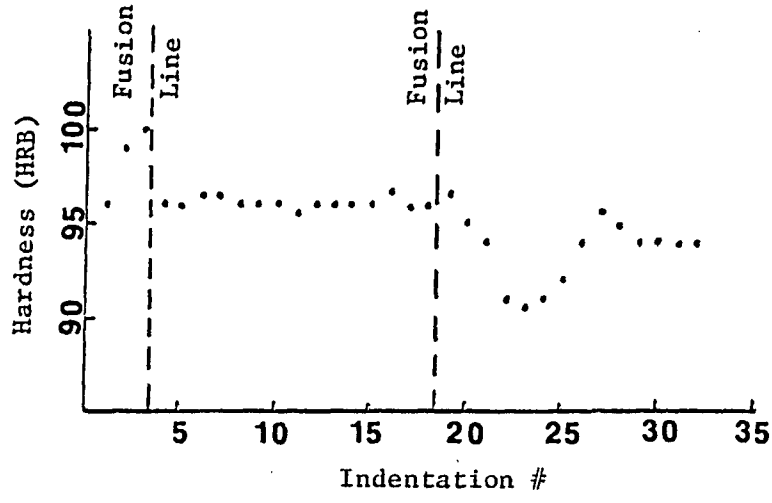

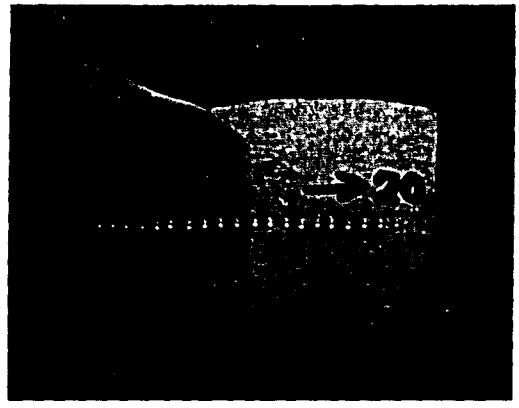

Figure 79 - Rockwell B hardness traverse of a cross-section of core KK using 2 mm increments.

Hardness Values

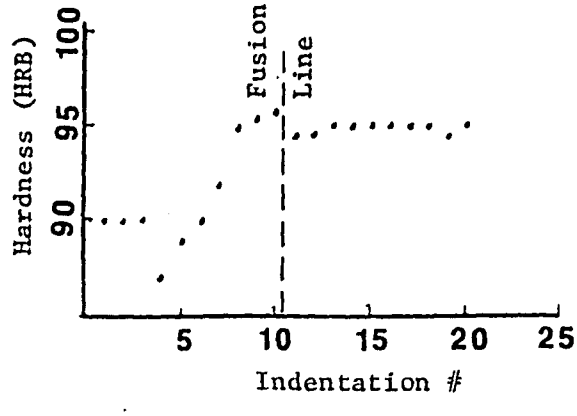

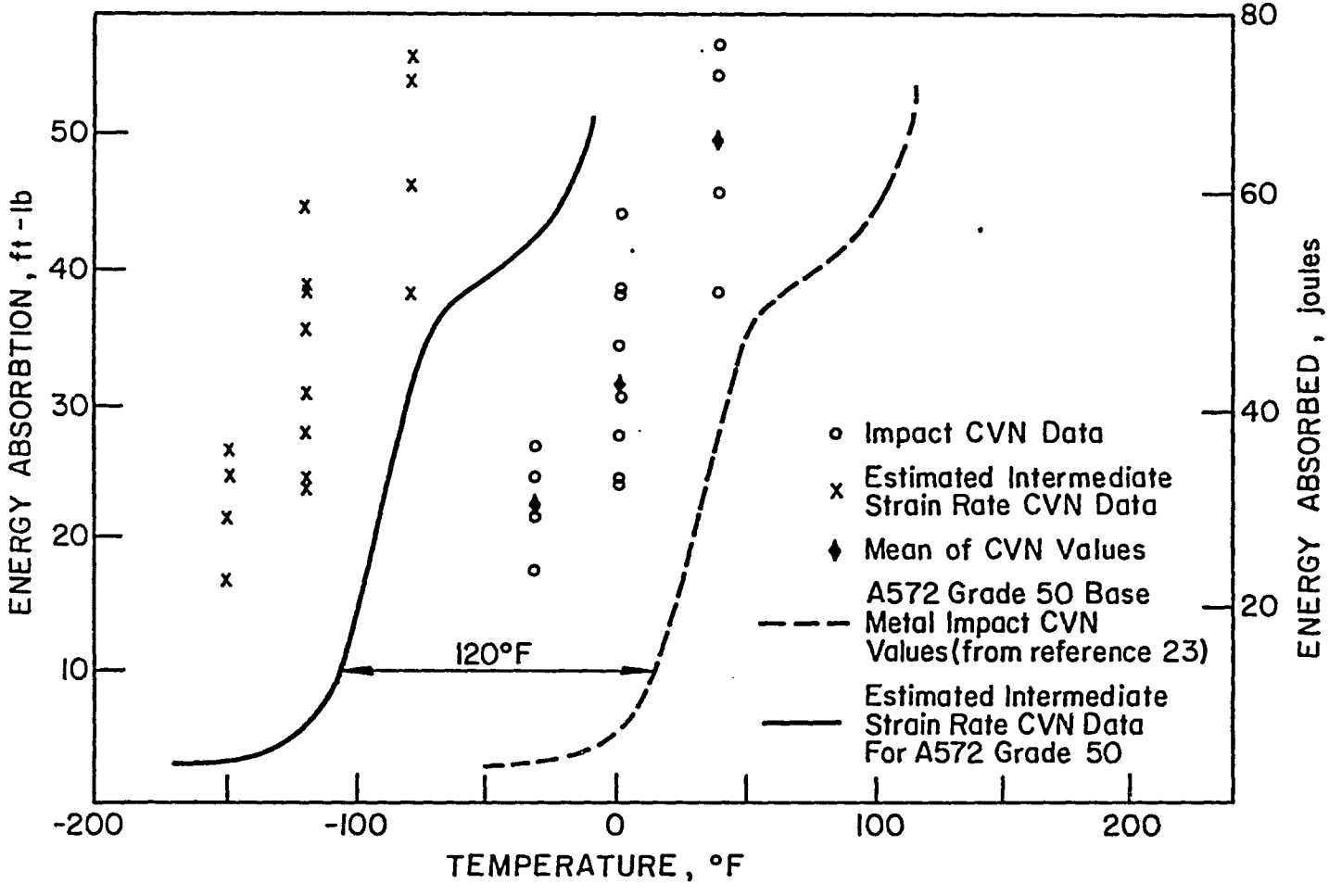

Figure 80A - Off centerline CVN values and empirically transformed intermediate loading rate values.

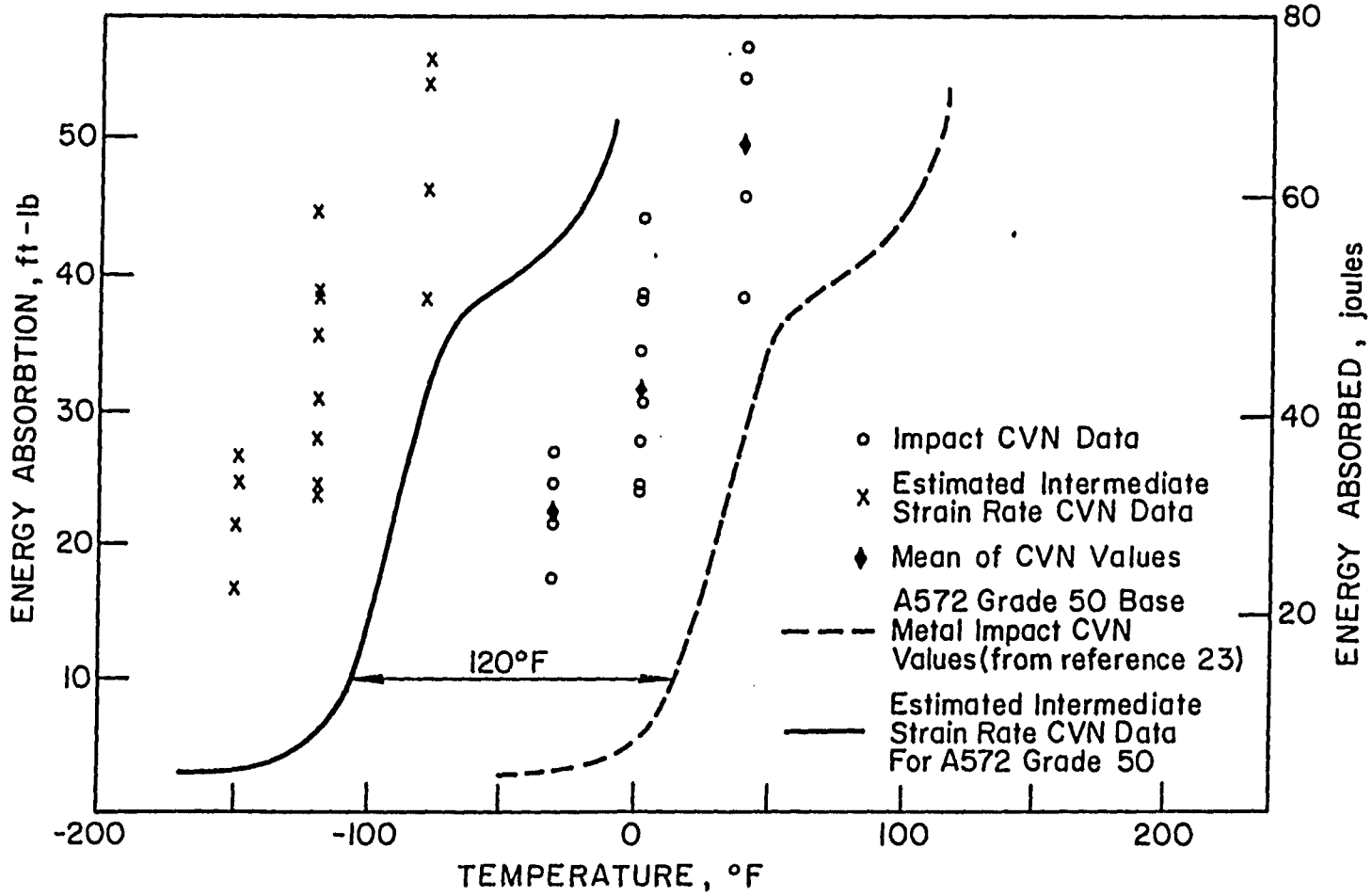

Figure 80A - Off centerline CVN values and empirically transformed intermediate loading rate values.

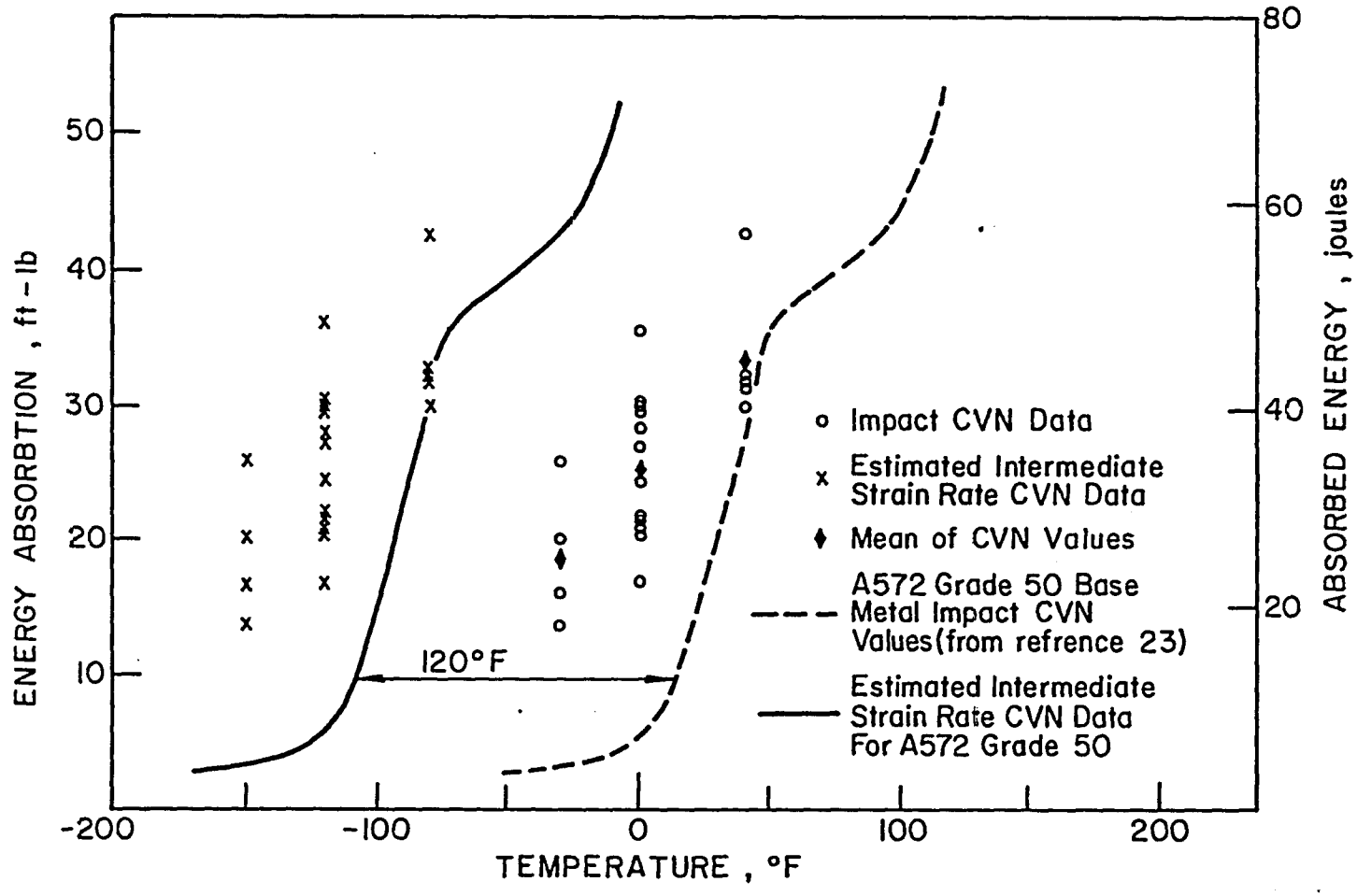

Figure 80B - Centerline CVN values and empirically transformed intermediate loading rate values.

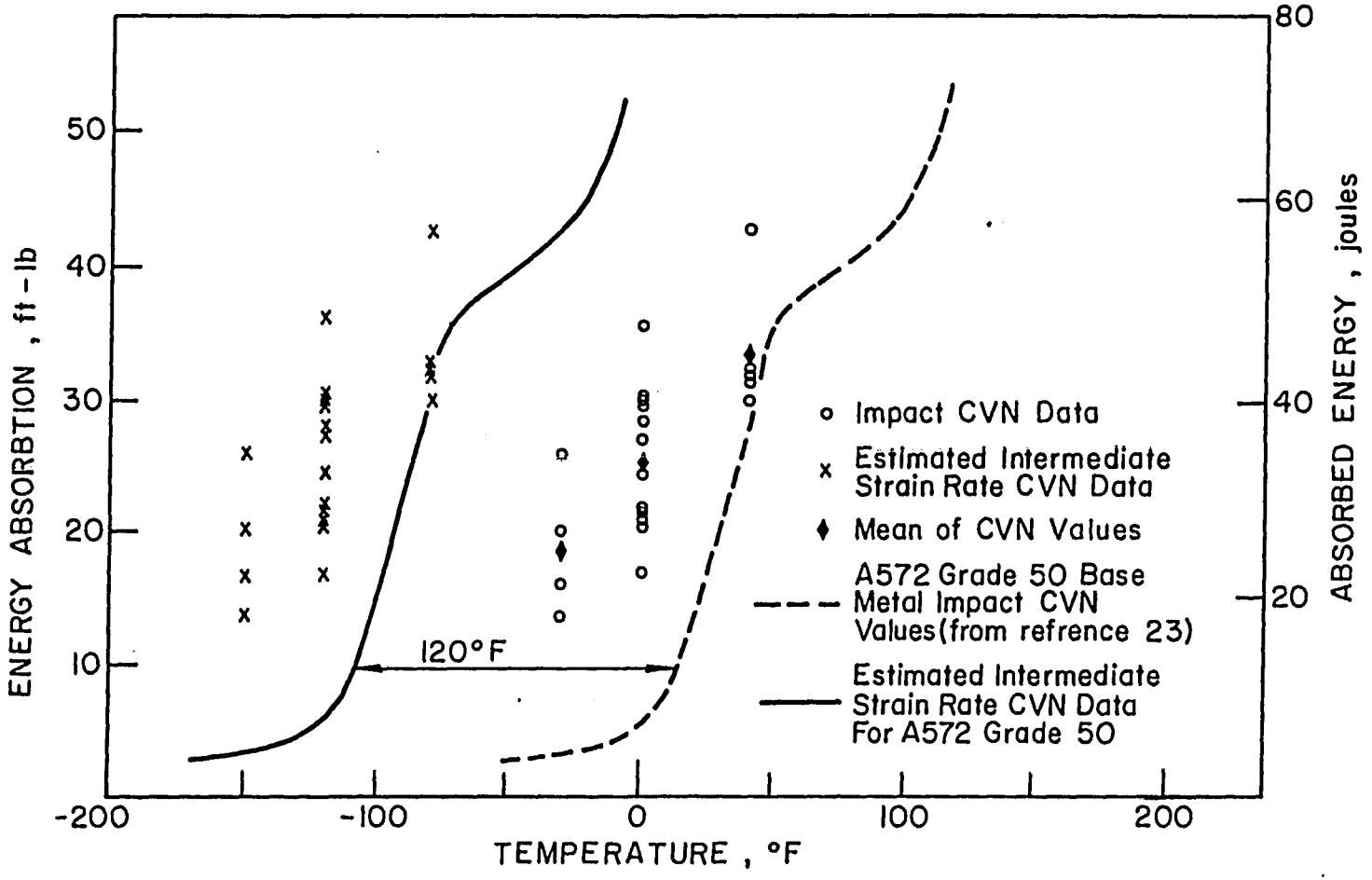

Figure 80B - Centerline CVN values and empirically transformed intermediate loading rate values.

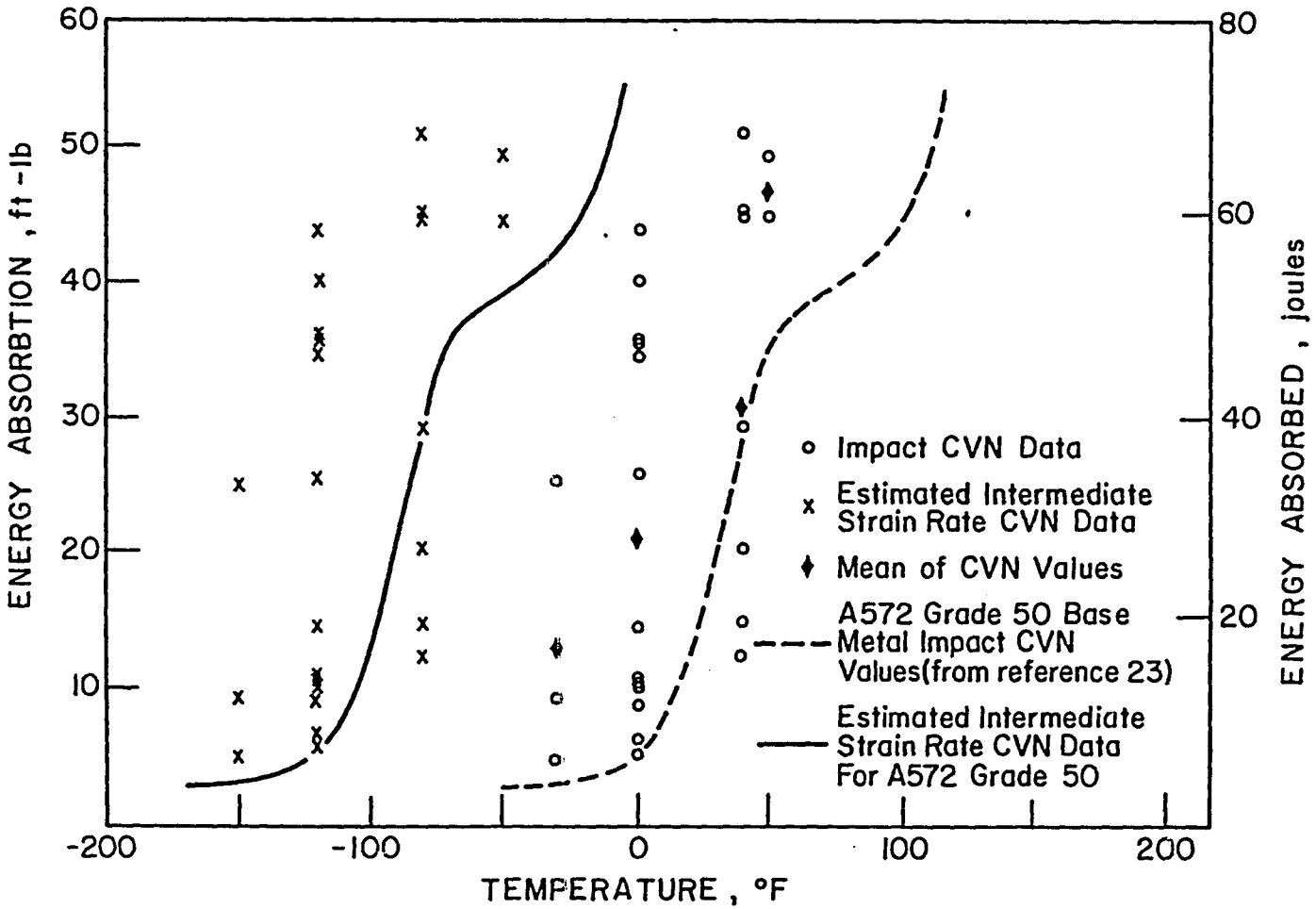

Figure 80C - Fusion line CVN values and empirically transformed intermediate loading rate values.

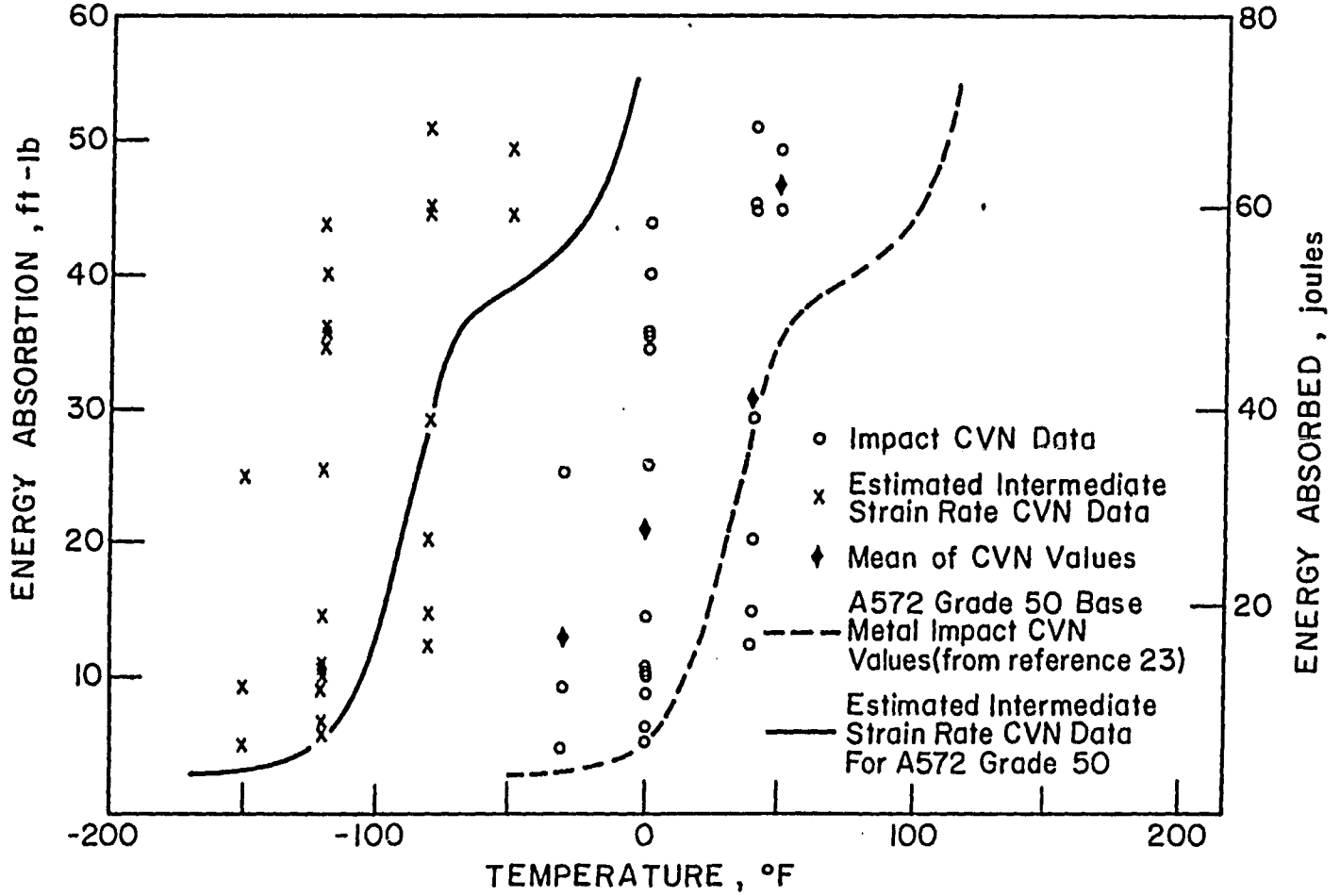

Figure 80C - Fusion line CVN values and empirically transformed intermediate loading rate values.

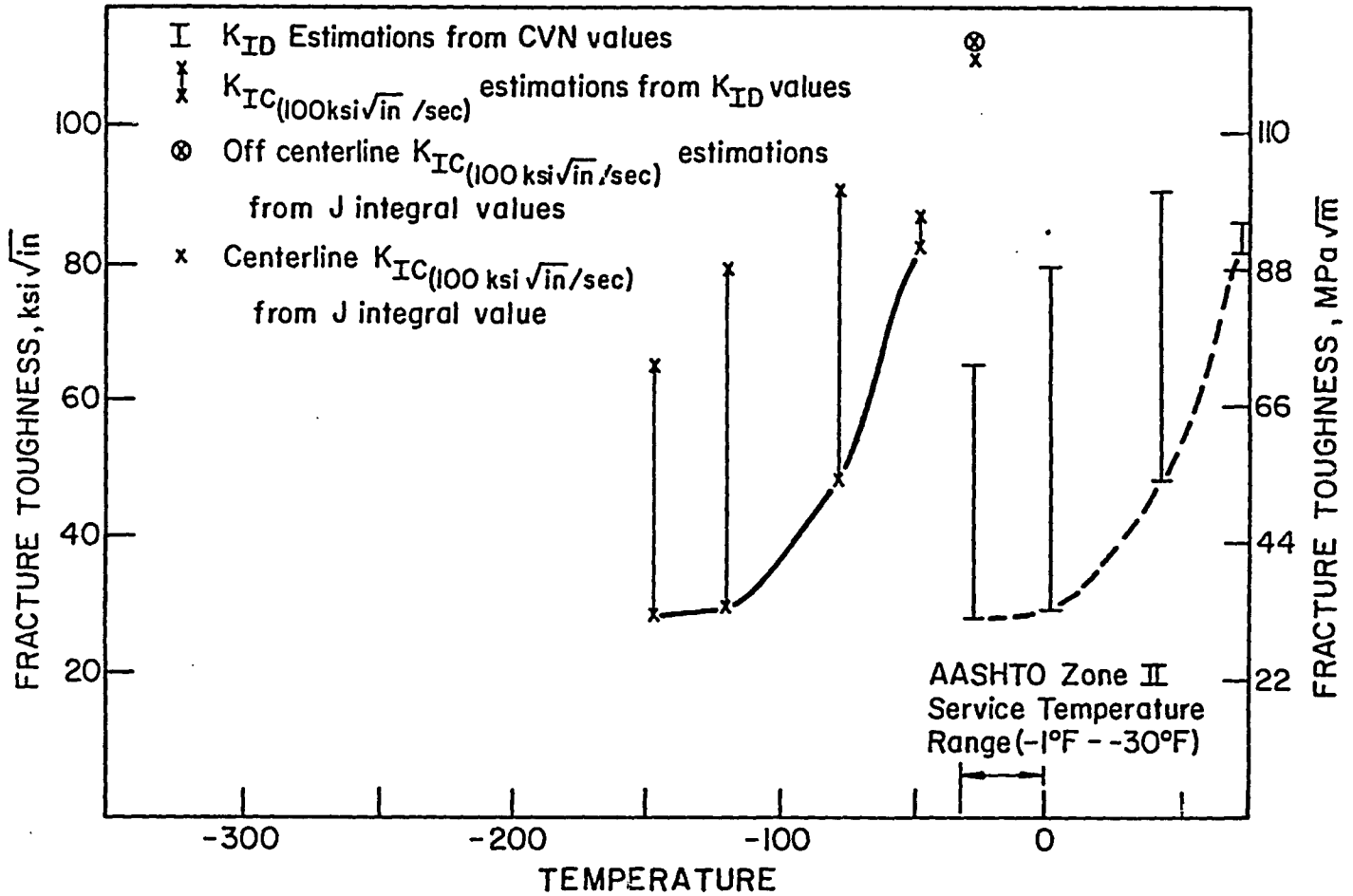

Figure 80D - Correlations between CVN estimated notched fracture toughness values and J integral estimated notched fracture toughness values of the Kittanning Bridge electrogas weld metal. The upper and lower bound CVN correlations were estimated from the highest and lowest dynamic CVN values observed in all three weld zones.

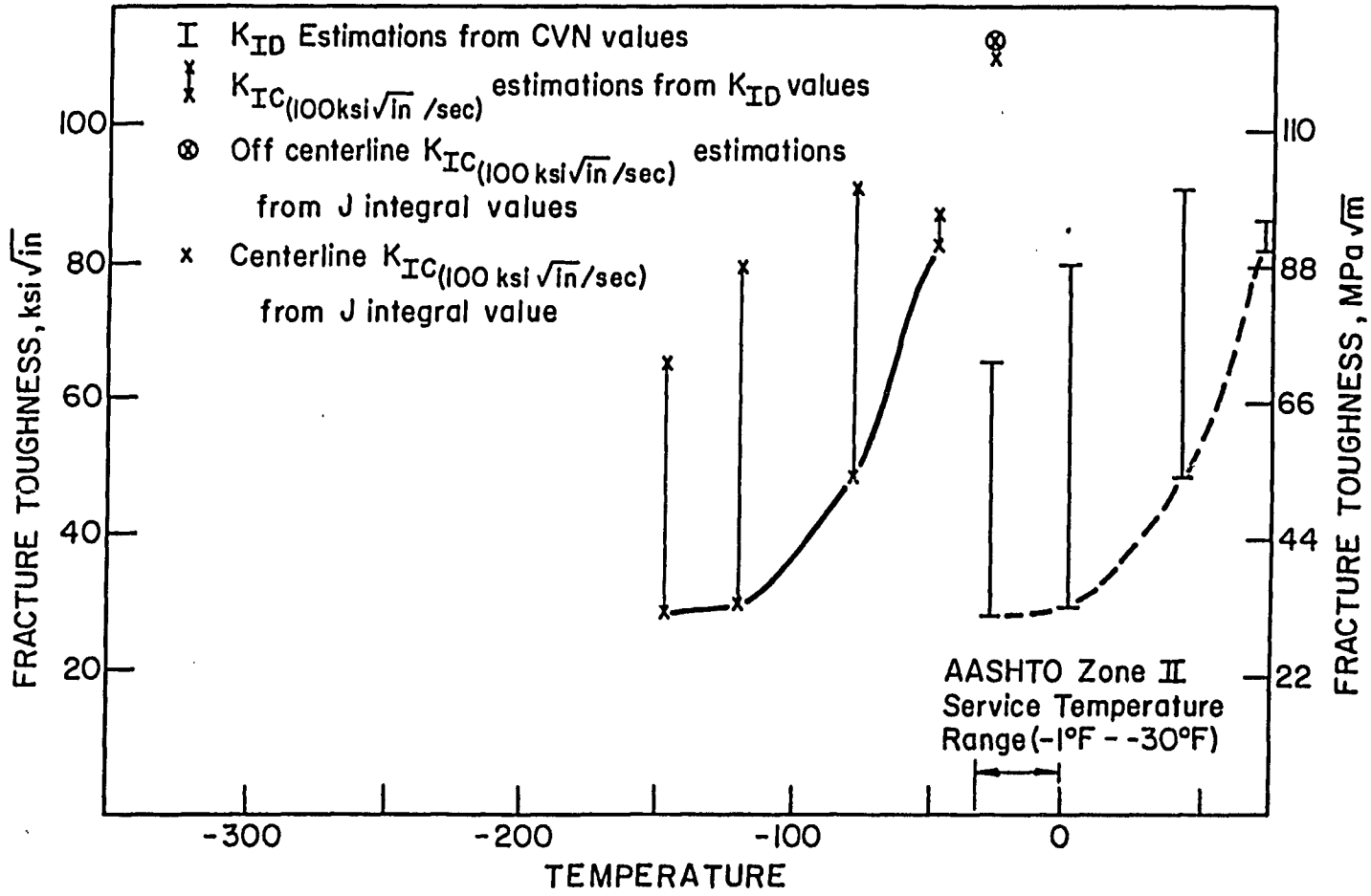

Figure 80D - Correlations between CVN estimated notched fracture toughness values and J integral estimated notched fracture toughness values of the Kittanning Bridge electrogas weld metal. The upper and lower bound CVN correlations were estimated from the highest and lowest dynamic CVN values observed in all three weld zones.

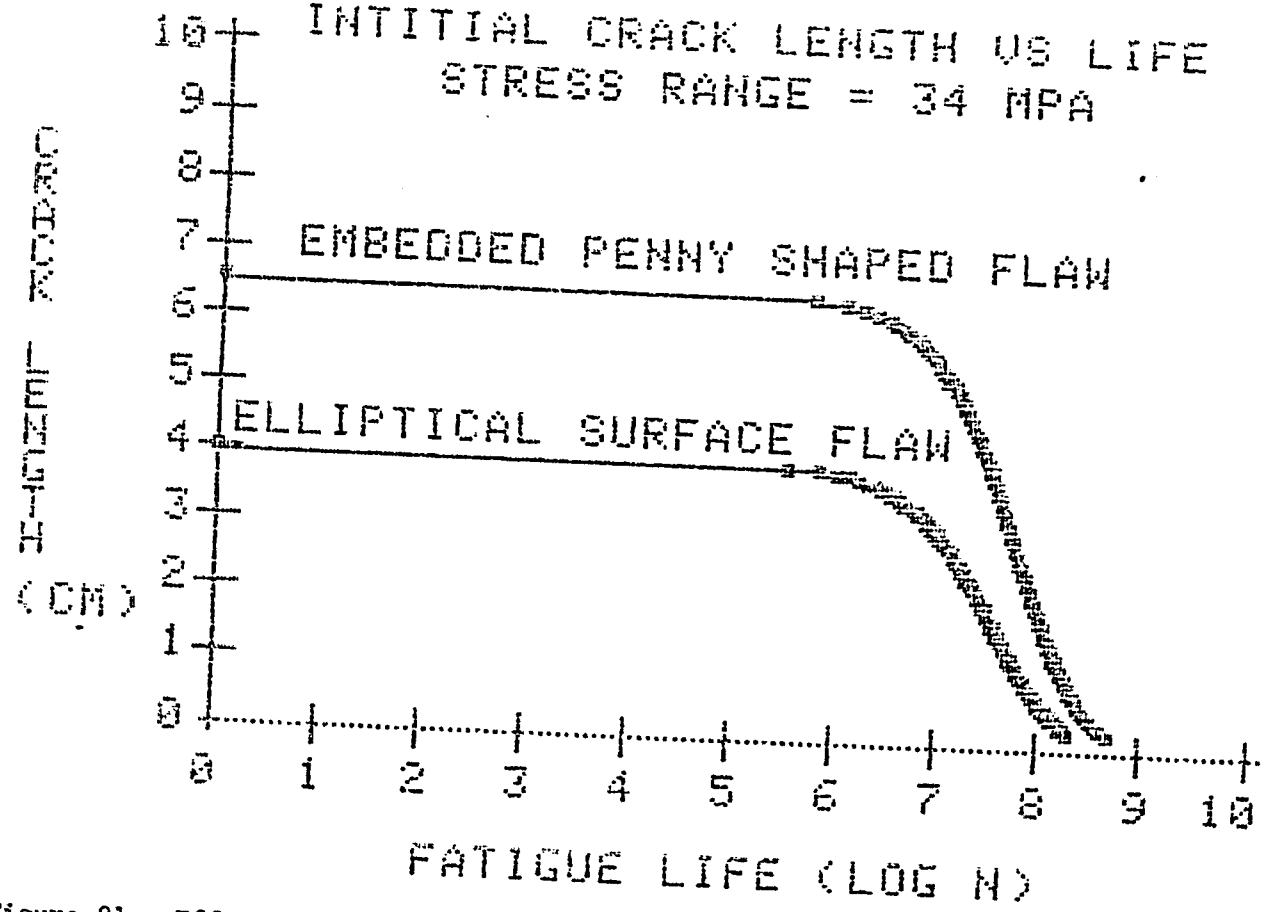

Figure 81 - Effect of crack geometry and size on the estimated fatigue life of the Kittanning Bridge electrogas weldments.

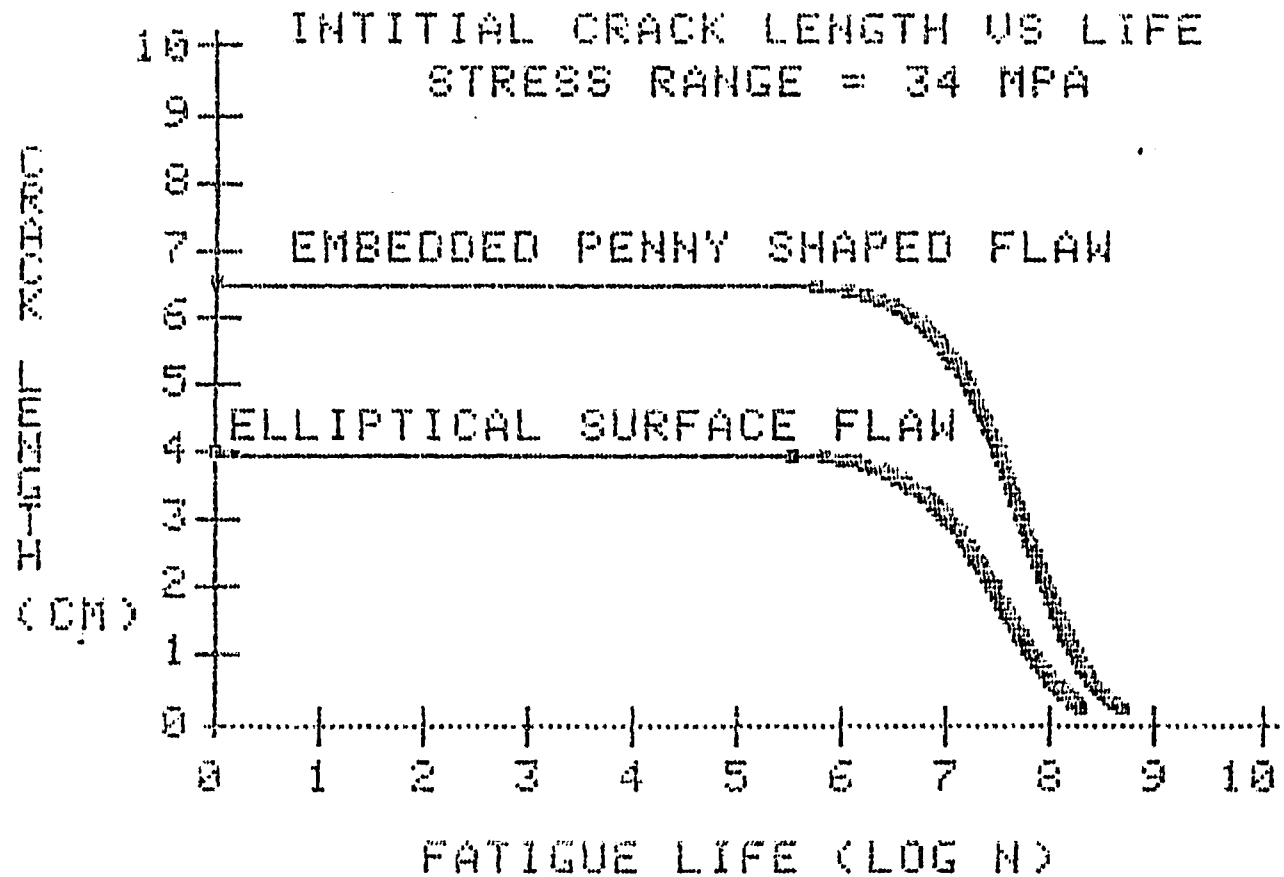

Figure 81 - Effect of crack geometry and size on the estimated fatigue life of the Kittanning Bridge electrogas weldments.

REFERENCES

1. Cambell, H. C., "Electroslag, Electrogas and Related Welding Processes," WRC Bulletin No. 154, pp. 21-22, Sept. 1970.
2. Paton, B. E., "Electroslag Welding," American Welding Society, 2nd Edition, New York, 1962.
3. Paton, B. E., "Electroslag Welding of Very Thick Materials," Welding Journal, Vol. 41, pp. 115-122, Dec. 1962.
4. Woodley, C. C., Burkekin, F. M. and Wells, A. A., "Electroslag Welded Wide Plate Tests on 3" Thick Mild Steel," British Welding Journal, Vol. 45, pp. 165-193, March 1966.
5. Culp, J. D., "Electroslag Weldments--Performance and Needed Research," Welding Journal, Vol. 59, pp. 27-42, July 1979.
6. Fisher, J. W., Pense, A. W., Wood, J. D. and Somers, B. R., "An Evaluation of Electroslag Welds in Three Bridges," Fritz Engineering Laboratory Report No. 438-1(81), March 1981.
7. Benter, Jr., W. P. and Schilling, C. G., "Acceptance Criteria for Electroslag Weldments in Bridges," National Cooperative Highway Research Program Report 201, Transportation Research Board-National Research Council, Washington, DC May 1979.
8. Shackleton, D. N., "Research Developments in Electroslag and Electrogas Welding," Revue de La Soudure (Brussels), Vol. 31, No. 1, pp. 1-21, 1975--Comptendex 1975 963608.
9. Loosen, B., "Electrogas Welding--applications and progress," Welding Design & Fabrication, September 1978, pp. 94-97.

10. Pense, A. W., Wood, J. D. and Fisher, J. W., "Recent Experiences with Electroslag Welded Bridges," Welding Journal, Vol. 60, No. 12, pp. 33-42, December 1981.

11. Pense, A. W., Wood, J. D. and Fisher, J. W., "Recent Experiences with Electroslag Welded Bridges," Welding Journal, Vol. 60, No. 12, p. 35, December 1981.

12. Private Communication with John Fisher.

13. Miller, I. and Freund, J. E., "Probability and Statistics for Engineers," 2nd edition, Prentice-Hall, Inc., New Jersey 1977.

14. Madison, R. B., "Application of Fracture Mechanics to Bridges," Lehigh University Institute of Research, Fritz Engineering Laboratory Report No. 335.2, June 1969.

15. Rice, J. R., "A Path Independent Integral and the Approximate Analysis of Strain Concentration by Notches and Cracks," Journal of Applied Mechanics, Transactions of ASME, pp. 379-386, June 1968.

16. Rice, J. R., Paris, P. C. and Merkle, J. G., "Some Further Results of J-Integral Analysis and Estimates," Progress in Flaw Growth and Fracture Toughness Testing, Proceedings of the 1972 National Symposium of Fracture Mechanics, ASTM STP 536, ASTM, 1973, pp. 231-245.

17. Merkle, J. G. and Corten, H. T., "A J-Integral Analysis for the Compact Specimen, Considering Axial Force as well as Bending Effects," Journal of Pressure Vessel Technology, Transactions of ASME, Paper No. 74 PVP-33, pp. 1-7.

18. Paton, B. E., "Electroslag Welding," American Welding Society, 2nd Edition, New York, 1962, p. 59.

19. Davenport, J. A., Qian, B. N., Pense, A. W. and Stout, R. D., "Ferrite Vein Cracking in Electroslag Welds," Welding Journal Vol. 60, No. 12, 1981, pp. 237s-243s.

20. Pussegoda, L. N. and Tyson, W. R., "Sensitivity of Electroslag Weld Metal to Hydrogen," Welding Journal, Vol. 60, No. 12, 1981, pp. 252s-257s.

21. Lowe, G., Bala, S. R. and Malik, L., "Hydrogen in Consumable Guide Electroslag Welds--Its Sources and Significance," Welding Journal, Vol. 60, No. 12, 1981, pp. 258s-268s.

22. Rolfe, S. T. and Barson, J. M., "Fracture and Fatigue Control in Structures--Applications of Fracture Mechanics," Prentice-Hall, Inc., New Jersey, 1977, pp. 414-418.

23. Barsom, John M., "The Development of AASHTO Fracture-Toughness Requirements for Bridge Steels," American Iron and Steel Institute, February 1975, p. 25.

24. Barsom, John M., "The Development of AASHTO Fracture-Toughness Requirements for Bridge Steels," American Iron and Steel Institute, February 1975, pp. 13, 14.

25. Fisher, J. W., Pense, A. W., Hausammann, H. and Irwin, G. R., "Quinnipiac River Bridge Cracking," Journal of the Structural Division, ASCE, Vol. 106, No. ST4, Proc. Paper 15343, April, 1980, pp. 773-789.

26. Dias, R. C., "Fatigue and Fracture of Electroslag Weldments in a Bridge," Thesis, Lehigh University, Department of Metallurgy and Materials Engineering, 1981.

27. Hertzberg, R. W., "Deformation and Fracture Mechanics of Engineering Materials," John Wiley & Sons, New York, 1976, p. 468.

28. Rolfe, S. T. and Barson, J. M., "Fracture and Fatigue Control in Structures--Applications of Fracture Mechanics," Prentice-Hall, Inc., New Jersey, 1977, p. 239.

29. Hertzberg, R. W., "Deformation and Fracture Mechanics of Engineering Materials," John Wiley & Sons, New York, 1976, p. 269.

APPENDIX I - J Integral Estimation Derivation

$$J \doteq \int_0^M \left(\frac{-\partial \theta_{total}}{\partial b} \right)_M dM \qquad (1)$$

where b = the remaining uncracked ligament length = W-a.

M = the remotely applied in-plane bending moment per unit thickness.

θ_{total} = the angle change between point of moment application

= θ no crack + θ with a crack

From a dimensional analysis it is found that the displacement due to the introduction a a crack is:

$$\theta_{crack} = f\left(\frac{M}{b^2}\right) \qquad (2)$$

From equation (2) it is found

$$\frac{-\partial \theta_{total}}{\partial b} = \frac{-\partial \theta_{crack}}{\partial b}_M = \frac{\partial \left[f\,(M/b^2) \right]}{\partial b}$$

$$= \frac{2M}{b^3} f'\left(\frac{M}{b^2}\right) \qquad (3)$$

since $$\frac{\partial \theta_{crack}}{\partial M}_b = \frac{\partial \left[f(M/b^2) \right]}{\partial M} = \frac{1}{b^2} f'(M/b^2) \qquad (4)$$

a combination of equations (3) and (4) leads to

$$\frac{-\partial \theta_{total}}{\partial b} = \frac{2M}{b^3} \left[b^2 \frac{\partial \theta_{crack}}{\partial M} \right]_b$$

$$= \frac{2M}{b} \left[\frac{\partial \theta_{crack}}{\partial M} \right]_b \qquad (5)$$

Substitution of equation (5) into equation (1) and integrating gives:

$$J = \frac{2}{b} \int_0^{M_{crack}} M \, d\, \theta_{crack} \qquad (6)$$

This suggests that J can be obtained by multiplying the work done in loading the specimen by $\frac{2}{b}$. If a remaining ligament is subject principally to bending and the load is applied by a force P then equation (6) becomes:

$$J = \frac{2}{b} \int_0^{\delta_{crack}} P \, d \, \delta_{crack} \qquad (7)$$

or

$$J = \frac{2}{b} \frac{A}{B} \qquad (8)$$

where A = area under the load displacement curve

B = the specimen thickness

The applicability of these equations requires: (1) the specimen geometry is such that plasticity encountered is confined to the uncracked ligament ahead of the crack; (2) applying the load in a bending mode; (3) we use a deeply notched sample such as the $\theta_{crack} \gg \theta_{no\ crack}$. By use of compact tension geometries with a/w ratio > 0.60 the above conditions are satisfied.

APPENDIX II

In these weldments the static (10^{-5}/sec) yield strength measured at room temperature is expected to be ~ (345-370) MPa [(50-54) ksi]. At -34.4°C (-30°F) and an intermediate loading rate (10^{-3}/sec) this yield strength will increase due to this increase in strain rate and decrease in temperature. Figure X shows an empirical correlation between static (10^{-5}/sec) and dynamic (10/sec) yield strengths as proposed by Rolfe for structural steels. By assuming a linear relationship for strain rate between these extremes we arrive at another empirical correlation between static (10^{-5}/sec) and intermediate (10^{-3}/sec) yield strengths:

$$\sigma_{y_{intermediate}} = \sigma_{y_{static}} + (6 \text{ to } 10) \text{ ksi}$$

This leads to an intermediate loading rate yield strength of ~ 415 MPa (60 ksi) for the electrogas weldments studied.

Another way of looking at this relationship is by considering how the residual stresses may be relaxed in these weldments. Obviously these weldments are going to be equilibrated for some length of time at room temperatures and static loading. Since the lowest material yield strengths will occur under these conditions the largest amount of relaxation will also occur to this level (i.e., to a residual stress level of 345 MPa (50 ksi)). A further increase in stress without further yielding would have to occur at temperatures below room temperature or under high strain rates.

The maximum expected magnitude to which this could occur is the value amount of the stress induced by impact and live loads. These are very conservatively estimated to be around 34.5 MPa (5 ksi), thus the maximum stress in these weldments should not increase beyond

$$345 + 34.5 \text{ MPa} \cong 380 \text{ MPa (55 ksi)}$$

under "normal" circumstances. It is thus believed that a stress of 415 MPa (60 ksi) is a very conservative estimate of the maximum stress to which these weldments might be subjected.

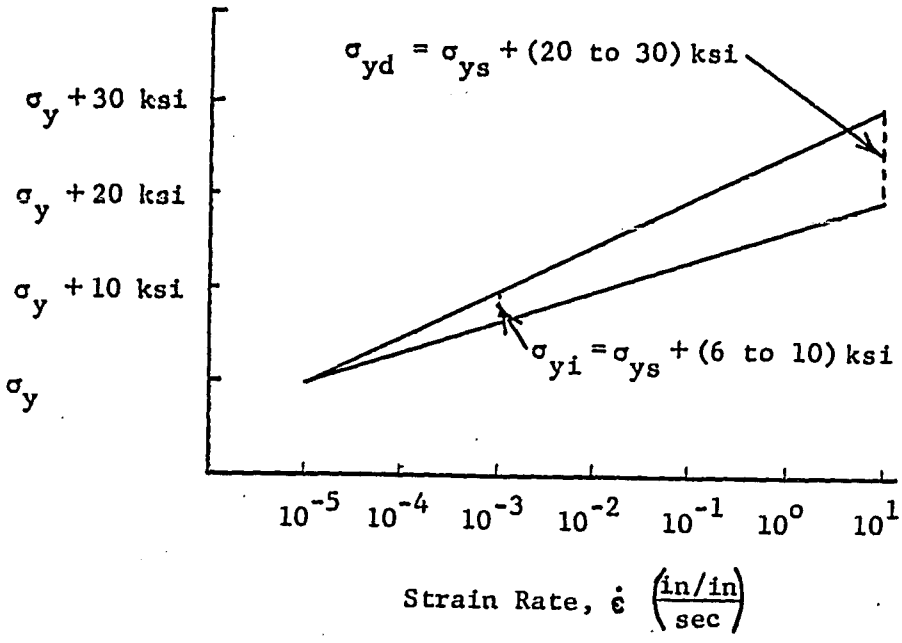

Figure X

VITA

Steve R. Paterson was born in Berkeley, California on February 11, 1955 to Robert and Dorothee Paterson. He was raised in Orinda, California, graduating from Miramonte High School, located nearby, in 1973.

Between 1973-1976 he attended Contra Costa Community College in San Pablo, California, where he received an Associate of Science Degree and a Certificate of Technology in Welding Technology. During this period he was also an instructor and co-director of a Mountaineering & Ecology School (The Moraga Mountaineers).

Between 1976-1980 he attended California Polytechnic State University in San Luis Obispo, California where he received a Bachelor of Science Degree in Metallurgy and Welding Engineering. During this period he also worked as a metallurgist at Mare Island Naval Shipyard (through Cal. Poly's Co-op education department), and as a research technician at the Oregon Graduate Center.

In September 1980, Mr. Paterson entered the Graduate School of Lehigh University where, engaged as a research and teaching assistant, he pursued a program of graduate study in the Department of Metallurgy and Materials Engineering.

Mr. Paterson is a member of the Tau Beta Pi honor society, the American Welding Society, and the American Society for Metals.

VITA

Steve R. Paterson was born in Berkeley, California on February 11, 1955 to Robert and Dorothee Paterson. He was raised in Orinda, California, graduating from Miramonte High School, located nearby, in 1973.

Between 1973-1976 he attended Contra Costa Community College in San Pablo, California, where he received an Associate of Science Degree and a Certificate of Technology in Welding Technology. During this period he was also an instructor and co-director of a Mountaineering & Ecology School (The Moraga Mountaineers).

Between 1976-1980 he attended California Polytechnic State University in San Luis Obispo, California where he received a Bachelor of Science Degree in Metallurgy and Welding Engineering. During this period he also worked as a metallurgist at Mare Island Naval Shipyard (through Cal. Poly's Co-op education department), and as a research technician at the Oregon Graduate Center.

In September 1980, Mr. Paterson entered the Graduate School of Lehigh University where, engaged as a research and teaching assistant, he pursued a program of graduate study in the Department of Metallurgy and Materials Engineering.

Mr. Paterson is a member of the Tau Beta Pi honor society, the American Welding Society, and the American Society for Metals.